MOLECULAR COMPOSITION AND STRUCTURE OF METAL COMPOUNDS IN ASPHALTENE

Fang Zheng

THÈSE

UNIVERSITE DE PAU ET DES PAYS DE L'ADOUR
École doctorale des Sciences Exactes et leurs Applications

Présentée et soutenue le 14 December 2020
par **Fang ZHENG**

pour obtenir le grade de docteur
de l'Université de Pau et des Pays de l'Adour
Spécialité : Chimie Analytique

MOLECULAR COMPOSITION AND STRUCTURE OF METAL COMPOUNDS IN ASPHALTENE

MEMBRES DU JURY

RAPPORTEURS
- Murray R. GRAY Professeur / University of Alberta
- Charles Philippe LIENEMANN IR-HDR/IFP EN

EXAMINATEURS
- Carlos AFONSO Professeur / Université de Rouen
- Pierre GIUSTI IR-HDR / TOTAL

DIRECTEURS
- Quan SHI Professeur / Université du Pétrole en Chine (Beijin)
- Brice BOUYSSIERE Professeur / Université de Pau et des Pays de l'Adour

UNIVERSITÉ DE PAU ET DES PAYS DE L'ADOUR

Preface

This Ph.D. thesis, subjected to the PhD Cotutelle Agreement signed between the Université de Pau et des Pays de l'Adour (UPPA) in France and the China University of Petroleum-Beijing (CUPB) in China has been carried out at the Institut des Sciences Analytiques et de Physico-Chimie pour l'Environnement et les Matériaux (IPREM) from UPPA and at the State Key Laboratory of Heavy Oil Processing from CUPB.

This Ph.D. thesis was financed by the China Scholarship Council, carried out by the UPPA and CUPB.

First of all, I would like to express my sincere gratitude to my two advisors: Prof. Brice Bouyssiere and Prof. Quan Shi for their continuous support and guidance throughout the last three years.

I would like to thank the support that I received from the professors at both the UPPA and CUPB. Without their support, I would not have been able to achieve the goals I proposed to myself: Carine Arnaudguilhem (UPPA), Yongmei Liang, Yahe Zhang, Xuxia Liu, Chao Ma, Chao Huang, Weilai Zhang, Weifeng Chang, Hao Wu, Yang Yang and Yuanyi Xu (CUPB).

I want to thank my fellow labmates and colleagues for all the help they have provided to me and the good moments we have shared during our free time: Ping Wang, Chen He, Jianxun Wu, Haidong Li, Lingzhi Zhang, Xiaocun Zhuo, Qiong Pan, Yunyun Li, Guangqing Cai and Limin Ren (CUPB); Vicmary Vargas, Remi Moulian, Aurore Mere, Ntau Mafisa and Victor Garcia Montoto (UPPA).

I will never forget all the friends I have made during the last three years. Among all the fantastic people I have met, I would like to thank my Chinese group of friends (Haikun Zhao, Li Tao and Lei Qin); my France group of friends (Victor Garcia Montoto, Guanlan Wang, Juncheng Guo, Mengwan Xu, Xue Wang and Huaiyuan Ren)

I would like to thank my parents and brother for their patience and their continuous support and encouragement.

I would like to thank my wife Ying Wang for her long love and continuous support, I'll be with her for the rest of my life.

I would also like to thank my son Fengyi Zheng for the happiness he brings to me and I hope to accompany him every moment of growth.

Abstract

The Asphaltene brings many negative effects to the exploitation, storage, transportation and refining of petroleum. As the most complex fraction in petroleum, the structure and composition of asphaltenes have always been one of the important issues in the field of petroleum science. Asphaltene contains most of the metal elements in petroleum, which have not been fully characterized to date. An in-depth exploration of the composition of metal compounds in asphaltenes not only allows to fully understanding of metals in petroleum, but also helps to understand the structure and composition of asphaltenes. In this thesis, Canadian oilsands bitumen, Venezuelan heavy oil asphaltenes, Qingchuan gilsonite and Texas immature marine shales were taken as the research objects. Molecular composition of asphaltenes and metals inside were characterized with the help of high-resolution mass spectrometry as well effective separation methods. A variety of chemical derivatization methods were used to treat the asphaltenes to define the existence of metal compounds inside, and provide informations of the asphaltene composition. The main contents of this work include:

Supercritical fluid extraction fractionation (SFEF) was used to separate the Canadian oilsands bitumen-derived vacuum residue, and Fourier ion cyclotron resonance mass spectrometry (FT-ICR MS) was used to characterize the molecular composition of each fraction in detail. As the SFEF fractions became heavier, the mass ranges of mass spectra and DBE values of polar heteroatom species were constantly increasing. The abundance of multifunctional group compounds and vanadyl porphyrins increased as the SFEF fraction became heavier. In the final end-cut fraction, the relative abundance of N_4VO and N_5VO class species vanadyl porphyrins accounted for 98 %.

Detailed molecular composition characterization of the porphyrins in the Texas immature marine shales was conducted. Iron porphyrins, vanadyl porphyrins, gallium porphyrins and nickel porphyrins were detected simultaneous in the shale samples. Three new oxygen-containing iron porphyrins were discovered, namely $C_nH_mN_4FeO$, $C_nH_mN_4FeO_2$ and $C_nH_mN_5FeO_2$. Gallium porphyrins were identified in petroleum samples for the first time. The discovery of petroleum gallium porphyrin and a variety of oxygen-containing porphyrins gave us a new understanding of the evolution path of petroporphyrins.

The molecular composition of Qingchuan gilsonite was characterized by various techniques. The metalloporphyrins in gilsonite were analysis in detail, which provided a reference for the molecular composition information of gilsonite and provided a supplement for the analysis of petroporphyrins inside. The distribution range of sulfur-containing porphyrins expanded the understanding of the evolution of petroporphyrins.

The aggregation behavior and fragmentation pathway of porphyrin was characterized in detail via trapped ion mobility spectrometry coupled time-of-flight mass spectrometer (TIMS-TOF MS). According to the

mobility spectra of porphyrins obtained from TIMS, it is believed that a considerable part of porphyrin compounds in petroleum asphaltene exist in the form of aggregations. The coordinated porphyrin compounds in the form of N_5VO in petroleum were characterized in detail.

A variety of chemical derivatization methods were designed to process the asphaltenes to define the existence of metal compounds inside, including acid treatment, hydropyrolysis, methanesulfonic acid demetalization, and silanization. The possible forms of "non-porphyrin" were confirmed as well the existence of metallic nickel and vanadium compounds in asphaltenes. All of the nickel and vanadium compounds in asphaltene have the core structure of metalloporphyrin. the porphyrins in asphaltene have larger weight and higher condensation degree, and some of them exist in the form of coordination compounds with other ligands. In addition, the porphyrins in asphaltenes are strongly aggregated with asphaltenes with the intermolecular interactions. The association makes the porphyrins in asphaltenes have apparent macromolecular structure, and it is difficult to be separated, ionized, vaporized, and detected by UV. This aggregation behavior is an equilibrium process, which can be broken by exotic charged particles.

Résumé

L'asphaltène a de nombreux effets négatifs sur l'exploitation, le stockage, le transport et le raffinage du pétrole. En tant que fraction la plus complexe du pétrole, la structure et la composition des asphaltènes ont toujours été l'un des problèmes importants dans le domaine de la science pétrolière. Les asphaltènes contiennent la plupart des éléments métalliques du pétrole, qui n'ont pas été complètement caractérisés à ce jour. Une exploration approfondie de la composition des composés métalliques dans les asphaltènes permet non seulement de bien comprendre les métaux dans le pétrole, mais aide également à comprendre la structure et la composition des asphaltènes. Dans cette thèse, le bitume des sables bitumineux canadiens, les asphaltènes de pétrole lourd vénézuélien, la gilsonite de Qingchuan et les schistes marins immatures du Texas ont été considérés comme objets de recherche. La composition moléculaire des asphaltènes et des métaux à l'intérieur a été caractérisée à l'aide de la spectrométrie de masse à haute résolution ainsi que de méthodes de séparation efficaces. Diverses méthodes de dérivatisation chimique ont été utilisées pour traiter les asphaltènes pour définir l'existence de composés métalliques à l'intérieur et fournir des informations sur la composition des asphaltènes. Le contenu principal de ce travail comprend:

Le fractionnement par extraction par fluide supercritique (SFEF) a été utilisé pour séparer les résidus sous vide dérivés du bitume des sables bitumineux canadiens, et la spectrométrie de masse par résonance cyclotronique à ions de Fourier (FT-ICR MS) a été utilisée pour caractériser la composition moléculaire de chaque fraction en détail. Au fur et à mesure que les fractions SFEF devenaient plus lourdes, les gammes de masse des spectres de masse et les valeurs DBE des espèces d'hétéroatomes polaires augmentaient constamment. L'abondance des composés du groupe multifonctionnel et des vanadyl porphyrines a augmenté à mesure que la fraction SFEF devenait plus lourde. Dans la fraction de coupe finale, l'abondance relative des vanadyl porphyrines des espèces des classes N_4VO et N_5VO représentait 98%.

Une caractérisation détaillée de la composition moléculaire des porphyrines dans les schistes marins immatures du Texas a été réalisée. Des porphyrines de fer, des vanadyl porphyrines, des porphyrines de gallium et des porphyrines de nickel ont été détectées simultanément dans les échantillons de schiste. Trois nouvelles porphyrines de fer contenant de l'oxygène ont été découvertes, à savoir $C_nH_mN_4FeO$, $C_nH_mN_4FeO_2$ et $C_nH_mN_5FeO_2$. Des porphyrines de gallium ont été identifiées pour la première fois dans des échantillons de pétrole. La découverte de la porphyrine de gallium de pétrole et d'une variété de porphyrines contenant de l'oxygène nous a donné une nouvelle compréhension du chemin d'évolution des pétroporphyrines.

La composition moléculaire de la gilsonite de Qingchuan a été caractérisée par diverses techniques. Les métalloporphyrines dans la gilsonite ont été analysées en détail, ce qui a fourni une référence pour les informations de composition moléculaire de la gilsonite et a fourni un supplément pour l'analyse des

pétroporphyrines à l'intérieur. La gamme de distribution des porphyrines contenant du soufre a élargi la compréhension de l'évolution des pétroporphyrines.

Le comportement d'agrégation et la voie de fragmentation de la porphyrine ont été caractérisés en détail par spectrométrie de masse à temps de vol couplé par spectrométrie de mobilité ionique piégée (TIMS-TOF MS). D'après les spectres de mobilité des porphyrines obtenus à partir de TIMS, on pense qu'une partie considérable des composés de porphyrine dans les asphaltènes de pétrole existe sous forme d'agrégations. Les composés de porphyrine coordonnés sous forme de N_5VO dans le pétrole ont été caractérisés en détail.

Diverses méthodes de dérivatisation chimique ont été conçues pour traiter les asphaltènes afin de définir l'existence de composés métalliques à l'intérieur, notamment le traitement acide, l'hydropyrolyse, la démétallisation à l'acide méthanesulfonique et la silanisation. Les formes possibles de "non porphyrine" ont été confirmées ainsi que l'existence de composés métalliques de nickel et de vanadium dans les asphaltènes. Tous les composés de nickel et de vanadium contenus dans l'asphaltène ont la structure centrale de la métalloporphyrine. les porphyrines dans l'asphaltène ont un poids plus important et un degré de condensation plus élevé, et certaines d'entre elles existent sous forme de composés de coordination avec d'autres ligands. De plus, les porphyrines dans les asphaltènes sont fortement agrégées avec les asphaltènes avec les interactions intermoléculaires. L'association fait que les porphyrines dans les asphaltènes ont une structure macromoléculaire apparente, et il est difficile de les séparer, ioniser, vaporiser et détecter par UV. Ce comportement d'agrégation est un processus d'équilibre, qui peut être rompu par des particules chargées exotiques.

摘 要

石油沥青质给石油的开采、储运及加工过程带了很多负面的影响。作为石油中最复杂的组分，沥青质的结构和组成一直以来都是石油科学领域研究的热点课题，沥青质本身的复杂性让赋予它一层难以揭开的神秘面纱。沥青质含有了石油中的大部分金属元素，石油中金属化合物由于沥青质的遮盖而至今没能被全面表征。深入探究沥青质中金属化合物尤其是镍、钒化合物的组成，不仅能够让全面认识石油中的金属的存在形态，更有利于以此为切入点，逐渐了解沥青质的结构组成。本文以加拿大油砂沥青、委内瑞拉重油沥青质、青川岩沥青和美国德州鹰福特地形油页岩样品为研究对象，采用有效的分离方法，借助高分辨率质谱分析沥青质的分子组成；详细表征沥青质中的石油卟啉类化合物并致力于发现新型的卟啉化合物；以多种化学衍生方法处理沥青质组分来探究其中金属化合物的存在形态，并以此提供沥青质组成的部分信息。主要内容包括：

表征了加拿大油砂沥青减压渣油中钒卟啉的分子组成及其在超临界萃取组分中的分布。杂原子化合物的分子量分布范围和分子缩合度都随着组分的变重而升高，不同组分中化合物的类型存在差异。各 SFEF 组分中钒卟啉类化合物的丰度随着组分的变重而不断升高，在萃取残渣的质谱图中几乎所有的质谱峰均为 N_4VO 和 N_5VO 类型的钒卟啉化合物。加拿大油砂沥青减渣的 SFEF 组分中杂原子化合物的分布与委内瑞拉减渣的 SFEF 组分中杂原子化合物的分布具有较大相似性。

在美国德州油页岩抽提物中同时检测到了铁卟啉、镓卟啉、镍卟啉和钒卟啉。其中铁卟啉类化合物的丰度最高，所有六种常规的石油铁卟啉化合物都存在，同时还含有大量的高缩合的铁卟啉化合物。发现了三种新型的含氧铁卟啉化合物，分别是 $C_nH_mN_4FeO$、$C_nH_mN_4FeO_2$ 和 $C_nH_mN_5FeO_2$。首次在石油样品中发现镓卟啉化合物。石油镓卟啉和多种含氧卟啉类化合物的发现为石油卟啉化合物的演化路径提供了新的证据。

对四川岩沥青中卟啉类化合物进行了详细表征。获得了岩沥青中金属化合物的性质以及其中卟啉类化合物的分子组成信息，为天然沥青的成因研究及资源利用提供了重要的基础数据；含硫卟啉化合物的组成与分布信息扩充了对石油卟啉化合物的演化规律的认识。

通过多种物理分离和化学转化处理，为沥青质中“非卟啉”化合物的存在形态研究提供了重要证据：沥青质中的镍、钒等金属化合物都具有金属卟啉化合物的核心结构，但是沥青质中的卟啉分子质量更大、缩合度更高，且大多会与其它配体形成配位卟啉单元。此外，在多种分子间作用力下，沥青质中的卟啉化合物分子会与沥青质分子产生严重的缔合。缔合作用使沥青质中的卟啉化合物形成表观大分子结构，且难以被分离、难以被电离、难以汽化、紫外特征吸收也因此减弱甚至消失。

结合离子淌度质谱和高分辨质谱等表征手段对卟啉化合物的缔合行为进行了表征。质谱分析中容易形成卟啉离子缔合体，便在离子转输过程中很容易发生解离，导致石油中金属化合物难以被准确分析。对金属卟啉化合物在质谱分析过程中的缔合、裂解行为的详细研究，有利于了解质谱解析卟啉化合物过程中卟啉离子的状态，也能够对石油特别是沥青质中卟啉化合物的存在形态有更深入的认识。另外探索了基于高分辨率质谱测定复杂基质中卟啉类化合物 ^{13}C 同位素的测试方法。

通过多种物理分离和化学转化处理，为沥青质中“非卟啉”化合物的存在形态研究提供了重要证据：沥青质中的镍、钒等金属化合物都具有金属卟啉化合物的核心结构，但是沥青质中的卟啉分子质量更大、缩合度更高，且大多会与其它配体形成配位卟啉单元。此外，在多种分子间作用力下，沥青质中的卟啉化合物分子会与沥青质分子产生严重的缔合。缔合作用使沥青质中的卟啉化合物形成表观大分子结构，且难以被分离、难以被电离、难以汽化、紫外特征吸收也因此减弱甚至消失。这种缔合现象是一个平衡过程，可被外来带电粒子打破。

Contents

List of publications

1. **Zheng, F.**; Hsu, C. S.; Zhang, Y.; Sun, Y.; Wu, Y.; Lu, H.; Sun, X.; Shi, Q., Simultaneous Detection of Vanadyl, Nickel, Iron, and Gallium Porphyrins in Marine Shales from the Eagle Ford Formation, South Texas. Energy & Fuels 2018, 32 (10), 10382-10390.

2. **Zheng, F.**; Chung, W.; Palmisano, E.; Dong, D.; Shi, Q.; Xu, Z.; Chung, K. H., Molecular characterization of polar heteroatom species in oilsands bitumen-derived vacuum residue fractions by Fourier transform ion cyclotron resonance mass spectrometry. Petroleum Science 2019, 16 (5), 1196-1207.

3. **Zheng, F.**; Zhu, G.; Chen, Z.; Zhao, Q.; Shi, Q., Molecular composition of vanadyl porphyrins in the gilsonite. Journal of Fuel Chemistry and Technology 2020, 48 (5), 562-567.

4. 郑方; 朱光有; 陈志强; 赵秋利; 史权, 岩沥青中钒卟啉化合物分子组成分析. 燃料化学学报 48 (05), 562-567.

5. **Zheng, F.**; Shi, Q; Salvato Vallverdu, G.; Giusti, P.; Bouyssiere, B., Fractionation and Characterization of Petroleum Asphaltene: Focus on Metalopetroleomics. Processes 2020.

6. **Zheng, F.**; Zhang, Y; Zhang, Y; Han, Y; Zhang, L; Bouyssiere, B; Shi, Q. Aggregation of petroporphyrins and fragmentation of porphyrin ions: characterized by TIMS-TOF MS and FT-ICR MS. **Submitted to Fuel (July 2020).**

7. Moulian, R.; **Zheng, F.**; Salvato Vallverdu, G.; Barrere-Mangote, C.; Shi, Q.; Giusti, P.; Bouyssiere, B., Understanding the Vanadium–Asphaltene Nanoaggregate Link with Silver Triflate Complexation and GPC ICP-MS Analysis. Energy & Fuels 2020.

8. **Zheng, F.**; Moulian, R.; Shi, Q.; Giusti, P.; Bouyssiere, B., Study of asphaltene nanoaggregates by silver triflate reaction and GPC ICP-MS. **(To be submitted to Energy & Fuels).**

Chapter 1. Literature review

1.1 Asphaltene and the containing heteroatoms

1.1.1 Introduction of asphaltene

Petroleum as the most important source of energy and chemical raw materials, is a complex but delicately balanced system that depends upon the relationship of the constituent fractions to each other.[1] Hence, the disturbance of these interactions such as recovery and refining may cause the formation of sediment and the deposition of asphaltene,[2-3] which brings many negative effects to the petroleum industry such as deactivation of catalysts, blocking pipelines, and deposition on the internal surface of the reservoirs, etc.[4-7]

Asphaltenes is the most polar fraction in crude oil, which provides very low economic value and raising adverse effects on oil industry. The images of *n*-heptane petroleum asphaltenes are shown in Figure 1.1. The content and the characteristics of the asphaltenes depend to a greater or lesser extent on the source of the crude oil.[8] Operationally, asphaltenes are defined as compounds insoluble in aliphatic hydrocarbons such as *n*-pentane or *n*-heptane, and soluble in aromatics as toluene and benzene.[9] Asphaltene is dark brown to black friable solids that have no definite melting point and usually foam and swell on heating to leave a carbonaceous residue.[10] The molecular weights of asphaltenes span a wide range from hundreds to millions leading to speculation about self-aggregation.[11] Carbon and hydrogen are the most abundant elements in asphaltenes, and the contents of carbon and hydrogen are usually greater than 90 wt%. These values correspond to a hydrogen-to-carbon atomic ratio of 1.15 in n-C_7 (n-heptane) asphaltenes.[12] In contrast to carbon and hydrogen, the content of undesired heteroatoms in asphaltenes usually vary greatly, especially sulfur.[13] Sulfur contents vary from 0.05 to 7.0 wt%.[12] On the other hand, the nitrogen content of the asphaltene constituents has a somewhat lesser degree of variation (0.05-0.5 wt%) and oxygen contents generally less than 1.0 wt%.[14] In addition, there are some metallic elements in asphaltenes, which are distributed in the range of 0-4000 ppm, among which nickel and vanadium are the most abundant. Metal atoms in asphaltenes are usually present in the form of metalloporphyrins.[15] And may also be present as so called "non-porphyrins", but have not been proved.[16]

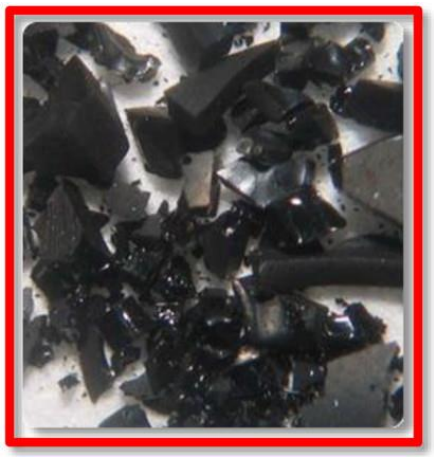

Figure 1.1 Laboratory sample of asphaltenes extracted from crude oil in *n*-heptane[17]

Composition and properties of asphaltenes has always been one of the most important issue for petrochemistry. Over several decades, many researchers have contributed to characterization, analysis, and determination of physicochemical properties of asphaltenes by various analytical techniques, but these studies have been only partially successful primarily because the asphaltenes exhibit significant complexity. Asphaltene molecules are highly condensed and relatively high in undesired heteroatoms and metals, leading to stubborn self-aggregation.[18] The asphaltenes defined as a solubility class differs from a chemical class so some variability among different asphaltenes is expected. To further complicate the problem, multifarious different source crude oils and preparation procedures exist for asphaltenes. The characterization of asphaltenes is still a very difficult and challenging issue.

1.1.2 Heteroatoms in asphaltenes

^{13}C NMR and x-ray studies show that the carbon distribution is typically about 40% aromatic and the remainder, saturated.[19] However, the hydrogen is found primarily (>90%) on saturated carbons, predominantly methylene groups, as determined by Fourier transform infrared (FT-IR) and NMR spectroscopy.[19] Asphaltenes generally contain small quantities of heteroatoms and metals, amounting to a few percent. The heteroatomic chemical functions are often polar and sometimes charged yielding strong intermolecular interactions. Metal atoms could be complexed by heteroatoms bring diverse adverse impact on petroleum refining. Thus, understanding the heteroatom chemistry and metal morphology is an essential component of asphaltene characterization.

Sulfur is the most abundant heteroatom in petroleum, generally ranging from 0.05 to 7.0 wt%.[20] Crude oils made from them vary in sulfur content according to different origins. Sulfur-containing compounds in crude oils can be categorized into six basic types in terms of their functional groups: H_2S, elemental sulfur, mercaptans, sulfides, thiophenes and polysulfides. Sulfones and sulfoxides are also found to be present in small quantities in many crude oils and mainly remains in asphaltene fraction. These oxidized sulfur species

are generated through oxidation in reservoirs by contact with oxic-water or subsequent to the extraction exposed to air.[14] X-ray absorption near edge structure spectroscopy (XANES) offers a powerful and nondestructive technique for specialization and quantization the chemical structures heteroatoms in asphaltenes.[21] Deconvolution usually conducted on the XANES spectra to improve resolution and dissolve the mixtures.[14] The results of sulfur XANES on asphaltenes showed that thiophene is the most dominant functional and followed by sulfide in general.[14, 22-23] Sulfoxides is the most dominant form of the oxidized sulfur species but not found in all samples. Thiophene sulfone was also detected in some asphaltene samples by derivative XANES spectra.[24] These oxidized sulfur compounds are related to the special reservoir environment or may be oxidized during transportation and storage. GPC-ICP-HR-MS has been applied to separate and monitor the size distribution of sulfur-containing compounds in asphaltenes and other petroleum fractions.[25-27] The sulfur-containing compounds are predominant in the aromatics and resins (75-90%), and only 10-25% distribute in asphaltenes, indicating medium polarity is prominent.[26] The S compounds present in asphaltenes are mainly associated with the high high-molecular-weight fraction (70-80%).[27] The molecular composition of heteroatom-containing species in asphaltenes have been analyzed by FT-ICR MS. Molecular formula of these polar compounds can be observed directly with the high resolution of the ICR. Multi-heteroatomic sulfur-containing compounds, such as N_1S_1, O_1S_1, S_2 and S_3 species, have been detected in asphaltenes.[28-30] Sulfur-containing vanadyl porphyrins in petroleum asphaltenes also identified by APPI FT-ICR MS.[31] High-resolution mass spectrometry possesses unique advantages in analyzing heteroatom-containing compounds in complex matrices.

The content of nitrogen element in petroleum is generally account for 0.05-0.5 wt%, with obvious increase of nitrogen concentrations in the vacuum bottoms and asphaltenes.[14] Nitrogen XANES studies on asphaltenes demonstrated that almost all of the nitrogen found in asphaltenes is aromatic existing as the form of pyrrolic or pyridinic. Pyrrolic nitrogen is more predominant than pyridinic forms. Contributions from (saturated and aromatic) amines found are to be negligible.[22] High-resolution mass spectrometry provides a molecular level understanding of the existence of nitrogen-containing compounds in asphaltenes.[32] The most abundant N_1 class species in Venezuela asphaltenes are dibenzocarbazoles.[28] The DBE values of N_1 class species are all above 9, which means these compounds have higher aromaticity than carbazole and phenanthridine. Similar DBE distribution of N_1 class species also exists in the asphaltene fractions of Liaohe crude oil and Canadian oilsands bitumen.[29, 33] The highest relative abundance of N_1 class species in Liaohe asphaltene was at DBE of 9, 12, 15, and 18, corresponding to carbazoles, benzocarbazoles, dibenzocarbazoles, and benzonaphthocarbazoles, respectively.[33] Thus, Arylcarbazole should be the predominant form of N_1 class species. Multi-heteroatomic nitrogen-containing compounds also widely distribute in the asphaltenes and all of them performing high degree of condensation. The porphyrin compound in asphaltene is also a kind of nitrogen-containing compound, and its existence form will be described in detail below.

Oxygen-containing compounds in petroleum can generally be categorized into two types according to their acid-base properties: acidic compounds, mainly composed of phenol and carboxylic acid which is usually referred to petroleum acid, and neutral compounds, mainly containing aldehydes, ethers, esters and furans. The oxygen in asphaltenes is present primarily in the form of phenolic hydroxyl function, contribute a strong hydrogen-bonding for intermolecular association.[34-35] Infrared spectroscopic examination on asphaltenes indicated that two or more oxygen-containing functions (e.g., hydroxyl and carbonyl) may reside in the same aromatic ring or a condensed aromatic system.[36] Recent studies have indicated that higher-order oxygen-containing compounds contain lower abundance-weighted DBE values, suggesting that lower aromaticity is offset by higher oxygen content.[37] These low condensation molecules with high oxygen content reside in the asphaltene fraction may due to hydrogen bonding. The morphology of oxygen-containing compounds in asphaltenes is more complicated than that of nitrogen and sulfur species, because there are further oxygen-containing functional groups, and hydrogen bonding performs a crucial role in the aggregation behavior of petroleum asphaltenes.

1.2 Research status of metal compounds in petroleum and asphaltenes

1.2.1 Metal in petroleum

Petroleum is a complex mixture containing not only carbon, hydrogen, sulfur, oxygen, and nitrogen but also many trace elements, including 45 metals such as V, Ni, Fe, etc.[38] It is well known that quite amount of metal in crude oil is existing in the asphaltene fraction. These metals are detrimental to petroleum processing, especially for accelerating catalyst deactivation.[39] Metal contents is one of the important parameters for evaluating crude oil. The modern instrumental approaches to determine trace metals in crude oil as well its asphaltenes is by means of physical methods. Developing of analytical methods have been performed for the determination of metals in crude oils and the derivatives using various analytical techniques including, flame atomic absorption spectrometry (FAAS),[40] graphite furnace atomic absorption spectrometry (GF AAS),[41] inductively coupled plasma optical emission spectroscopy (ICP-OES),[42] inductively coupled plasma mass spectrometry(ICP-MS),[43] X-ray fluorescence spectroscopy,[44] spectrophotometry,[45] and high performance liquid chromatography (HPLC).[46] To date, concentrations of these metals in petroleum have been mostly determined by ICP-OES and ICP-MS because of their distinguished sensitivity, repeatability and operability[47]. A large amount of data indicates that the metals content in crude oil is between 1 and 10000 μg/g, and the concentrations of nickel and vanadium can reach up to several thousand wppm.[48] The concentration of these metals in asphaltene fraction is the most abundant. The concentration range of V, Ni and Fe in asphaltenes from the literature is shown in Table 1.1.

Table 1.1 Concentrations of V, Ni and Fe in asphaltenes with different origin

Origin of the Asphaltene	Concentration Range of V (ppm)	Concentration Range of Ni (ppm)	Concentration Range of Fe (ppm)	Reference
Venezuela crude oils	1300-4000	300-410		[26]
Kuwait crude oils	200-800	50-120		[49]
Athabasca oil sand	640	240	260	[50]
Utah oil sand	21	170	4820	[50]
Russia Tatarstan crude oils	200-10000	120-550		[51]
China Qingchuan Gilsonite	3888	366	491	[52]
Texas shale	270	257	634	[53]

The most abundant and troublesome metal-containing compounds present in the petroleum deposits are vanadium and nickel. The majority of these complex is contained within the highly aromatic, highly polar asphaltene fraction poses some significant difficulties.[16, 39] The exact molecular form of these metals remains the focus of controversy among researchers in the field. Undoubted fact is that a portion of vanadium and nickel in asphaltenes deposits in the form of petroporphyrins.[53-54] Another part of nickel and vanadium compounds in petroleum that have no characteristic absorption peaks in the UV-vis are temporarily defined as "non-porphyrins". Due to the lack of suitable characterization methods for these nickel and vanadium compounds, they are currently limited to the study of their average structure, and there is no molecular level characterization. Scholars have never identified any “non-porphyrin”. At the same time, the discovery of new porphyrins and the inaccuracy of UV quantification make the existence of non-porphyrins questionable.

1.2.2 Research progress of petroporphyrin

As a geological biomarker, porphyrins have been used in petroleum exploration to determine the source rock type, maturity, hydrocarbon generation threshold, and hydrocarbon expulsion migration. It also provided important information for the studies of oil-source rock comparison, oil and gas reservoir types, and oil/gas reservoir distribution.Since the discovery of metalloporphyrins in crude oil and shales by Treibs,[55-56] who postulated that porphyrins were derived from chlorophylls and hemes (hemoglobins) in the living organisms where Mg and Fe functioned as cofactors, porphyrins have been extensively studied. During the burial of dead organisms that escaped oxidation, cofactors in chlorophylls and hemes would have been ion-exchanged with other metal elements, such as nickel and vanadium, in the depositional environments and formed more stable metalloporphyrins as “petroporphyrins”. Petroporphyrins contain metal cores that are detrimental to

petroleum processing, especially for accelerating catalyst deactivation.[39] Hence, systematic studies on petroporphyrins are of particular importance to the research into petroleum formation and oil refining.

Many analytical techniques including spectroscopy and mass spectrometry have been widely used to analyze petroporphyrins.[57-60] Ultraviolet-visible (UV-vis) spectroscopy is commonly used to identify and quantify petroporphyrins due to its high sensitivity to metalloporphyrins and metal-free porphyrins in electronic absorption of UV-vis radiation.[61] The emergence of mass spectrometry technology in 1960s led to new development in the identification of petroporphyrins. Vanadyl, nickel and iron porphyrins have been found in crude oil and shale present in several types.[62-64] Etio porphyrins (ETIO) and deoxophylloerythroetio porphyrins (DPEP) are two most common types with double-bond equivalences (DBE, i.e., number of rings plus double bonds) of 17 and 18, respectively.[65] Other types of porphyrins such as dicyclic-deoxophylloerythroetio (di-DPEP), rhodo-etio (rhodo-ETIO), rhodo-deoxophylloerythoetio (rhodo-DPEP), and rhodo-dicyclic-deoxophylloerythroetio (rhodo-di-DPEP) have also been identified in petroleum.[59, 65-67] With the development of ultrahigh resolution mass spectrometry in the last decade, studies on petroporphyrins have made a great progress.[68-70] Fourier-transform ion cyclotron resonance mass spectrometry (FT-ICR MS) offers the highest available broadband mass resolution and accuracy, allowing the assignment of a unique elemental composition to each mass spectral peak measured to analyze complex mixtures.[71-74] The high ionization efficiency and selectivity of electrospray ionization (ESI) improves the analysis for identifying trace polar compounds.[75] Rodgers *et al.* first applied positive-ion ESI to petroporphyrin-enriched fractions and identified porphyrin monomers and dimers. Mckenna *et al.*[65] and Qian *et al.*[76] identified vanadyl and nickel porphyrins in heavy crude oil and asphaltene by atmospheric pressure photoionization (APPI) FT-ICR MS combined offline chromatographic fractionation, who also combined quantitation with ICP-MS. Qian *et al.*[31] gave the primary evidence of sulfur-containing vanadyl porphyrins. Cho *et al.*[77] evaluated laser desorption ionization (LDI) FT-ICR MS to study metalloporphyrin complexes. Zhao *et al.*[78] combined chromatographic fractionation with ESI FT-ICR MS and identified three series of vanadyl porphyrins that contain oxygen functional groups, which should include the porphyrin acids identified by Ocampo *et al.*[79-80] in an oil shale. Schaub *et al.*[81] applied FT-ICR MS for direct characterization of iron porphyrins in hydrothermal liquefaction biocrude oils. Therefore, FT-ICR MS has become a more informative technique to characterize petroporphyrins. The overview of the known vanadyl-, nickel- and iron-petroporphyrin types are listed in table 1.2.

Table 1.2 An overview of the known vanadyl-, nickel- and iron-petroporphyrin types

	Vanadyl porphyrins	Nickel porphyrins	Iron porphyrins	Reference
Multi-oxygen	$C_mH_nN_4VO_1$	$C_mH_nN_4Ni$	$C_mH_nN_4Fe$	[53]
	$C_mH_nN_4VO_2$	$C_mH_nN_4NiO_1$	$C_mH_nN_4FeO_1$	[53]
	$C_mH_nN_4VO_3$		$C_mH_nN_4FeO_2$	[53]
	$C_mH_nN_4VO_4$			[54]
Multi-sulfur	$C_mH_nN_4VO_1S_1$			[31]
	$C_mH_nN_4VO_1S_2$			[82]
	$C_mH_nN_4VO_1S_3$			[82]
Multi-nitrogen	$C_mH_nN_5VO_1$			[83]
Multi-heteroatomic	$C_mH_nN_4VO_2S_1$			[82]
	$C_mH_nN_4VO_3S_1$			[82]
	$C_mH_nN_4VO_4S_1$			[82]
	$C_mH_nN_4VO_2S_2$			[82]
	$C_mH_nN_4VO_3S_2$			[82]
	$C_mH_nN_5VO_2$			[83]
			$C_mH_nN_5FeO_2$	[53]

1.2.3 Research progress of "non-porphyrin"

UV-vis has been widely used in the identification and quantification of petroporphyrins because of the sensitive electronic absorption.[61] However, the measured UV-vis absorption of petroporphyrins is much too small to account the total vanadium and nickel content in asphaltenes, scilicet a significant part of the porphyrins presents in asphaltene fraction lacking this characteristic absorption.[84] Therefore the definition of “non-porphyrin” was introduced. But no corroborated "non-porphyrin" compound has been found to date.[16] The bonding structure surrounding of vanadium and nickel atoms within the asphaltenes determined by EXAFS and XANES showed that all of them present in asphaltene samples is present as a metal ion (i.e., V=O and Ni) coordinated to four nitrogen ligands.[85-88] A major barrier to effective quantitation of petroporphyrins in asphaltene is the significant interference from asphaltene matrix.[89] The lack of porphyrin

characteristic absorption in asphaltenes could be attributed to the chemical interactions between asphaltene molecules and porphyrin molecules.[90]

The size distributions of metals in asphaltenes could be well characterized by GPC ICP-MS.[91] Approximately 80% of total V present in HMW and MMW compounds as the form of nanoaggregates. HMW compounds were even observed in an asphaltene solution that was diluted by 40000-fold (25 mg/kg) indicating the interaction between asphaltene molecules is strong enough to resist the dissolution of the solvent.[26] Other metals in asphaltene, such as sodium and calcium, are presumed to exist in the form of organic carboxylates. But so far, their presence has not clearly been confirmed yet due to the complexity of asphaltenes.

The characterization of the metal-containing compounds by using the gas chromatography with a high temperature injector and an atomic emission detector (HT GC–AED) providing the valuable information on identification of metal porphyrin species in the heavy oil fractions as well asphaltenes.[49, 92] Although most V-containing compounds in the asphaltenes are non-volatile and cannot be analyzed by GC even with a high temperature, these results revealed that porphyrin units existing in the asphaltenes linked to the larger aggregates.[49] The V and the Ni complexes present in asphaltene fraction display a strong interaction with their matrixes.

There are three inferences about the existence of "non-porphyrin": First, “non-porphyrin” is aggregates of petroporphyrins with asphaltene molecules. Due to the influence of asphaltene matrix, these porphyrin compounds are no characteristic absorption in the ultraviolet spectrum; secondly, “non-porphyrin” is coordination compounds formed by heteroatom compounds such as N, O, S with petroleum porphyrin. The effect of coordination makes the characteristic absorption peaks of porphyrin compounds deviate to varying degrees. After the superposition, the absorption peak tends to be smooth, and then the characteristic absorption peak disappears; third, the “non-porphyrin” compound has a different structure from the petroporphyrins. However, there is no strong evidence for the identification “of non-porphyrins”, and no “non-porphyrin” compounds have been confirmed yet.

Goulon *et al.*[86] measured the EXAFS/XANES spectra for Boscan asphaltenes and compared them to those for oxovanadyl (VO^{2+}) OEP and thiovanadyl (VS^{2+}) OEP. As well, the asphaltene spectra were compared to the spectra of authentic petroporphyrins extracted from the original crude sample using dichloromethane þ n-hexane mixtures followed by chromatographic separations on aluminum oxide and silica gel columns. Although UV/visible Soret absorbance of the asphaltenes accounted for only 13-15% of the total vanadium present in the asphaltene fractions, the EXAFS and XANES spectra of the whole asphaltenes were almost completely superimposed on the spectra for pure VOOEP and the authentic petroporphyrins in toluene. This result indicated that, although the asphaltenes show very high levels of “non-porphyrinic” vanadium (i.e., vanadium with no UV/visible absorbance), the vanadium within this fraction is of the oxovanadyl type coordinated to four nitrogen atoms, as in the porphyrin macrocycle.

Poncet *et al.*[87] synthesized a VO ETIO compound with the four nitrogen atoms replaced by sulfur atoms. The EXAFS spectrum of this tetra-sulfur porphyrin ligand was dramatically different than the traditional VO ETIO spectra. When the spectra of VO ETIO were compared to those for authentic petroporphyrins, the spectra were nearly identical. Therefore, the vanadium compounds present in asphaltenes are unlikely to be coordinated to four sulfur atoms.

Berthe *et al.*[85] applied X-ray photoelectron spectroscopy (XPS or ESCA) to the analysis of vanadium compounds in heavy oils. They compared the binding energy of vanadium in both Cabimas and Boscan asphaltenes to the binding energy of vanadium in several model vanadyl compounds with different coordination environments. The binding energy of the vanadium in asphaltenes very closely matched that for the model compounds with a 4-N coordination environment. The binding energy observed with other coordination spheres (i.e., 4-O; 4-S; and various combinations of O, S, and N) showed binding energies significantly different than that of the asphaltene bound vanadium.

Looset *et al.*[88] compared the EXAFS spectra of a series of vanadyl porphyrins with varying types of substitution at the periphery of the porphyrin macrocycle: VO DPEP, VO ETIO, VOOEP, VO tetrabenzyl, VO tetrapyridine, etc. The effect of varying the size of the substituents but not location (e.g., ETIO vs OEP) was low for the V=O and V-N bonds and became significant at distances farther from the vanadyl center. Adding meso-tetrasubstitution (e.g., meso-tetraphenyl porphyrin) did have a slight impact on the magnitude of the V=O and V-N signals. These slight variations at the center of the porphyrin core arise due to slight distortions induced in the porphyrin macrocycle by the different substituents at the periphery.

The current research on "non-porphyrin" compounds is mainly focused on the determination of the average structure, and various researchers are also trying to find evidence at the molecular level. But no breakthrough discovery has been made so far. Based on the existing experimental results, it can be confirmed that all vanadium and nickel atoms in petroleum are with the core structure of porphyrin macrocycle with 4-N coordination.

Bouyssiere *et al.*[93] used size exclusion chromatography (SEC) combined with ICP-MS to analyze the molecular weight of metal compounds in asphaltenes and found that the most of metal compounds falls in the high molecular weight range (5000-40000 Da), as shown in Figure 1.2. The re-injected experiments revealed that dissociation of asphaltene aggregates and re-aggregation of LMW fraction occurring after the isolation. SEC-ICP-MS has a very important reference value for the research of petroleum asphaltenes to some extent, and it is clear that the results of the molecular weight of asphaltenes measured by size exclusion chromatography are different from the real results.

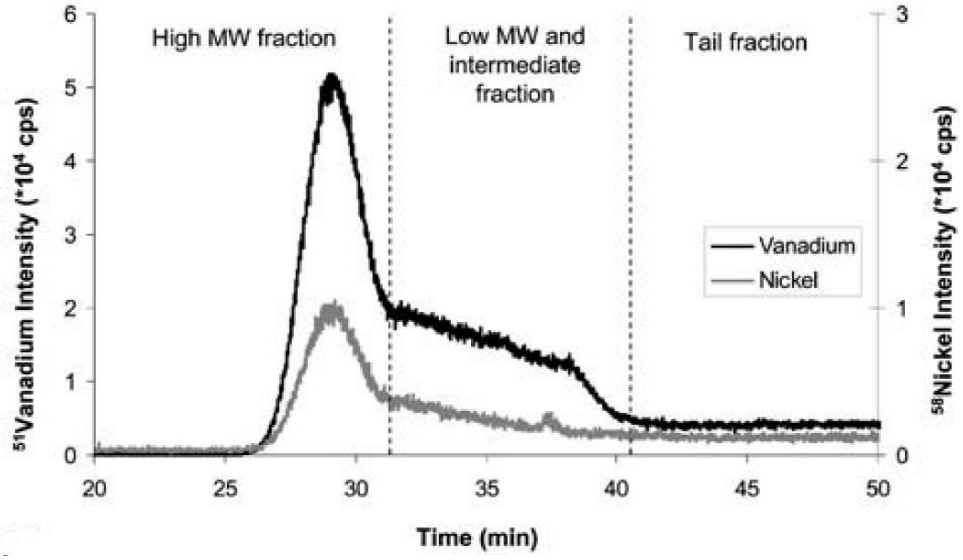

Figure 1.2 Chromatogram obtained by SEC-ICP MS of asphaltene sample[93]

We got an intuitive understanding of the aggregation of asphaltenes by the combination of chromatography and elemental analysis. There must be a strong aggregation between the metal porphyrins and asphaltene.[94-104] Of course, macromolecular metalloporphyrin compounds must also exist, that is, high carbon number and high degree of condensation. This can be directly observed through high-resolution mass spectrometry results.[78] The existence of coordination structure will also increase the apparent molecular weight of metalloporphyrins, and six-coordinate metalloporphyrin compounds are basically confirmed to be inevitable in petroleum.[105-109] The existence of porphyrin macromolecules in asphaltene formed by ether linkage or acyl group connection needs to be further confirmed.

1.3 Research progress of petroleum asphaltenes

The precipitation and filtration of asphaltenes is generally carried out using small molecules *n*-alkanes. The procedure performed by multifarious standard methods, and there are a variety of variants in use, as shown in Table 1.3. Each provides different results.[110-111]

Table 1.3 Variety of asphaltene precipitation methods

Method	Solvent	solvent/oil ratio	operating conditions	filter media
ASTM D-3279-07	n-heptane	100:1	reflux for 30 min, settle at ambient for 1 h, filter at 38-49 °C	fiberglass, 1.5 μm
ASTM D-4124-01	n-heptane	100:1	heat on steam bath for 30 min, settle at ambient overnight	slow/medium paper, ~10 μm
ASTM D-4124-09	iso-octane	100:1	reflux for 2 h, settle at ambient for 2 h	medium glass frit, 10 μm
WRI	n-heptane	40:1	heat to 80 °C for 5 min, stir at ambient for 16 h, settle for 30 min	medium glass frit, 10 μm
ASTM D-6560-00	n-heptane	30:1	reflux for 60 min, settle at ambient for 90-150 min	Whatman 42 paper, 2.5 μm
ASTM D-2007-03	n-pentane	10:1	settle at ambient for 30 min	rapid paper, 20 μm
IFP 9313 absorbance versus maltenes at 750 nm	n-heptane	20:1-200:1	heat to 80 °C for 5 min, filter at ambient	cellulose ester filter, 0.45 μm

1.3.1 Analysis method of asphaltenes

Asphaltenes as the most mysterious fraction in petroleum, whose properties have been studied for decades. Bulk properties of asphaltene such as element content, density, and thermogravimetric analysis, are known well and can be determined readily via correlative analytical instruments nowadays.[112-113] More comprehensive understanding of asphaltenes requires the utilization of utilization specialized analysis method, for example, NMR[114-115] and X-ray diffraction (XRD)[116] can be used to determine the average molecular parameters of asphaltenes, Vapor pressure osmometry (VPO) and Size exclusion chromatography (SEC) as well as mass spectrometry (MS) techniques can be used to measure the molecular weight distribution of asphaltenes. [117-120]

The molecular weight distribution (MWD) of asphaltenes has been measured and controverted for decades. Various methods were used to test the molecular mass of asphaltenes and the values differ by as much as 10 times or more. Vapor pressure osmometry (VPO) is a traditional method to measure the molecular weight of asphaltenes Normally, the values acquired from VPO are higher than those found with such mass spectrometry (MS) techniques because VPO required high analyte concentrations, in this case, asphaltene aggregation is known to occur.[117] Size exclusion chromatography (SEC) also could get a higher asphaltenes molecular weight value than that from MS due to the association phenomenon. However, a more-precise average MW can be obtained when using calibration curves based on chemicals that mimic in better ways the chemical functionalities of real petroleum fractions instead of the conventional polymer standards.[118, 121-122] Fluorescence decay and depolarization were once used to measure the molecular size and weight of asphaltenes by calibrating with known compounds.[123-124] However, the conclusions derived from these

techniques has been pointed wrong because they just sensitive to the fluorescent compounds but asphaltene fluorescence is a highly complex function with unknown concentrations of different, unknown components.[125-126] Laser desorption ionization (LDI) and/or matrix-assisted laser desorption ionization (MALDI) coupled with MS were also used to analyze the molecular weight distribution (MWD) of asphaltenes. The MWDs of asphaltenes investigated by LDI-MS have a monomer peaking at massed around 500 Da and a number-averaged WM of 800-1000 Da.[119-120] In 2008, Mullins and Marshall *et al.*[127] published a comprehensive paper on asphaltenes mass weight distribution determined by four molecular diffusion techniques and seven mass spectral techniques from many groups around the word. They concluded that all mass spectrometric measurements are in agreement with all molecular diffusion methods, yield the same MWD for petroleum asphaltenes, and this range has an average molecular weight of ~750 Da (±200 Da) with a fwhm 500-1000 Da.

In recent years, with the continuous development of mass spectrometry (MS) technology, MS, especially Ultra-high resolution (UHR) mass spectrometers, have indispensable tool for analyzing the chemical properties and molecular composition of asphaltenes.[128-130] ESI equipped FT-ICR MS has long been used to characterize the molecular composition of asphaltenes, as early as a decade ago. ESI preferentially ionizes heteroatoms-containing compounds, such as polar N-, S-, O- and Metal containing species. ESI FT-ICR MS has been widely used to analyze the molecular composition of heteroatomic compounds in asphaltenes and their corresponding saturates, aromatics and resins.[33, 131] In addition, it is also widely used in the research of petroleum porphyrin as well as geochemical porphyrin due to the good response of metalloporphyrins in ESI,.[53-54] Compared to ESI, APPI ionizes a wider range of compounds, including non-polar compounds.[132] The APPI ionization source may obtain some asphaltene composition information not seen by ESI, such as polycyclic aromatic hydrocarbons (PAHs).[133] So APPI is also widely used to characterize the molecular composition of petroleum asphaltenes and other components.[76, 134] Although the resolution of Orbitrap is not as high as that of FT-ICR, its resolution ability cannot be ignored, and its stronger isolation and collision capabilities have unique advantages in studying the molecular composition and structural information of asphaltenes.[135] In addition, other ionization techniques (e.g. APCI, APLI, LDI, MALDI, ASAP) equipped with Ultrahigh-resolution mass spectrometers also be applied to characterize the asphaltenes.[136-140]

Due to the limitations of molecular MS for the direct and quantitative identification of asphaltene compounds, inductively coupled plasma high resolution mass spectrometry (ICP HR-MS) is an efficient tool for studying the size distribution of vanadium-, nickel-, and sulfur-containing compounds in asphaltenes. When ICP MS is used to study asphaltenes, liquid chromatography (LC) is often used for on-line separation, and gel permeation chromatography (GPC) is the most commonly used column. Asphaltene solution (usually dissolved in tetrahydrofuran) will be separated into high-molecular-weight (HMW), medium-molecular-weight (MMW) and low-molecular-weight (LMW) after passing through GPC, and then analyzed online by

mass spectrometry and detected by UV or other detectors simultaneously.[93] Despite the criticisms that the GPC is subjected, coupling GPC with ICP MS enables the identification and quantification of the relative sizes associated with the various V, Ni, and S compounds in asphaltenes.[27] The re-injected experiments revealed that dissociation of asphaltene aggregates and re-aggregation of LMW fraction occurring after the isolation, as shown in Figure 1.3.[93]

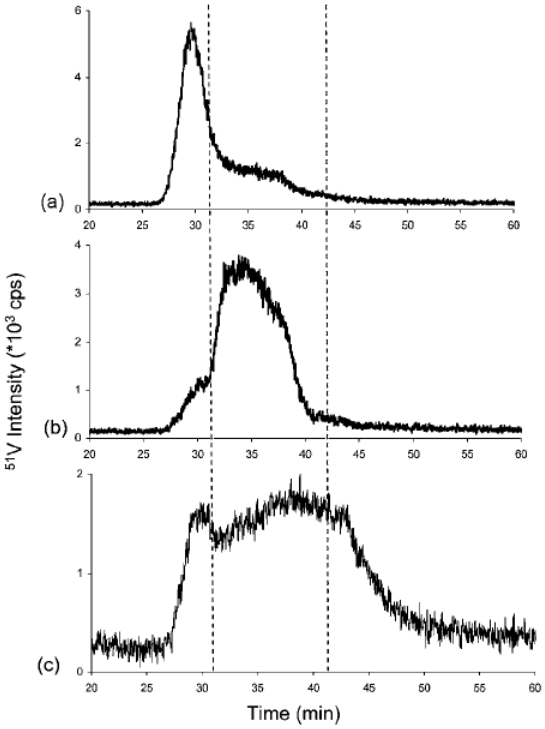

Figure 1.3 Chromatograms obtained by GPC-ICP MS of (a) HMW fraction: collected and reinjected; (b) MMW fraction: collected and reinjected; (c) LMW fraction: collected and reinjected[93]

Recently, high-resolution scanning probe microscopies have emerged as effective method for elucidating molecular structure. Scanning probe microscopy offers the unique capability of imaging single adsorbate at the atomic scale. The latest advances in atomic force microscopy (AFM) enabled the direct observation of individual asphaltene molecules. Schuler *et al.*[141] studied more than 100 asphaltene molecules using AFM and STM, and provided the direct measurement of the tremendous range of molecular structures in asphaltenes. The images of asphaltene molecules derived from coal and petroleum are shown in Figure 1.4. This work is groundbreaking in the history of asphaltenes, allowing us to have a direct visual understanding of the structure of some molecules in asphaltenes. This technique is also used to identify colloidal particles associated with asphaltene aggregates present in crude oils as well as model system.[142] AFM even allows for direct observation on specific structure of some biomarkers, such as the characterization of substitution patterns on petroporphyrins.[143] This technology constitutes a paradigm shift in the analysis of complex

molecular mixtures and may be applied to molecular electronics, organic light-emitting diodes, and photovoltaic devices.[141]

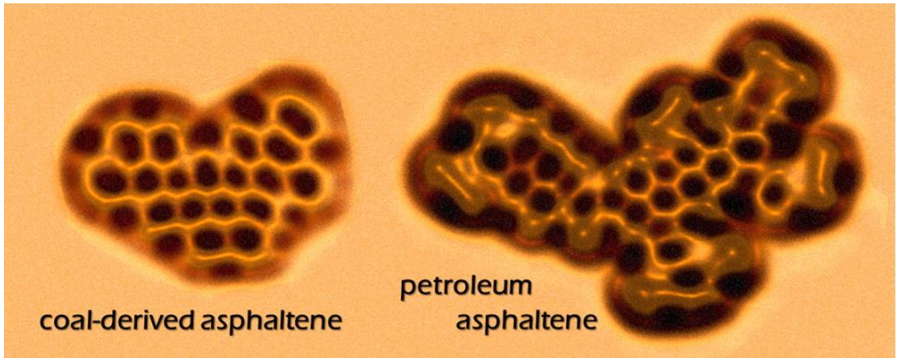

Figure 1.4 AFM images of coal-derived asphaltenes and petroleum asphaltenes[141]

1.3.2 Molecular theoretical model of asphaltene

Molecular aggregation is a common phenomenon encountered in many chemical and biochemical systems because of strong association interaction between molecules.[144] The size distribution of aggregate asphaltenes span a range of 1000-100000 g/mol in apparent molecular weight leading physical dimensions of 2-20 nm.[145] The driving forces contributing to aggregations include π-π stacking (electrostatic and/or van der Waals forces),[146] hydrogen bonding,[147] acid−base interactions,[148] and coordination interactions.[149] These aggregates are suspended stable in most unmodified crude oils and aromatic solvents such as toluene.[150] Deposition of asphaltene emerge when pressure,[151] temperature,[152] composition and shear rate change,[2, 153] which is responsible for operational problems related to well production and exploration,[154] oil transportation, oil refining and processing, and emulsion stabilization.[6-7, 155] It is generally acknowledged that asphaltene fractions aggregate to form nanoparticles and clusters throughout a range of concentration and temperature.[156] These aggregates dissociate with the decreasing of concentration and increasing of temperature.[157-158] In addition, metals and heteroatoms play an important role in aggregating of asphaltene.[147, 159]

Morphological study of asphaltene aggregates has been paid much attention by petroleum chemists for a long time.[18] Various morphologies have been proposed with the resort of mathematical functions and approximation model, such as colloidal/micellar, polymeric, solubility and modified Yen models.[160] With considerable consensus in various studies on the molecular structure of asphaltene aggregates, it can be concluded that the modified Yen model is the most suitable representation of aggregated asphaltenes.[159] Yen model was proposed by Professor Ten Fu Yen and coworkers in 1967 for accounting chemical moieties in asphaltenes[161] This model was modified by Mullins *et al.*[156] (2010) specifies the dominant molecular and colloidal structure of asphaltenes, and called as modified Yen model (also known as the Yen-Mullins Model). Figure 1.5 shows a graphical representation of this model. As it can be seen in the figure, these asphaltene molecules can form asphaltene nanoaggregates with less than six aggregation numbers.[156] In this model, the

basic force of aggregation comes from the attraction between the large aromatic cores of asphaltene molecules. Steric hindrance driven by peripheral substituents limits the molecular numbers of association. The interior attractive force and exterior repulsive force of asphaltene molecules lead to a low molecule number of nanoaggregate particles. These nanoaggregates can form asphaltene clusters. These clusters (less than 10 nm) are not much bigger than the nanoaggregates and quite small than flocs, which are micron scale.[162] Asphaltene clusters are likely fractal in their scaling with a much smaller binding energy compared with the nanoaggregate binding.[163] The modified Yen model shows considerable consistency with latter experimental results.[159] This model provides a convincible definition for nano and cluster aggregation of asphaltene molecules. Nevertheless, recent studies indicated that asphaltenes form primary aggregates at concentrations as low as ca. 0.7 mg/L, which is far below the value advocated by modified Yen model.[158]

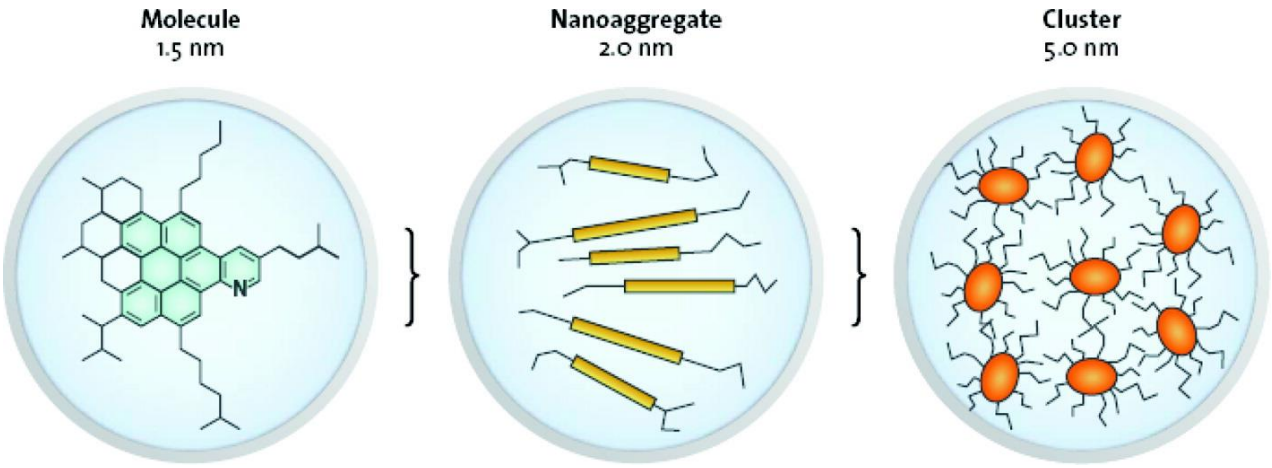

Figure 1.5 The modified Yen model[164-165]

Another model of asphaltene aggregates was proposed by Murray R. Gary *et al.*[146] They suggested that the general motifs of supramolecular assembly observed in simple mixtures are related to asphaltene aggregation, and the stoichiometry and thermodynamics of aggregation in complex petroleum mixtures. There will be no strong donor-acceptor interactions in petroleum, but large asphaltene molecules will produce multiple cooperative associations that combine acid-base interactions, hydrogen bonding, metal coordination, and hydrophobic pockets and aromatic π-π stacks. They took into account the known chemistry of petroleum and the canonical properties of asphaltene fractions. The schematic representation of a supramolecular assembly of this model is shown in Figure 1.6.

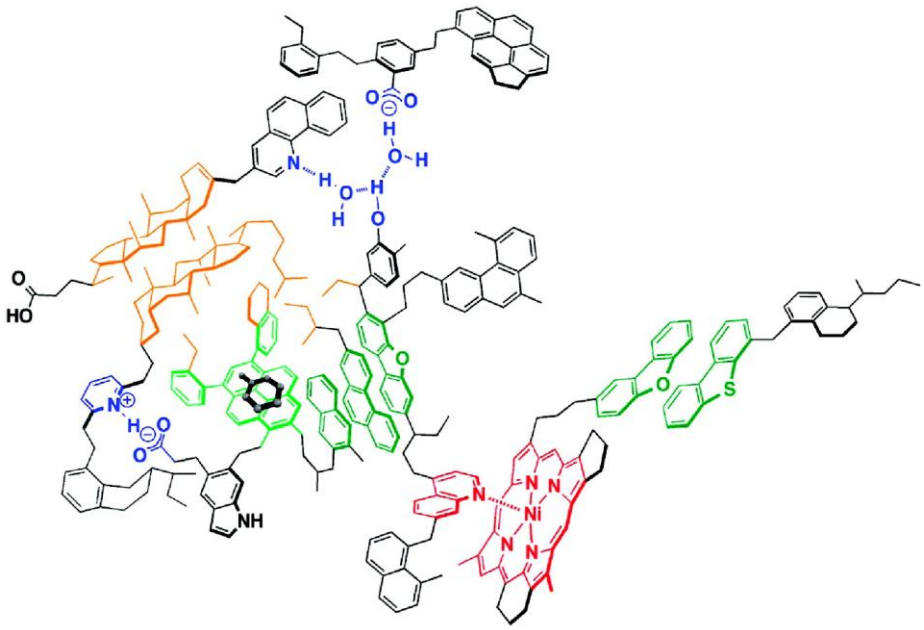

Figure 1.6 Supramolecular assembly model of asphaltene, proposed by Murray R. Gray[146]

Recently, Zhang *et al*[166] proposed a pancake bonding model for the interpretation of asphaltene aggregation behavior (Figure 1.7), which is consistent with the latest findings based on Fourier transform ion cyclotron resonance mass spectrometry and non-contact atomic force microscopy techniques. Various structural features of polycyclic aromatic hydrocarbons contribute to this interaction involving a stable free radical.

Figure 1.7 Pancake bonding model of asphaltene aggregation[166]

The heteroatoms in asphaltene, in the form of polar functional groups will inevitably unbalance the charge density, inducing permanent or partial dipoles that do not exist in non-polar fractions. The sulfur atoms

present as sulfides and thiophenes in asphaltenes increase the condensation extent of asphaltene molecules, and sulfide bridged bonds could expand the size of asphaltene molecules. Nevertheless, the sulfur-containing groups are only slightly polar and seem no contribution to intermolecular aggregation.[147] Unlike sulfur, oxygen and nitrogen-containing function groups in asphaltenes are generally polar and competent in participating in strong intermolecular aggregation. Nitrogen atoms in the form of pyrrolic and pyridinic as well oxygen present as phenolic and carboxylic acid are responsible for hydrogen bond accepter and donor species.[159] Polycyclic compounds containing pyridine functional groups were investigated to study the influence of both aromatic and aliphatic parts of asphaltene molecules on their aggregation via determining the association free energies. It was illuminated that the heteroatoms residing in the aromatic core significantly affected the interaction strength than the ones connected to the aliphatic side chains. The heteroatoms dwell in polycyclic core can impact the electronic cloud density which alter the associative strength.[167] Nitrogen and oxygen are more electronegativity than carbon, which can enhance the electrostatic attraction in both isolated and solvent environment leading to the aggregation of asphaltenes via hydrogen bonds.[168-169] The interactions of metalloporphyrins concentrated in the asphaltene fraction appear to play a pivotal role in the aggregation of asphaltenes.[147]

1.4 Literature summary and research tasks of this thesis

According to the literature research, the following conclusions can be drawn:

(1) A comprehensive understanding of the composition and properties of asphaltenes is of great significance to the entire petroleum industry; (2) The existence of metal compounds in petroleum and asphaltenes requires more in-depth research; (3) In-depth understanding of molecular composition is an important to study the existence of asphaltenes; (4) Modern analysis techniques such as high-resolution mass spectrometry provide technical conditions for the analysis of petroleum molecular composition. The analysis of heteroatom compounds and metal compounds in asphaltenes is of great significance.

The main research content of this paper:

Based on the previous literature research and laboratory sample conditions, several representative petroleum samples were selected to explore the molecular composition of metal compounds in asphaltenes as well the existence of asphaltenes.

Chapter 2. Molecular composition of SFEF fractions of Canadian oilsands bitumen

2.1 Introduction

Instrumental analysis on asphaltenes is significant to obtain their physicochemical properties. Furthermore, combined with effective pretreatment, such as fractionation of asphaltene, further information on the molecular composition would be obtained. As asphaltene is the most complex component in petroleum, in order to study the physicochemical properties and structural composition of asphaltene more deeply, various researches tried numerous methods to divide asphaltene into a series of narrow fractions, and comparatively analyzed their physical and chemical composition. Asphaltene itself is defined by the solubility in solvents, that is, components in petroleum that are soluble in toluene or benzene, but insoluble in saturated hydrocarbons such as n-heptane. Asphaltenes are also "non-distillable" components, so the separation of asphaltenes is usually based on solubility. In addition to the separation of asphaltenes based on other physical and chemical methods are also used to separate asphaltenes. With the development of analytical methods and technologies, even matrices as complex as asphaltenes, could be separated with simple, effective, and rapidly methods, and even online fractionation methods have emerged. The methods used to separate asphaltenes mainly include: SEF(sequential elution fractionation) method[170-171], solvent extraction[27, 172], sequential extraction[173-174], column chromatographic fractionation[175-176], sequential precipitation[147, 177], on-column method[178], ultracentrifugation[163, 179], SFE(supercritical fluid extraction)[180-181], ultrafiltration fractionation[182-183], adsorption onto porous medium[184-186] and microwave Treatment[187]。

The separation of asphaltenes into fractions has two major advantages: it reduces the complexity of the research materials and provides a properties distribution rather than just averages. Based on the continuity model, this strategy has been successfully applied to improve the characterization of asphaltenes and shows regular changes in the performance of different fractions. Generally, fractions with lower solubility show decreased H/C ratio and increased aromaticity and heteroatom content.

Supercritical fluid extraction fractionation (SFEF) has been proven to effectively separate heavy petroleum fractions and asphaltenes.[181] As one of the largest oil reservoir resources in the world, Canadian oil sand bitumen has very important strategic significance. In this study, the VR of Canadian oil sands bitumen was used as the research object. After being separated into 14 fractions by the SFEF method, the molecular composition was analyzed by high-resolution mass spectrometry and compared with Venezuelan VR.

2.2 Materials and methods

2.2.1 Materials

The oilsands bitumen was obtained from a commercial in-situ operation in Northern Alberta and subjected to pilot scale vacuum distillation to yield a distillate and 500°C$^+$ VR fraction. The VR was further fractionated into 13 extractable narrow fractions and an unextractable end-cut by SFEF using pentane solvent. The experimental setup and operating procedure of SFEF have been described elsewhere [188]. Analytical reagent grade solvents, toluene and methanol were purified by distillation, prior to use in preparing samples for analyses.

2.2.2 ESI FT-ICR MS analysis

The SFEF fraction (10 mg) was mixed with 1 mL of toluene. The mixture solution (20 μL) was diluted with 1 mL of toluene/methanol (1:3) solution, followed by adding 15 μL of an aqueous solution of ammonium hydroxide (28-35 wt%) as an ionization promoter for negative-ion ESI. Correspondingly, 10 μL of HCOOH were added as an ionization promoter for positive-ion ESI. The sample solution was injected via an Apollo II electrospray source at 180 μL/h and analyzed using a Bruker apex-ultra FT-ICR MS equipped with a 9.4 T superconducting magnet. The operating conditions of negative-ion ESI FT-ICR MS were 4.1 kV spray shield voltage, 4.6 kV capillary column front end voltage and -320 V capillary column end voltage. The ions were accumulated in a hexapole for 1 ms. The DC voltage was -3.0 V with 500 Vpp RF amplitude and 1.2 ms delay was selected to transfer to the ICR cell. Optimized mass for Q1 was *m/z* 200. The ions accumulated in Qh-Interface was 2 s with 5 MHz Hexapoles and 500 Vp-p RF amplitude. The ICR cell was 13.5 dB attenuation and 200-1000 Da mass range was selected. The data size set was 4M with 64 scans co-added, resulting in a resolving power of 400,000 at *m/z* 500. The operating conditions of positive-ion ESI FT-ICR MS were -3.5 kV spray shield voltage, -3.0 kV capillary column front end voltage, and 280 V capillary column end voltage. The ions accumulated in a hexapole for 0.1 s. The DC voltage was 2.0 V with 350 Vpp RF amplitude and 1.3 ms delay was selected to transfer to the ICR cell. Optimized mass for Q1 was *m/z* 200. The ion accumulated in Qh-Interface was 2 s with 5 MHz Hexapoles and 400 Vp-p RF amplitude. The ICR cell was set to 1.3 ms and 12.1 dB attenuation and 200-1000 Da mass range was selected. The data size set was 4 M with 64 scans co-added, resulting in a resolving power of 400,000 at *m/z* 500.

2.2.3 Mass calibration and data analysis

The mass spectrum peaks were calibrated using a crude oil and the mass errors were less than 1 ppm. Internal calibration was carried out using the identified homologous series of N_1 compounds. Peaks with relative abundance greater than 5 times the standard deviation of the baseline noise were selected and analyzed using the in-house software, which has been described elsewhere.[189] Species with the same heteroatom class and

its isotopes with different double bond equivalent (DBE) values and carbon numbers were searched within a set ±0.001 Kendrick mass defect (KMD) tolerance.[189]

2.3 Results and discussion

2.3.1 Properties of VR and its SFEF fractions

Table 2.1 shows the properties of oilsands derived VR and its SFEF fractions. The extractable SFEF fractions accounted for 67 wt% of VR. The molecular weight (MW) of extractable SFEF fractions increased from 500 to 1000 Da. The unextractable end-cut with high molecular weight of 3000 Da determined by vapor pressure osmometry is likely due to molecular aggregation.[144] As the SFEF fraction became heavier, the hydrogen-to-carbon (H/C) ratio of SFEF fraction decreased, and the density, sulfur, nitrogen, Conradson carbon residue (CCR) and metals contents increased.

The bulk vanadium concentration of VR was very high at 318 wppm. In the SFEF fractions, the vanadium concentration increased gradually in the extractable SFEF fractions; 9.9 wppm in SFEF1, 211 wppm in SFEF11, 388 wppm in SFEF13, and increased abruptly to 865 wppm in the unextractable end-cut. The trend of nickel concentrations in SFEF fractions was similar to that of vanadium. In general, the properties of VR and its SFEF fractions were similar to those reported for mined oilsands derived VR [188].

Table 2.1. Properties of the VR and its SFEF fractions

	extract pressure (Mpa)	yield (wt%)	cumulative yield (wt%)	H/C	C[a] (wt%)	H[a] (wt%)	S[b] (wt%)	N[c] (wt%)	Ni[d] (ppm)	V[d] (ppm)	CCR[e] (wt%)	Density @20 °C[f] (g/cm^3)	Molecular weight (VPO)[g]
VR			100	1.41	82.5	9.75	6.18	0.77	120	318	25.02	1.0516	966
SFEF1	5.43	5.14	5.14	1.61	84.21	11.38	3.66	0.31	4	9.9	2.44	0.97	467
SFEF2	6.01	5.01	10.15	1.63	83.91	11.45	3.86	0.35	4.7	10.8	3.96	0.98	546
SFEF3	6.38	5.06	15.21	1.62	84.12	11.45	4.04	0.4	5.5	8.9	3.98	0.98	568
SFEF4	6.92	5.09	20.3	1.59	83.66	11.18	4.27	0.44	4.6	6.5	4.27	0.99	580
SFEF5	7.16	5.08	25.38	1.58	83.66	11.11	4.49	0.48	6.6	13.1	6.14	0.99	600
SFEF6	7.61	5.18	30.56	1.56	83.34	10.93	4.81	0.53	10.8	21.8	7.77	0.99	636
SFEF7	8.15	5.19	35.75	1.53	84.05	10.76	5.08	0.62	17	34.5	9.11	1.01	673
SFEF8	8.37	5.11	40.86	1.52	82.84	10.54	5.29	0.7	29.9	65.9	12.09	1.02	802
SFEF9	8.74	5.0	45.86	1.51	82.88	10.51	5.65	0.78	40.7	85.7	14.07	1.03	873
SFEF10	9.34	5.06	50.92	1.48	82.46	10.23	5.89	0.86	57.9	125.1	17.12	1.03	901
SFEF11	10.02	5.08	56	1.44	82.14	9.95	6.43	0.97	85.3	210.7	20.7	1.03	927
SFEF12	11	5.06	61.06	1.42	81.87	9.7	6.53	1.0	117.9	256	25.1	1.03	1055
SFEF13	12	5.04	66.1	1.39	81.34	9.46	7.07	1.21	156.3	388.1	31.16	1.07	1012
End-cut	N/A	31.9	98	1.29	80.91	8.77	7.93	1.64	374.4	864.6	46.59	N/A	3036

[a]ASTM D5291 (flash EA 1112 analyzer). [b]ASTM D5453 (Antek 7000 elemental analyzer). *c*ASTM D5762 (Antek 7000 elemental analyzer). [d]ASTM D5708 (Vista-PRO simultaneous ICP−OES). [e]ASTM D189 (Shanghai Yutong Instrument YT-30011). [f]ASTM D1480 (pyonometer). [g]VPO were determined by Knauer K-7000.

2.3.2 Molecular composition characterized by negative-ion ESI FT-ICR MS

Figure 2.1 shows the negative-ion ESI FT-ICR MS broadband spectrum of fraction SFEF1 at *m/z* 200-1000. The insert is the close-up view of expanded mass spectrum at *m/z* 472 (randomly selected for illustration purposes) which shows a mass resolution power of 300,000. The high-resolution mass spectrum provides distinct assignments of compounds with unique elemental compositions. The even-mass peaks at *m/z* 450-700 indicated that the dominant compounds were O_2 and N_1 class species.

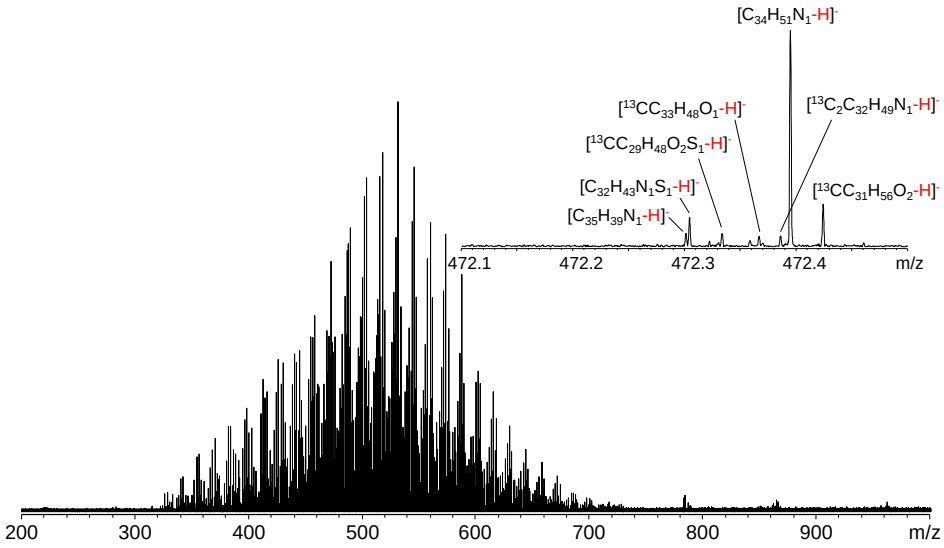

Figure 2.1. Negative-ion ESI FT-ICR MS broadband spectrum of SFEF fraction SFEF1. The insert is the expanded mass spectrum at *m/z* 472

Figure 2.2 shows the negative-ion ESI FT-ICR MS broadband spectra of various SFEF fractions. The abundant peaks were located at *m/z* 400-600 range. As the SFEF fraction became heavier, the mass distribution range shifted slightly to the right. The mass spectrum of the non-extractable SFEF end-cut was distinctly different from those of extractable SFEF fractions (SFEF1-13). Low peak intensities indicated that high molecular weight species in the SFEF end-cut were insufficiently ionized. The signal intensities of extractable SFEF fractions also showed that ionization efficiency decreased slightly as the SFEF fraction became heavier.

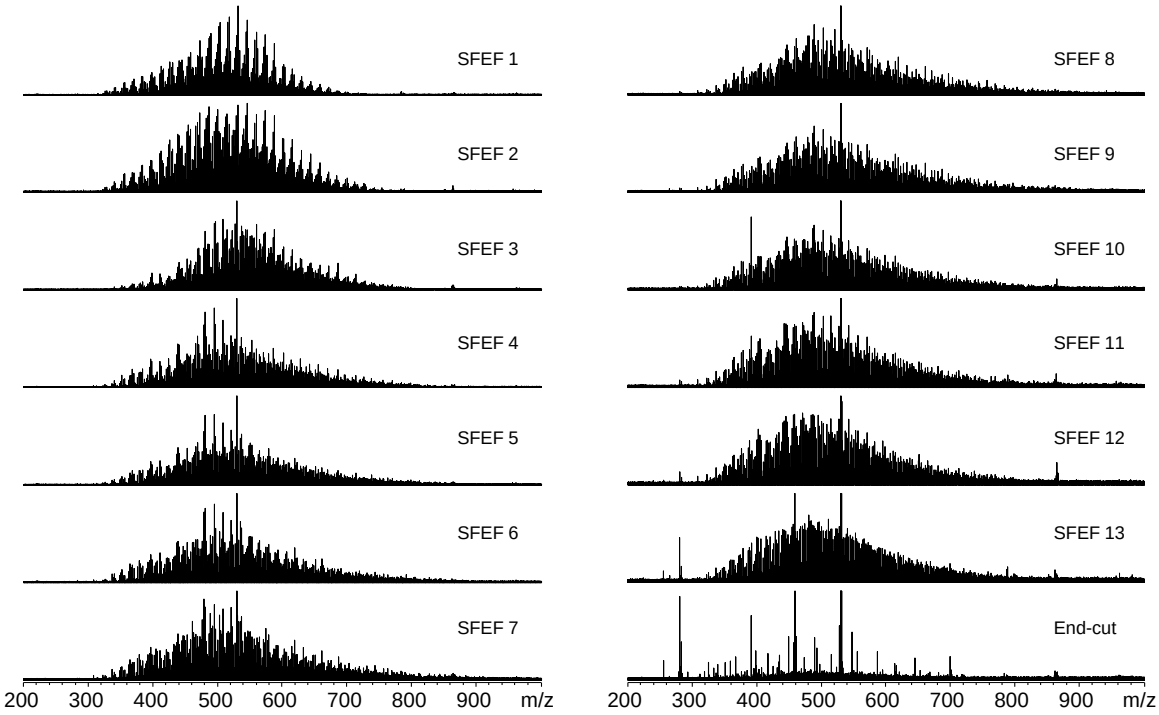

Figure 2.2 Negative-ion ESI FT-ICR MS broadband spectra of various SFEF fractions

Figure 2.3 shows the close-up view of expanded mass spectra of various SFEF fractions at *m/z* 472. The differences in molecular composition among the SFEF fractions were distinct, indicating the effectiveness of SFEF in separating VR into multiple narrow fractions. In SFEF1, $[C_{34}H_{51}N_1\text{-}H]^-$ with 10 DBEs was the most abundant, followed by $C_{32}H_{43}N_1S_1\text{-}H]^-$ and $[C_{35}H_{39}N_1\text{-}H]^-$ with 17 DBEs. However, the abundance of $[C_{34}H_{51}N_1\text{-}H]^-$ decreased dramatically in heavier SFEF fractions and was substituted by $[C_{35}H_{39}N_1\text{-}H]^-$, indicating that heavy SFEF fractions were more aromatic. The abundances of $[C_{34}H_{35}N_1O_1\text{-}H]^-$, $[C_{33}H_{31}N_1O_2\text{-}H]^-$, $[C_{33}H_{31}N_1S_1\text{-}H]^-$ and $[C_{32}H_{27}N_1O_1S_1\text{-}H]^-$ increased in the heavier SFEF fractions, indicating that the relative abundance of the multifunctional group class, such as N_1O_1, N_1O_2, N_1S_1, and $N_1O_1S_1$ increased as the SFEF fraction became heavier.

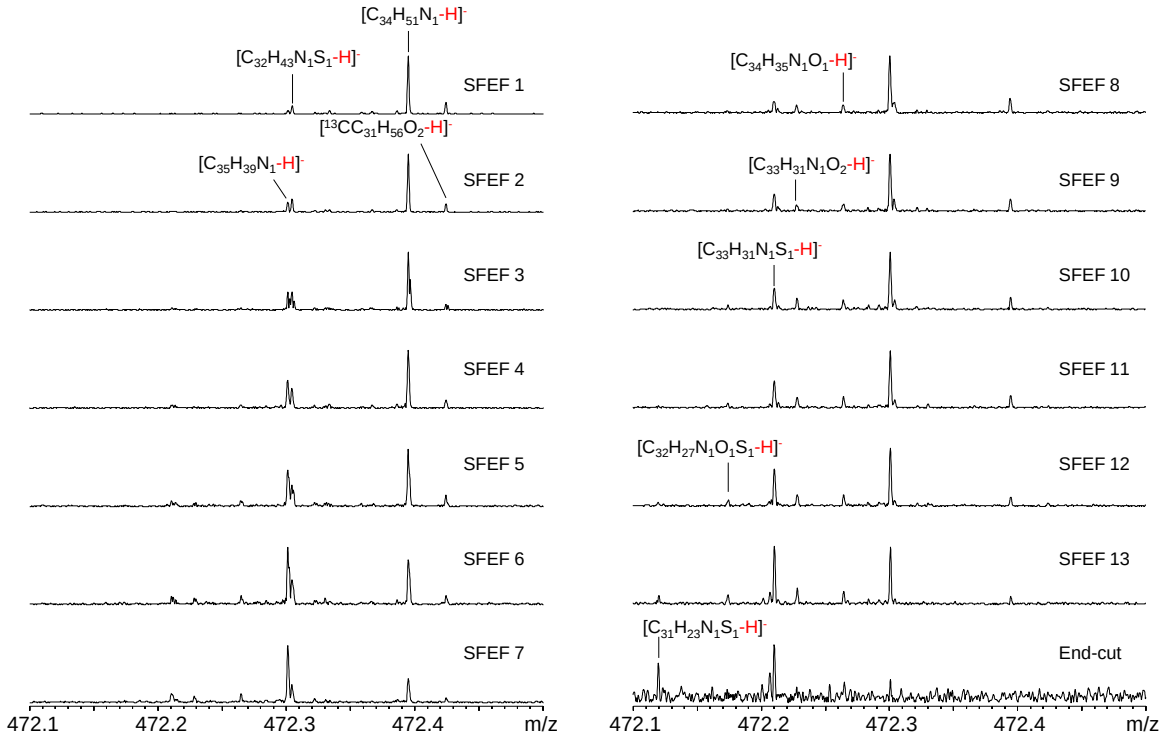

Figure 2.3 Expanded negative-ion ESI FT-ICR MS spectra of various SFEF fractions at m/z 472

Figure 2.4 shows the relative ion abundance plots of DBE as a function of carbon number for pyrrolic compounds (N_1-class species) in various SFEF fractions. The dots in the plots denote the abundance of species. Pyrrolic compounds can be easily ionized by negative-ion ESI. Data in Figure 2.4 showed that the distribution of pyrrolic compounds shifted diagonally to top-right, indicating that the pyrrolic compounds in heavier SFEF fractions were larger (higher carbon numbers) and more condensed (higher DBE values) molecules. The most abundant pyrrolic compounds in SFEF1 had 10 DBEs and 33 carbons, whereas those in SFEF13 had 20 DBEs and 37 carbons. Even though SFEF end-cut was insufficiently ionized, the data in Figure 2.4 showed that the pyrrolic compounds in SFEF end-cut were the homologous pyrrolic compounds as found in the extractable SFEF fractions, but with higher DBEs and carbon numbers.

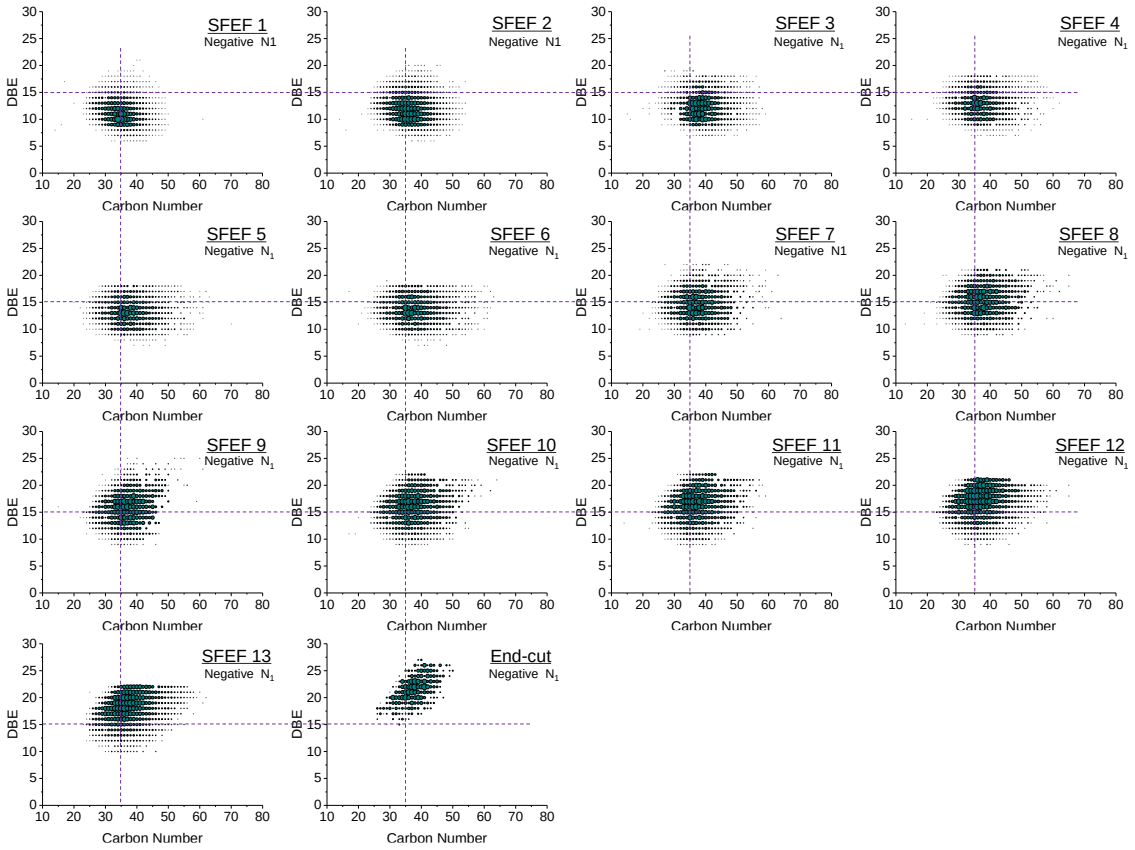

Figure 2.4 Relative ion abundance plots of DBE as a function of carbon number derived from negative-ion ESI FT-ICR mass spectra for N_1 class species (pyrrolic compounds) in various SFEF fractions

Figure 2.5 shows the relative ion abundance plots of DBE as a function of carbon number for O_2-class species in various SFEF fractions. Compared to data in Figure 2.4, the trend of distribution of O_2-class species in the SFEF fractions was different from that of pyrrolic compounds. The O_2-class species in SFEF fractions were centered at 30-40 carbon numbers and their DBE increased as SFEF fraction became heavier, indicating a vertical shift in distribution of O_2-class species in heavier SFEF fractions.

The DBE variation of O_2-class species in SFEF fractions was inconspicuous, since the number of naphthenic rings has relatively low impact on the polarity of a molecule as compared to aromatic rings. As for the end-cut, the series with DBE=1 was corresponding to fatty acids which were contaminants commonly found in negative ion ESI analysis.

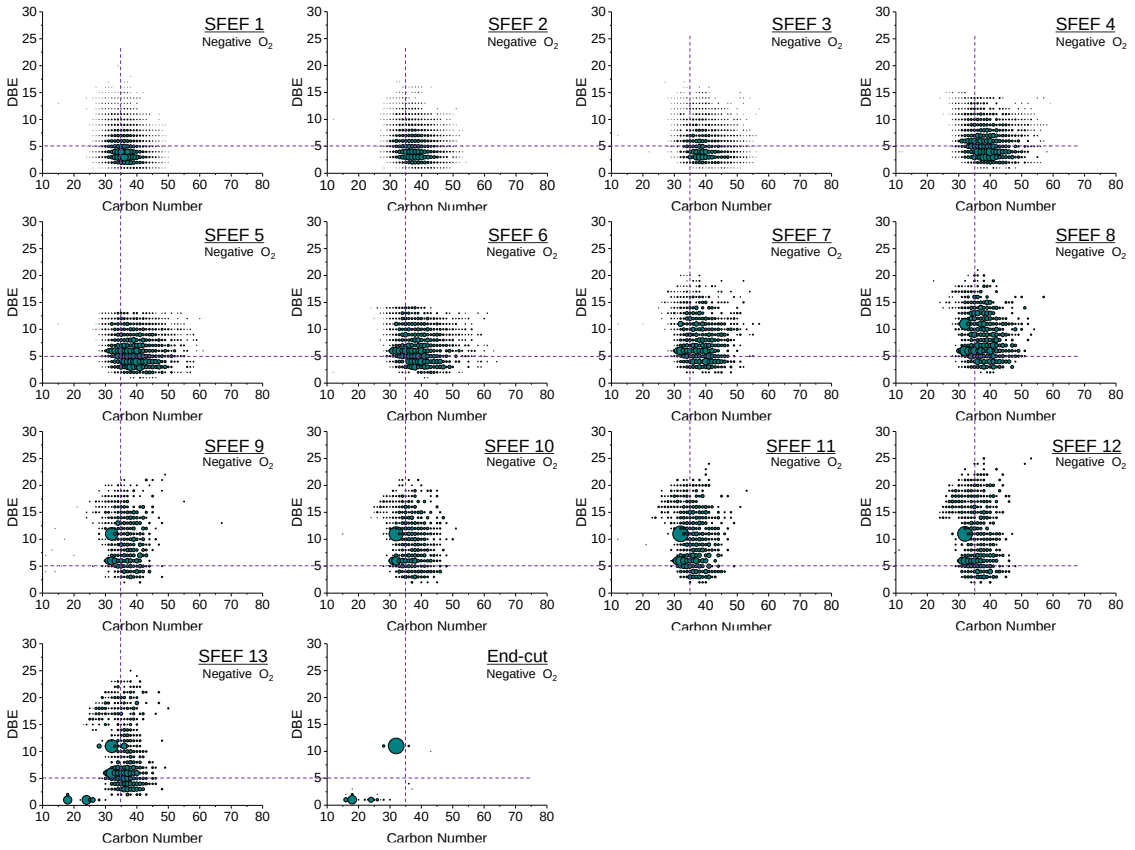

Figure 2.5 Relative ion abundance plots of DBE as a function of carbon number derived from negative-ion ESI FT-ICR mass spectra for O_2 class species in various SFEF fractions

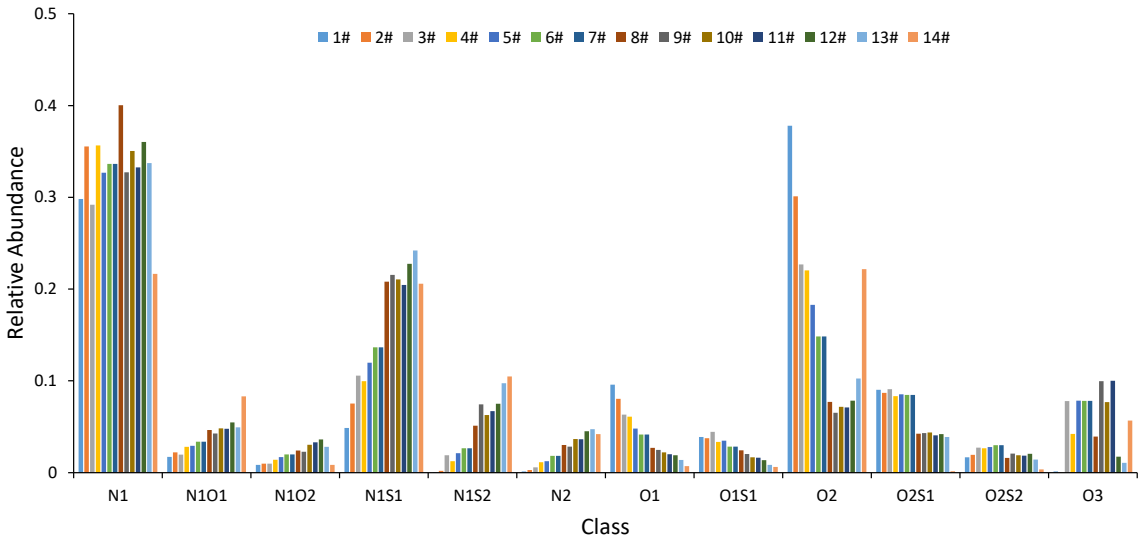

Figure 2.6 Relative abundance of heteroatom class species assigned from negative-ion ESI FT-ICR mass spectra of various SFEF fractions

Figure 2.6 shows the relative abundance of heteroatom class species in various SFEF fractions by negative-ion ESI FT-ICR MS. Twelve class species were assigned, namely N_1, N_1O_1, N_1O_2, N_1S_1, N_1S_2, N_2, O_1, O_1S_1, O_2, O_2S_1, O_2S_2, and O_3. Among them, N_1 class species were the most abundant. The abundances of multifunctional group compounds, such as N_1O_1, N_1O_2, N_1S_1, N_1S_2, and N_2 class species, increased as the fraction became heavier.

2.3.3 Molecular composition characterized by positive-ion ESI FT-ICR MS

Figure 2.7 shows the positive-ion ESI FT-ICR MS spectra of various SFEF fractions. Basic compounds, such as pyridines, sulfoxides, and metal porphyrin compounds, can be ionized by positive-ion ESI. As the SFEF fraction became heavier, the mass distribution range of mass spectra shifted slightly to the right. The mass peaks of SFEF12, SFEF13, and end-cut were sparse. This could be due to the low ionization efficiency or suppressed by the high responses of vanadyl porphyrins. The most abundant peaks at *m/z* 450-700 in SFEF12, SFEF13, and end-cut were vanadium compounds. More detailed discussion on these compounds will be in the following section.

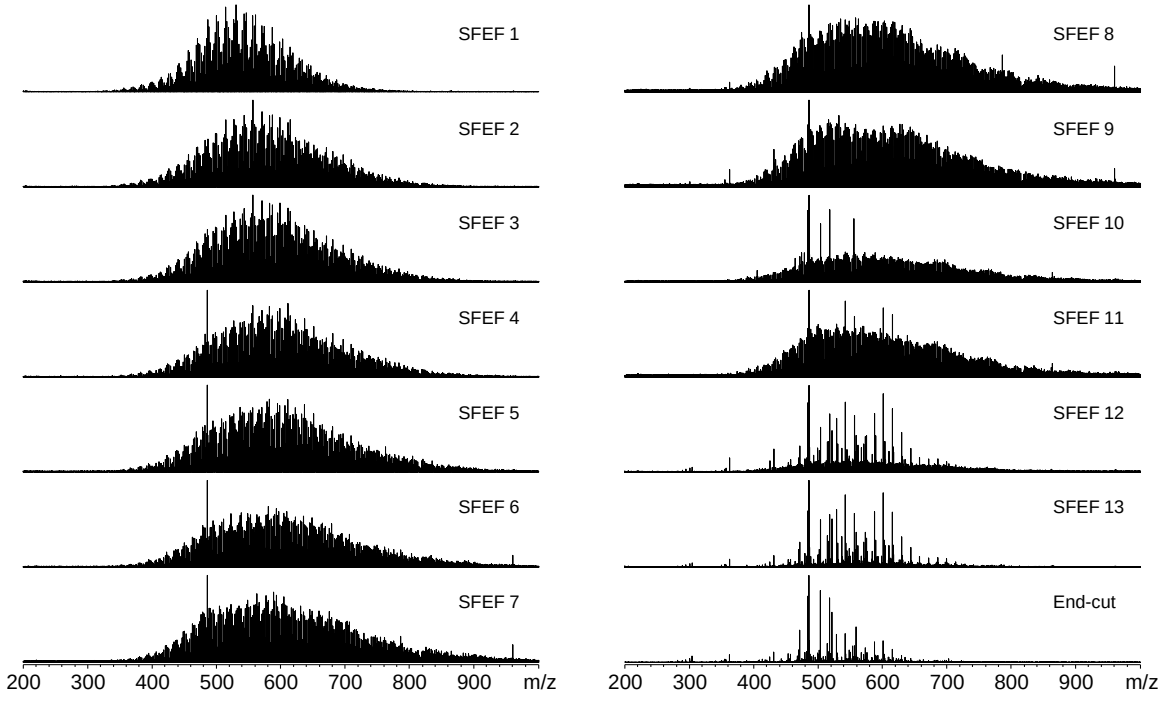

Figure 2.7 Broadband positive-ion ESI FT-ICR mass spectra of various SFEF fractions

Figure 2.8 shows the expanded mass spectra of various SFEF fractions at *m/z* 542. The differences in molecular composition among the SFEF fractions were distinct. The peak of $[C_{39}H_{59}N_1+H]^+$ with 11 DBEs was dominant in the light SFEF fractions, but decreased in the heavy SFEF fractions, and was substituted by $[C_{40}H_{47}N_1+H]^+$ with 18 DBEs in SFEF8, SFEF9, and SFEF10, indicating more highly aromatic compounds in heavier SFEF fractions. In SFEF12, SFEF13, and end-cut, $[C_{32}H_{34}N_4O_1V_1+H]^+$ was predominant. The

relative abundances of multifunctional group class species, such as N_1O_1, N_1O_2, N_1S_1, and N_1S_2 increased as SFEF fraction became heavier.

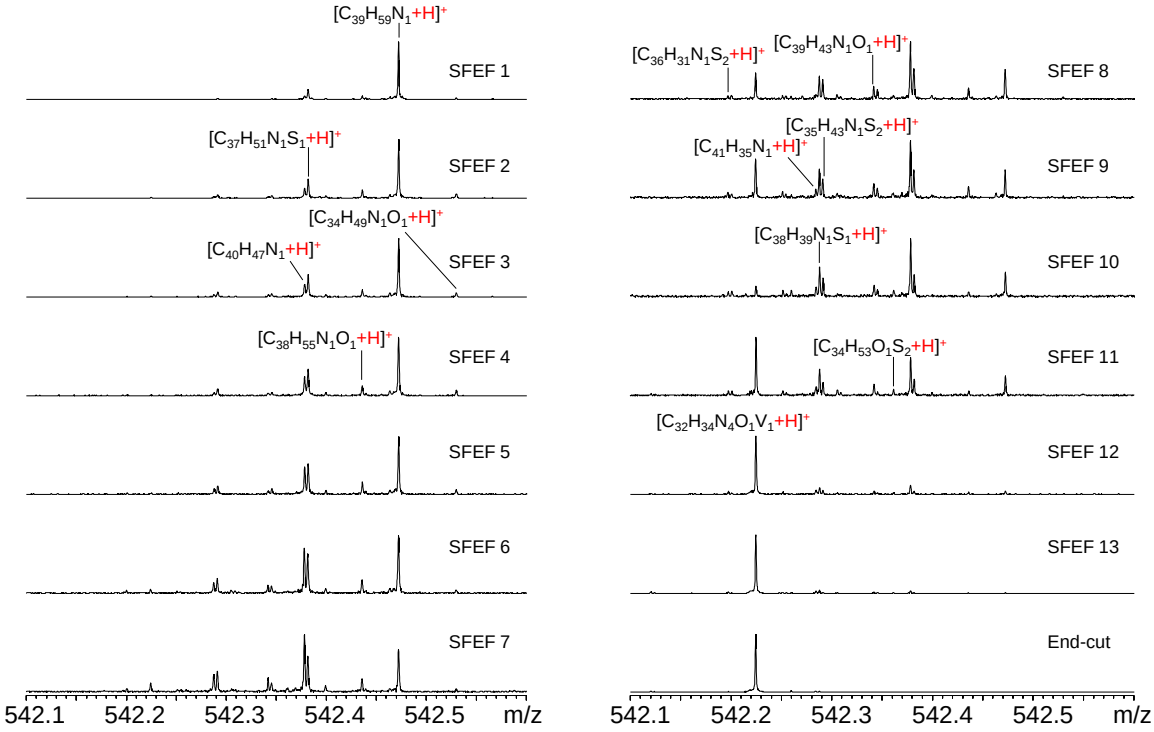

Figure 2.8 Expanded positive-ion ESI FT-ICR mass spectra of various SFEF fractions at *m/z* 542

Figure 2.9 shows the relative ion abundance plots of DBE as a function of carbon number for N_1-class species in various SFEF fractions. The N_1-class species, such as pyridine derivative compounds, are basic nitrogen compounds, since amines are rarely present in petroleum crude. The N_1-class species in SFEF fractions contained 30-50 carbons. The minimum DBE value for basic nitrogen species in SFEF fractions was 4, which is consistent with DBE value of pyridines. The N_1-class species with higher than 4 DBE are likely a pyridine unit attached to naphthenic rings. The size of DBE distribution of N_1-class species in SFEF fraction expanded as the SFEF fraction became heavier.

Figure 2.10 shows the relative ion abundance plots of DBE as a function of carbon number for N_1S_1 class species in various SFEF fractions. The N_1S_1-class species are likely an N_1-class species attached to a S_1-functional group. The DBE distribution patterns of N_1S_1 class species of SFEF fractions were similar to those of N_1-class species shown in Figure 2.9.

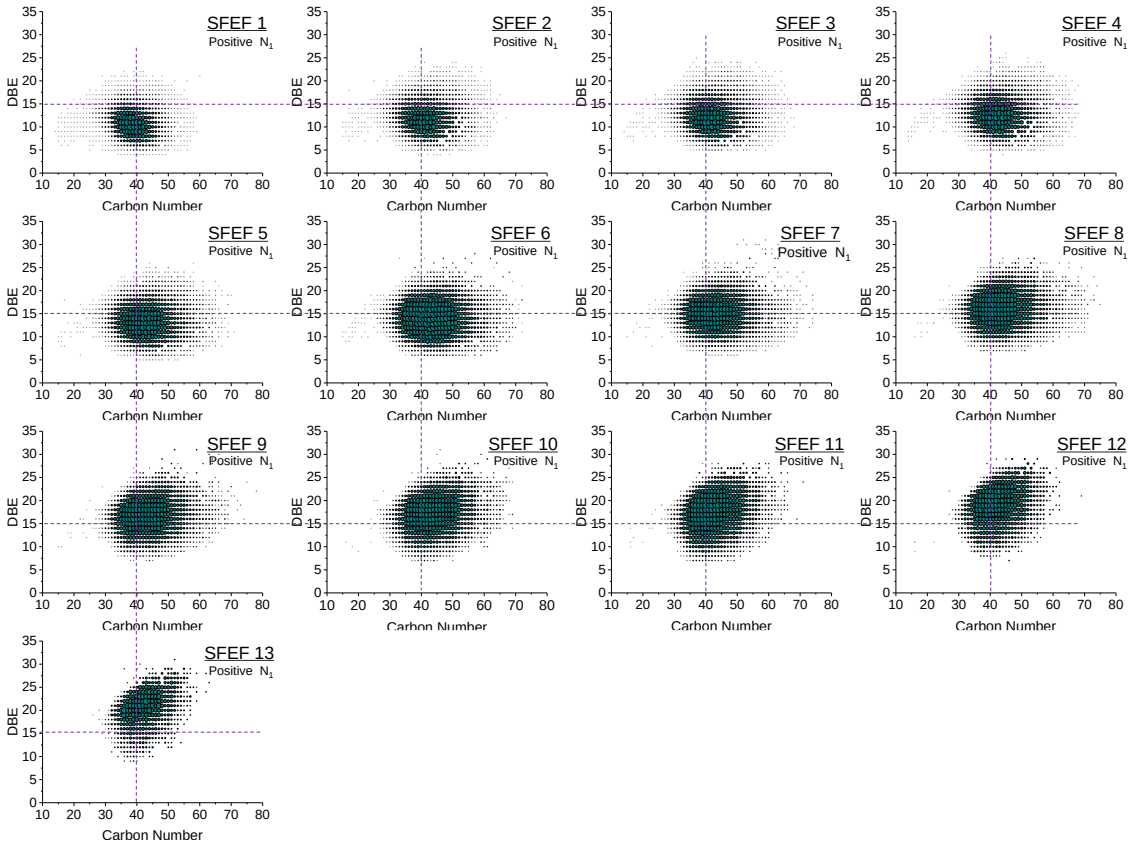

Figure 2.9 Relative ion abundance plots of DBE as a function of carbon number derived from positive-ion ESI FT-ICR mass spectra for N_1-class species in various SFEF fractions. No N_1 compounds were detected in the end-cut

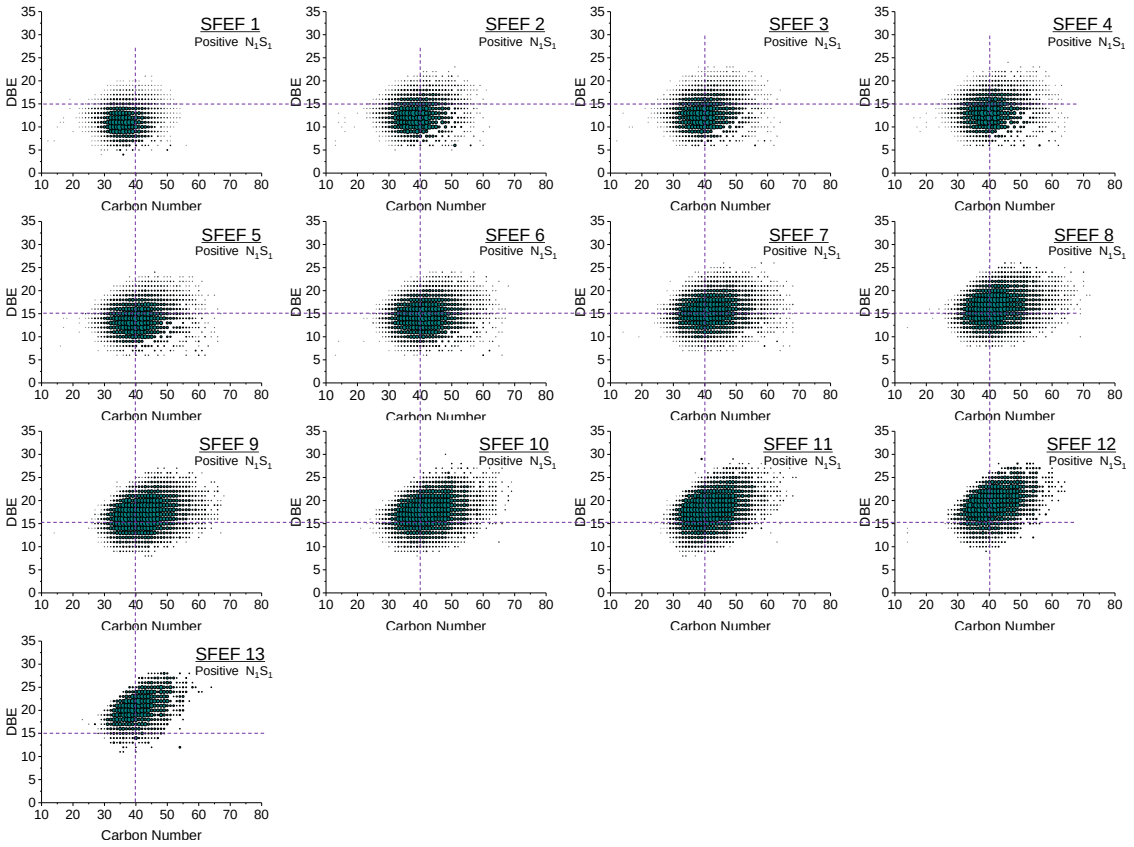

Figure 2.10 Relative ion abundance plots of DBE as a function of carbon number derived from positive-ion ESI FT-ICR mass spectra for N_1S_1-class species in various SFEF fractions. No N_1S_1 compounds were detected in the end-cut

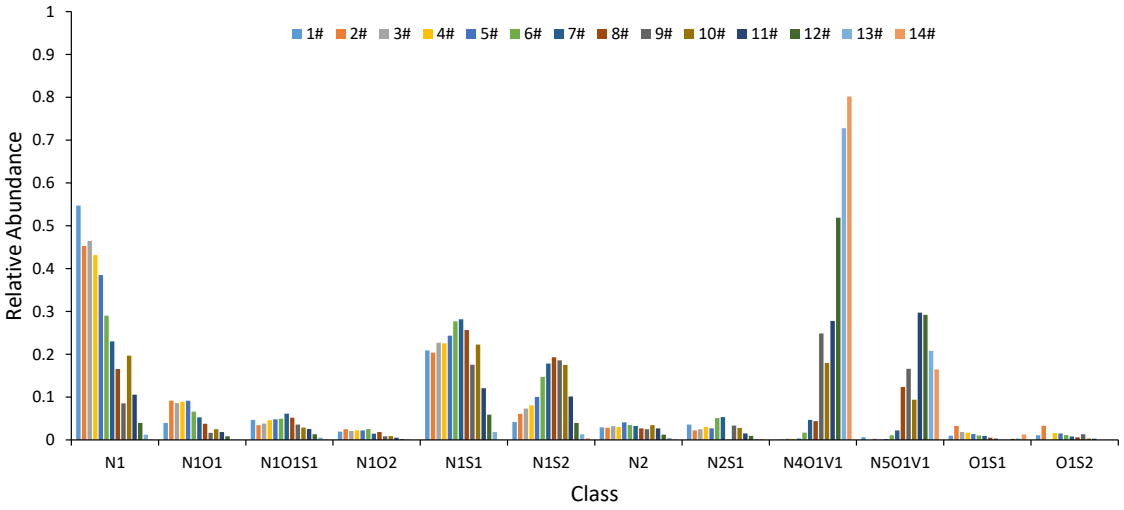

Figure 2.11 Relative abundance of heteroatom class species assigned from positive-ion ESI FT-ICR mass spectra of various SFEF fractions

Figure 2.11 shows a total of 12 class species, such as N_1, N_1O_1, $N_1O_1S_1$, N_1O_2, N_1S_1, N_1S_2, N_2, N_2S_1, $N_4O_1V_1$, $N_5O_1V_1$, O_1S_1, and O_1S_2 compounds, were identified by positive-ion ESI FT-ICR in various SFEF fractions. The relative abundance of N_1 class species decreased gradually as the SFEF fraction became heavier and disappeared in the end-cut. Conversely, the relative abundance of $N_4V_1O_1$ increased dramatically from 0.1% in SFEF1 to 73% in SFEF13, and 80% in the end-cut.

2.3.4 Vanadium compounds in SFEF fractions

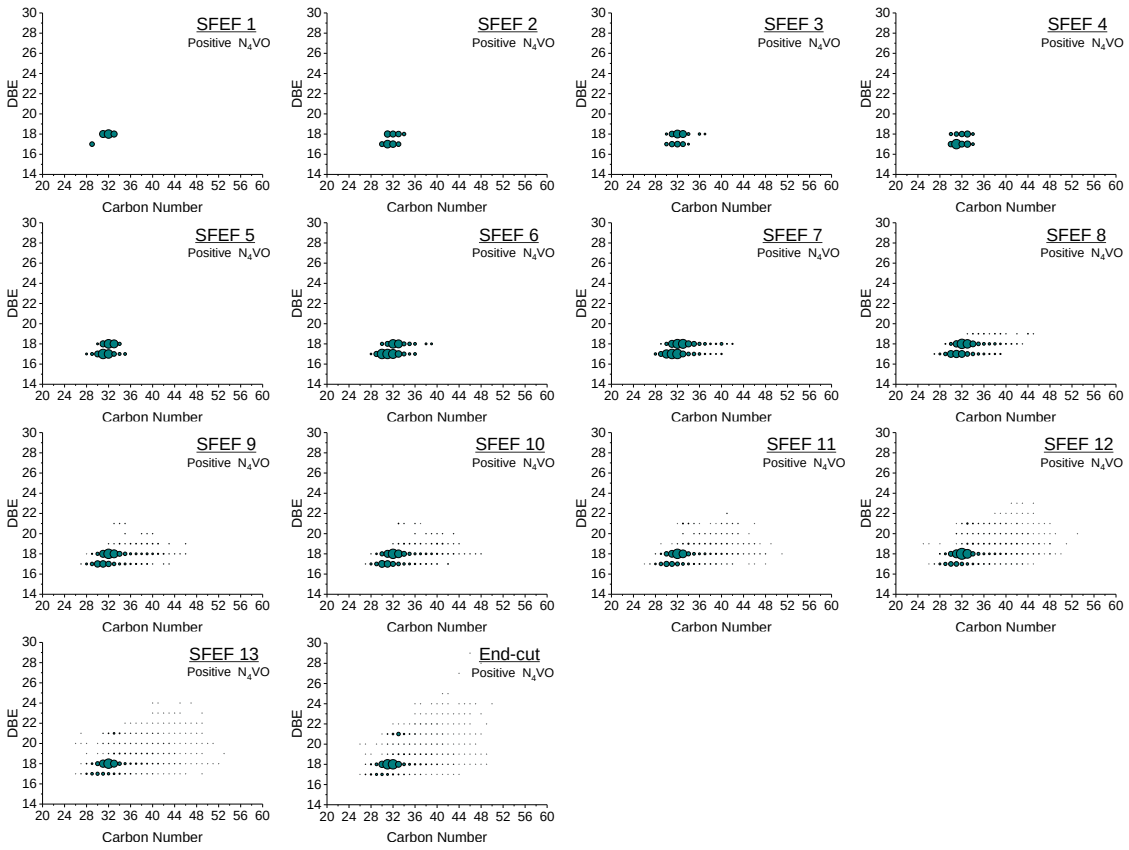

Figure 2.12 Relative ion abundance plots of DBE as a function of carbon number for N_4VO compounds in various SFEF fractions

Canadian oilsands bitumen contains a high concentration of vanadium which is difficult to process in refining operations. All six-petroleum derived vanadyl porphyrins, such as ETIO, DPEP, di-DPEP, rhodo-ETIO, rhodo-DPEP, and rhodo-di-DPEP, were detected in SFEF fractions by the accurate mass values identified by positive-ion ESI FT-ICR MS. Figure 2.12 shows the relative ion abundance plots of DBE as a function of carbon number for N_4VO compounds in various SFEF fractions. Only a few dots were observed in SFEF1 indicating very low abundance of vanadyl porphyrins and the number of dots increased as the SFEF fraction became heavier. In SFEF1-7, only two types of vanadyl porphyrins (ETIO with 17 DBEs and DPEP with 18 DBEs) were detected. In the heavy SFEF fractions, all six types of petroleum derived vanadyl porphyrins were detected. The number of carbons in these vanadyl porphyrins varied over a wide range. Most of the

peaks in the end-cut were vanadyl porphyrins indicating a high abundance of vanadyl porphyrins, which is consistent with the results shown in Table 2.1.

2.3.5 Comparison of Canadian oilsands bitumen and Venezuela orinoco extra heavy oil

The properties of Venezuela Orinoco extra heavy oil closely resemble those of Canadian oilsands bitumen; heavy feedstocks with high concentrations of contaminants. Due to their enormous reserves, these two feedstocks have been studied extensively. Zhang *et al.*[190] conducted a similar molecular characterization study using FT-ICR MS on a 500 °C Venezuela VR sample (bulk properties: 1.0524 g/cm^3 density at 20 °C, 4.8 wt% sulfur, 0.98 wt% nitrogen, 176 wppm nickel, and 752 wppm vanadium) and its SFEF narrow fractions. The mass range and maximum peak of the Venezuela SFEF fraction increased as the fraction became heavier, which were different from those of the oilsands bitumen derived VR. This cannot be explained by their compositional differences, since the FT-ICR MS analysis has poor reproducibility in mass distribution. In the Venezuela VR, the relative abundance of multifunctional group classes, such as N_1O_1, N_1O_2, N_1S_1, and N_1S_2 increased gradually as the fraction became heavier. The DBE value and carbon number for pyrrolic compounds in the Venezuela VR derived SFEF fractions showed progressive changes. However, the DBE values for O_2 class species among SFEF fractions showed a slight increase.

In general, the distributions of polar heteroatom species of oilsands bitumen derived VR were similar to those of Venezuela Orinoco extra heavy oil derived VR; the carbon number and DBE gradually increased as the fraction became heavier.

2.4 Conclusions

Molecular composition of polar species in various SFEF fractions of a Canadian oilsands bitumen derived VR was characterized using negative- and positive-ion ESI FT-ICR MS and compared to that of the Venezuela Orinoco extra heavy oil derived VR. The mass ranges of mass spectra and DBE value of polar heteroatom species increased as the SFEF fraction became heavier. The distributions of various class species were shifted as the SFEF fraction became heavier. The single functional compounds were dominant in the light SFEF fractions and the abundant multifunctional group compounds steadily increased as the SFEF fraction became heavier. The abundance of vanadyl porphyrins increased dramatically in heavy fractions, and accounted for 98% in the end-cut. The distributions of polar heteroatom species in the oilsands bitumen derived VR were similar to those in the Venezuela Orinoco extra heavy oil derived VR.

Chapter 3. Porphyrins in marine shales from the Eagle Ford Formation, South Texas

3.1 Introduction

Since the discovery of metalloporphyrins in crude oil and shales by Treibs,[55-56] who postulated that porphyrins were derived from chlorophylls and hemes (hemoglobins) in the living organisms where Mg and Fe functioned as cofactors, porphyrins have been extensively studied. During the burial of dead organisms that escaped oxidation, cofactors in chlorophylls and hemes would have been ion-exchanged with other metal elements, such as nickel and vanadium, in the depositional environments and formed more stable metalloporphyrins as "petroporphyrins". Petroporphyrins contain metal cores that are detrimental to petroleum processing, especially for accelerating catalyst deactivation.[39] Hence, systematic studies on petroporphyrins are of particular importance to the research into petroleum formation and oil refining.

Many analytical techniques including spectroscopy and mass spectrometry have been widely used to analyze petroporphyrins.[57-60] Ultraviolet-visible (UV-vis) spectroscopy is commonly used to identify and quantify petroporphyrins due to its high sensitivity to metalloporphyrins and metal-free porphyrins in electronic absorption of UV-vis radiation.[61] The emergence of mass spectrometry technology in 1960s led to new development in the identification of petroporphyrins. Vanadyl, nickel and iron porphyrins have been found in crude oil and shale present in several types.[62-64] Etio porphyrins (ETIO) and deoxophylloerythroetio porphyrins (DPEP) are two most common types with double-bond equivalences (DBE, i.e., number of rings plus double bonds) of 17 and 18, respectively.[65] Note that the double bond in the vanadyl group (V=O) is not counted in DBE for which only co-valent double bonds connected with carbon atoms are considered. Other types of porphyrins such as dicyclic-deoxophylloerythroetio (di-DPEP), rhodo-etio (rhodo-ETIO), rhodo-deoxophylloerythoetio (rhodo-DPEP), and rhodo-dicyclic-deoxophylloerythroetio (rhodo-di-DPEP) have also been identified in petroleum.[59, 65-67] With the development of ultrahigh resolution mass spectrometry in the last decade, studies on petroporphyrins have made a great progress.[68-70] Fourier-transform ion cyclotron resonance mass spectrometry (FT-ICR MS) offers the highest available broadband mass resolution and accuracy, allowing the assignment of a unique elemental composition to each mass spectral peak measured to analyze complex mixtures.[71-74]

In this study, UV-vis, inductively coupled plasma mass spectrometry (ICP-MS) and gas chromatography-mass spectrometry (GC-MS), positive-ion ESI FT-ICR MS are used to highlight the structural diversity of iron, gallium, vanadyl and nickel porphyrins in immature shales of the late Cretaceous Eagle Ford Formation from South Texas. Late Cretaceous source rocks in the South Texas Eagle Ford Formation were characterized by low maturity organic-rich marls and limestones interbedded with bentonite layers, which clearly recorded Oceanic Anoxic Event 2 (OAE 2). [191-192]

3.2 Experimental section

3.2.1 Samples and reagents

Immature marine shales of the Eagle Ford Formation were collected from Eagle Ford outcrop in Antonio Creek, Terrell County, Texas.[191] The samples were washed with distilled water and rinsed by dichloromethane in order to remove the possible contaminants, and then crushed into 100-200 meshes. The powdered sample was extracted with dichloromethane and methanol (97:3, v: v) in Soxhlet extractors for 72 h. The asphaltenes were collected from the extracts by precipitation in petroleum ether (a boiling point range of 30-60 ℃), followed by filtration. The extracted-asphaltenes fractions were then separated into saturates, aromatics and resins by column chromatography (silica gel : alumina = 4:1), using hexane, benzene and methanol as eluents, respectively.

Analytical reagent grade toluene, methanol, n-hexane, and n-heptane were purified by distillation before use.

3.2.2 GC-MS analyses for saturates and aromatics

The GC-MS analyses of the saturated and aromatic hydrocarbons were performed on an Agilent 5977A mass spectrometer coupled with an Agilent 7890B GC equipped with a DB-1MS capillary column (60 m × 0.32 mm × 0.25 μm). For the saturated hydrocarbons, the oven temperature was maintained at 80 ℃ for 2 min, increased to 220 ℃ at 3 ℃ /min, then to 295 ℃ at 2 ℃ /min, and held at 295 ℃ for 30 min. For the aromatic hydrocarbons, the oven temperature was kept at 60 ℃ for 3 min, then ramped to 295 ℃ at 3 ℃/min, and held at 295 ℃ for 30 min. Helium was used as the carrier gas with a flow rate of 1.0 mL/min. The transfer line temperature was 280 ℃, and the ion source temperature was 230 ℃. The ion source was operated in electron-impact ionization (EI) mode at 70 eV. A full scan mode was used for biomarker identification.

3.2.3 UV-vis spectroscopy analysis

UV-vis spectroscopy (Angilent Cary 60) was used to identify the petroporphyrins of the shale sample. The shale asphaltenes were dissolved in methanol for comparison with a methanol extract of Venezuela Orinoco crude oil. The instrument was equipped with a 1 cm cuvette, and HPLC-grade toluene was used as the solvent. The samples were scanned at 300-700 nm wavelength.

3.2.4 ICP-MS analysis

One milligram of asphaltenes from one sample was weighed and treated by nitrolysis with 6 mL HNO_3, and then dissolved in water, formulated as an aqueous solution. The concentrations of vanadyl, nickel, iron and gallium as ions in the solution were measured by an ICP-MS (Thermo Scientific XSERIES 2). The HNO_3 was HPLC-grade, and the water was deionized (18.3 MΩ•cm).

3.2.5 ESI FT-ICR MS analysis

Ten milligrams of the asphaltenes was mixed with 1 mL of toluene. A 20 µL of the toluene solution was diluted with 1 mL of 1:3 toluene:methanol. The toluene and methanol used were analytical reagent grade that were distilled twice and kept in glass bottles with ground glass stoppers. Glassware was used for solvent handling and transfer, except the steel pistons for 10 µL Hamilton syringes.

The asphaltene sample was analyzed using a Bruker Apex-Ultra FT-ICR MS equipped with a 9.4 T superconducting magnet. The sample solution was infused into an Apollo II electrospray ionization source at 180 µL/h using a syringe pump. $HCOONH_4$ was added into the solution as ionization promoter to enhance the response of low-polar compounds in positive-ion ESI.

The conditions for positive ion operation were -4.5 kV spray shield voltage, -5.0 kV capillary column front end voltage, and 310 V capillary column end voltage. Ions accumulated for 0.001 s in a hexapole with 2.0 V DC voltage and 500 Vpp RF amplitude. Optimized mass for Q1 was 300 Da. Hexapoles of the Qh-Interface were operated at 5 MHz and 800 Vp-p RF amplitude, in which ions accumulated for 1.2 s. The delay was set to 1.3 ms to transfer the ions to an ICR cell by electrostatic focusing of transfer optics. ICR was operated at 13.84 dB attenuation, 193-1000 Da mass range. The FT-ICR data were acquired in 4M with a transient time about 2.936 s, resulting in a resolving power of roughly 450,000 at *m/z* 500. Time domain data sets were coadded from 128 acquisitions. $HCOONH_4$ was used as ionization promoter to enhance the response of low-polar compounds in positive-ion ESI.

3.3 Results and discussion

3.3.1 Iron porphyrins and atypical iron porphyrins

Table 3.1 shows bulk characters by Rock-Eval pyrolysis and the concentrations of vanadium, nickel, iron and gallium elements in the asphaltenes measured by ICP-MS. All samples have high TOC content and low maturity (T_{max} < 430 °C). the equivalent vitrinite reflectance using Rock-Eval T^{max} values is about 0.4 – 0.5 $\%R_c$[33]. Hydrogen index and oxygen index from Rock-Eval pyrolysis suggest a type II kerogen organic matter[33]. The measured sample contains high concentrations of iron, vanadium and nickel at 634.2, 270.1, and 257.7 ppm, respectively. There is also a considerable amount of gallium with a value of 29.3 ppm.

Table 3.1 Bulk characters by Rock_Eval pyrolysis and concentrations of vanadium, nickel, iron and gallium in asphaltenes measured by ICP-MS

			Rock_Eval Pyrolysis							ICP-MS			
Samples	Depth	TOC	S1	S2	S3	Tmax	HI	OI	PI	V	Ni	Fe	Ga
	(m)	(%)	(mg/g)	(mg/g)	(mg/g)	(ºC)	(mg/g.TOC)	(mg/g.TOC)			(wppm)		
No1	outcrop	4.79	2.72	23.16	0.73	430	484	15	0.10	nd	nd	nd	Nd
No2	79.7	2.3	0.3	11.5	0.7	424	492	28	0.03	nd	nd	nd	nd
No3	110	5.1	0.8	33.7	0.8	419	665	15	0.02	270.1	257.7	634.2	29.3

TOC: total organic carbon; S1 and S2 are obtained from Rock-Eval pyrolysis; S1: volatile hydrocarbon; S2: degraded hydrocarbon from kerogen; HI: hydrogen index, S2×100/TOC; OI: oxygen index, S3×100/TOC; PI: production index, S1/[S1 + S2].

Figure 3.1 shows the GC-MS results of the saturates and aromatics fractions of the shale extracts (maltanes), UV-vis and (+) ESI FT-ICR MS. The gas chromatogram of saturated hydrocarbon fraction in Figure 3.1(*a*) exhibits *n*-alkanes in the saturated hydrocarbon fraction ranging from *n*-C_{13} to *n*-C_{35} with abnormally high abundances of isoprenoids (e.g. pristane and phytane) and steranes. The Pr/Ph ratio is 2.1, indicating an oxidizing environment. The distribution of steranes in the *m/z* 217 mass chromatogram (insert) with significant amounts of C_{29} steranes and the presence of C_{30} steranes indicate that marine algae inputs are an important contributor to sedimentary organic matter.[192] The relatively high concentrations of biomarkers and isoprenoids suggest low thermal maturity of the Eagle Ford shale being analyzed. The gas chromatogram of aromatic fraction in Figure 3.1(*b*) contains abundant alkylnaphthalenes, alkybenzothiophenes, alkydibenzothiophenes, alkylphenanthrenes and triaromatic steranes. The highest peak in the aromatic fractions is 5,7,8-tetramethyl-2-methyl-2-(4,8,12-trimethyltridecyl) chroman (*5,7,8-triMe*-MTTC), suggesting a low salinity setting.[193] Figure 3.1(*c*) shows the overlaying UV-vis spectra of the asphaltenes from South Texas shale in methanol with a methanol extract of Venezuela Orinoco crude oil that contains high concentrations of vanadyl porphyrins.[78] The majority of the vanadyl porphyrins are enriched in the methanol extract which exhibit a strong UV-vis absorption band at 410 nm, known as Soret band. The asphaltenes also exhibit a strong Soret band, indicating the presence of plentiful vanadyl porphyrins. Another absorption band at 395 nm indicates that the asphaltenes may contain other types of porphyrins, perhaps nickel porphyrins whose Soret band leis near 392nm. Figure 3.1(*d*) shows the positive-ion ESI FT-ICR broadband mass spectrum of the asphaltenes fraction. The appearance of intense iron porphyrins peaks at *m/z* 480-700 which will be discussed below is in agreement with the UV-vis result.

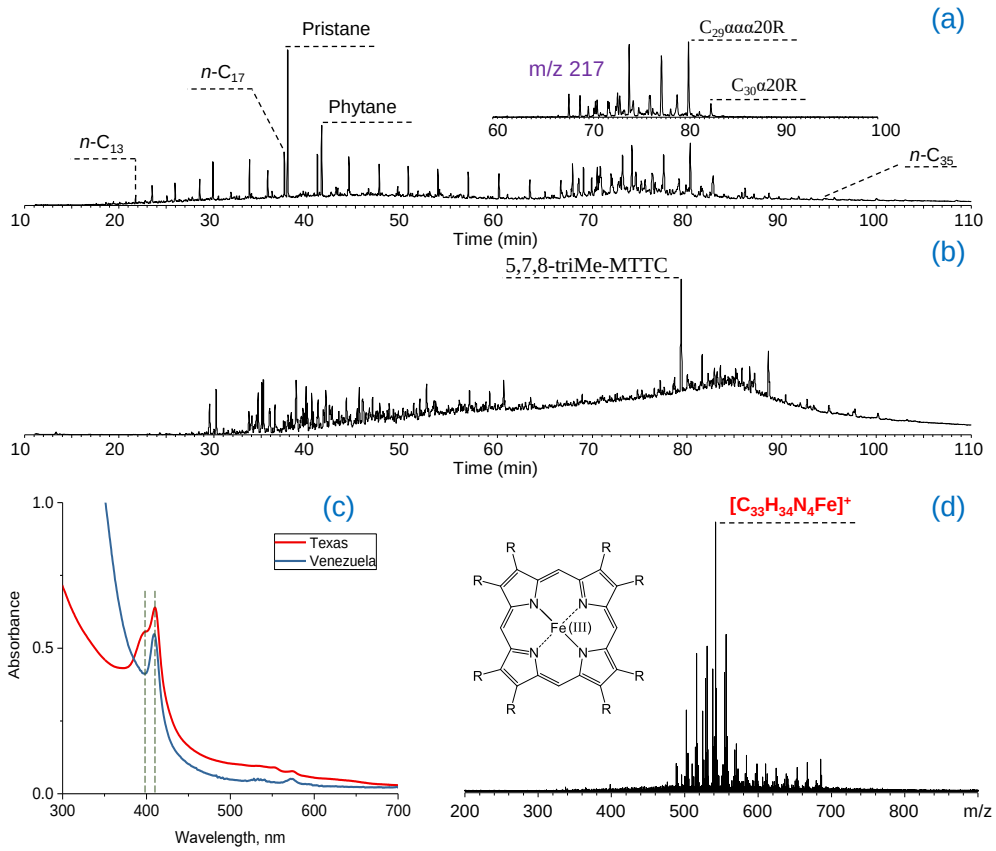

Figure 3.1 Analysis results of South Texas shale extracts : (a) gas chromatogram of the saturates with the *m/z* 217 mass chromatogram inserted, (b) gas chromatogram of the aromatics, (c) UV-vis spectra of the asphaltenes of South Texas shale and the methanol extract of Venezuela crude oil in comparison, and (d) positive-ion ESI FT-ICR broadband mass spectrum of the South Texas asphaltenes. Notes: *5,7,8-triMe-MTTC* stands for *5,7,8-tetramethyl -2-methyl-2-(4,8,12-trimethyltridecyl) chroman*; $C_{29}ααα20R$ stands for (20*R*)-24-ethyl-5*α*(H),14*α*(H),17*α*(H)- cholestane; $C_{30}α20R$ stands for (20*R*)-5*α*(H)-sterane

All three samples show the same pattern of petroporphyrins. Therefore, one sample was used as an example for detailed analysis in order to further investigate the petroporphyin distributions. Figure 3.2 exhibits the expanded *m/z* ranges of 502-506, 526-530 and 606-610 of Figure 1(*d*). All six previously identified petroporphyrin series are found for iron porphyrins, namely, ETIO (DBE = 17), DPEP (DBE = 18), di-DPEP or tetrahydrobenzo DPEP (DBE = 19),[194] rhodo-ETIO (DBE = 20), rhodo-DPEP (DBE =21), and rhodo-di-DPEP (DBE = 22), whose molecular ion peaks and associated isotope peaks can be clearly seen, along with their tentative structures plotted in Figure 3.2.

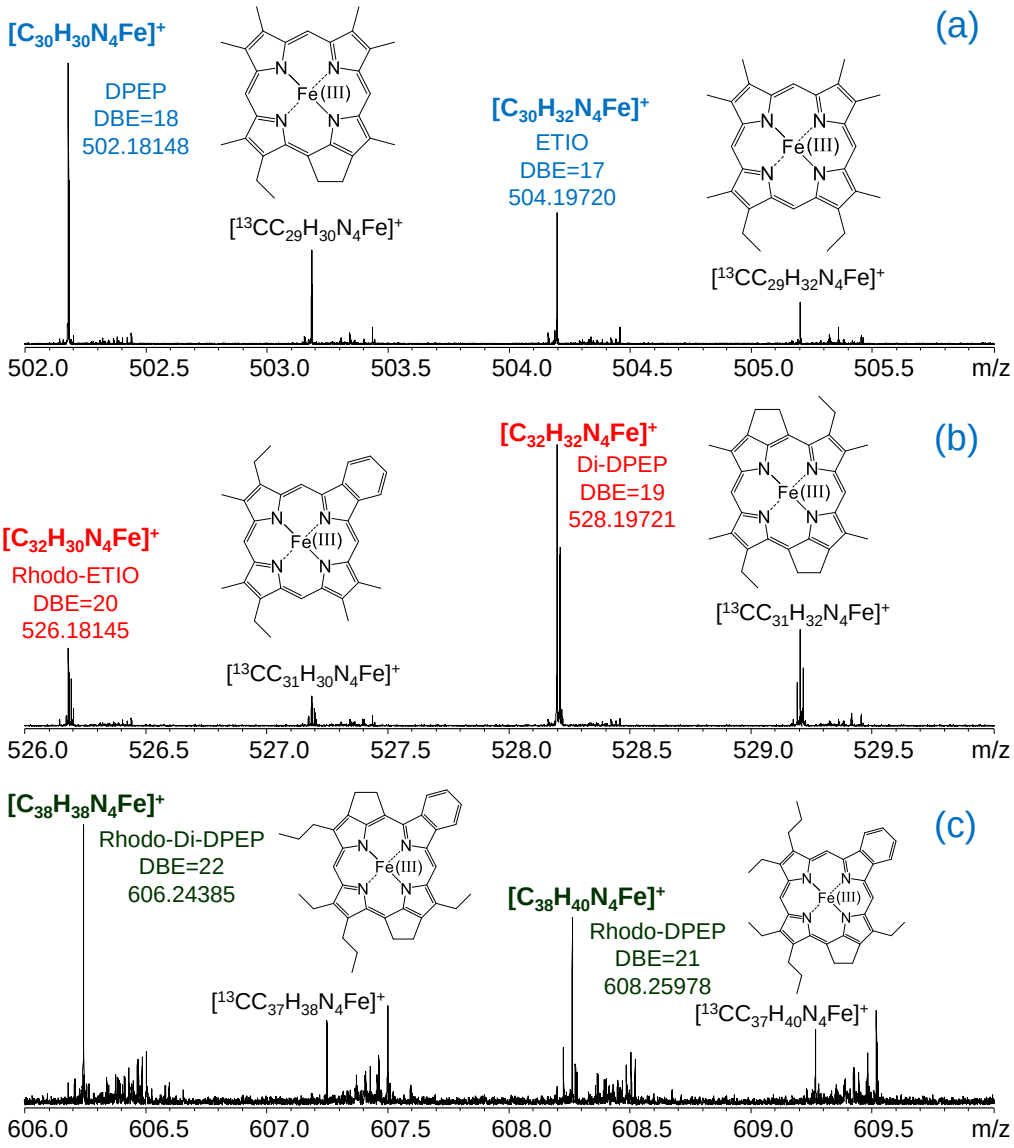

Figure 3.2 Expanded mass spectra of six previously identified iron porphyrin series from the positive-ion ESI FT-ICR MS analysis in the *m/z* ranges of: (a) 502-506, (b) 526-530 and (c) 606-610. Plausible structures shown are based on the molecular composition

To our best known, an entire family of iron porphyrins are identified in a shale for the first time. Iron porphyrins exhibited by strong molecular ions instead of protonated ions in Figure 3.2 suggest that they are fairly polar. Previous studies showed that the iron (II) porphyrin complexes are very unstable in air and rapidly oxidized to ferric porphyrins. Therefore the iron porphyrins here are likely to be iron (III) porphyrins.[195-196] However, the central iron atom would be replaced by nickel and vanadyl during the geological evolution because the stability of nickel and vanadyl porphyrins is higher than that of iron porphyrins.[197] This is why most petroporphyrins detected in more mature shales and crude oils are mainly nickel and vanadyl porphyrins.

Figure 3.3(a) shows the relative ion abundance plot of DBE versus carbon number of the six previously identified iron porphyrin types. High condensation iron porphyrins with DBE values of 23, 24, 25 and 26 are present, with respective carbon number ranges of 34-49, 36-53, 39-48 and 45-48. Figure 3.3(b) and 3.3(c) are the relative ion abundance plots of iron porphyrins containing oxygen with corresponding molecular formulae of $C_nH_mN_4FeO$ and $C_nH_mN_4FeO_2$. The $C_nH_mN_4FeO$ class species may contain a ketone group and exhibit DBE values of 17, 18, 19, 20, 21, 22, 23, 24, 25, 26, and respective carbon number ranges of 29-32, 28-36, 29-44, 31-44, 31-47, 31-50, 35-50, 39-49, 41-51 and 44-46. The $C_nH_mN_4FeO_2$ class species exhibit DBE values of 19, 20, 21, 22, 23 and 24, with postulated ester structure consistent with the ester group in hemoglobin.[198] A new series of iron porphyrins corresponding to $C_nH_mN_5FeO_2$ was also detected. The additional nitrogen atom could be on a functional group, such as amide. Its relative ion abundance plot is shown in Figure 3.3(d). The DBE values of $C_nH_mN_5FeO_2$ class species are 21-27, with 22 most abundant. Figure 3.4 shows the expanded mass spectra at *m/z* 558 and 667. The $C_nH_mN_4FeO$, $C_nH_mN_4FeO_2$ and $C_nH_mN_5FeO_2$ class species yield good responses in ESI FT-ICR MS for an entire family of $C_nH_mN_4FeO$ and $C_nH_mN_4FeO_2$ porphyrins to be identified in petroleumsource rocks for the first time.

Compared with the iron porphyrins found by Schaub et al in hydrothermal liquefaction biocrude oils[81], the distribution range of iron porphyrins in the Eagle Ford shales is wider including abundance of high condensation iron porphyrins. In addition, we also found a large number of oxygen-containing iron porphyrins, which would provide new reference for the evolution of chlorophyll to petroporphyrins.

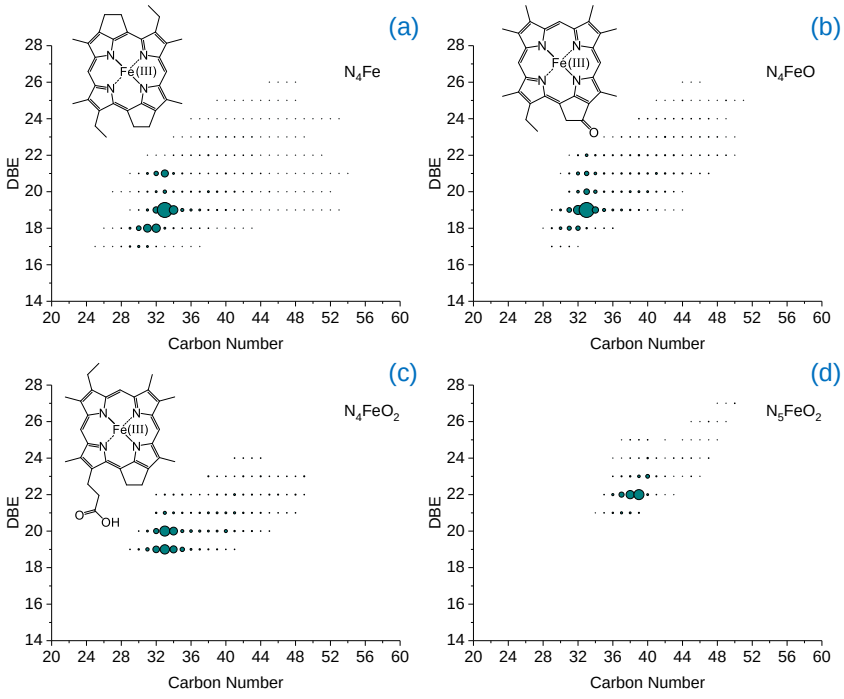

Figure 3.3 Relative ion abundance plots (DBE versus carbon number) of (a) N_4Fe, (b) N_4FeO, (c) N_4FeO_2, and (d) N_5FeO_2, from positive-ion ESI FT-ICR MS analysis

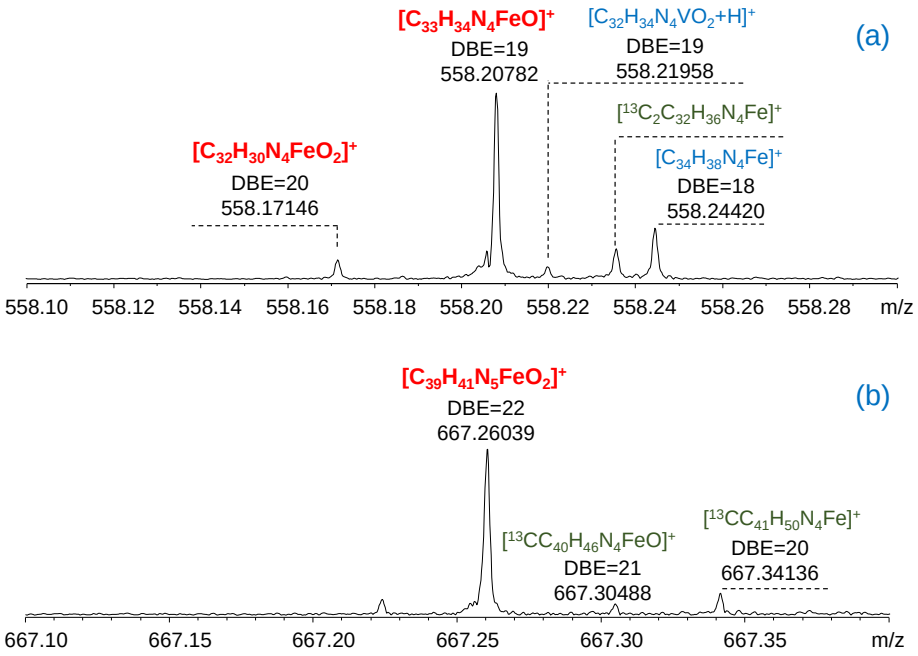

Figure 3.4 Expanded mass spectra of the asphaltenes from the positive-ion ESI FT-ICR MS analysis at *m/z* (a) 558 and (b) 667

3.3.2 Gallium porphyrins detected in the shale

Gallium (III) porphyrins were also found in the asphaltenes of South Texas shale, which have previously been reported in bituminous coal[199-200] but never been identified in other shales and petroleum samples. The metalloportphyrins commonly found in petroleum contain the transition metals of the first row in the periodic table, such as nickel, vanadium and iron. However, gallium is a post-transition metal. Figure 3.5 shows the relative ion abundance plots in DBE versus carbon number of N_4Ga from positive-ion ESI FT-ICR MS analysis. The $C_nH_mN_4Ga$ class species exhibit five types of compounds with DBE values of 17, 18, 19, 20, and 21, and carbon number ranges of 28-32, 28-34, 31-40, 32-39, and 32-34, respectively. The most abundant gallium porphyrins class species are DBE = 18 and 19. Identification of these gallium porphyrins is based on the accurate mass and isotopic ratio of the spectral peaks. Figure 3.6 shows the comparison between the measured and calculated mass spectra, which covers these new gallium compounds and their ^{13}C and ^{71}Ga isotopic peaks. The theoretical isotope distributions were generated by Bruker DataAnalysis software. The mass measurement errors of monoisotopic and isotopic peaks of $[C_{33}H_{34}N_4Ga]^+$ and $[C_{32}H_{34}N_4Ga]^+$ is only 1 mDa except for the small $^{13}C^{71}Ga$ peaks that overlap with larger peaks. The measured and calculated isotope ratios are essentially the same. The found of gallium porphyrins in the very low maturity shale would provide new clue on evolution of chlorophylls and hemes to porphyrins.

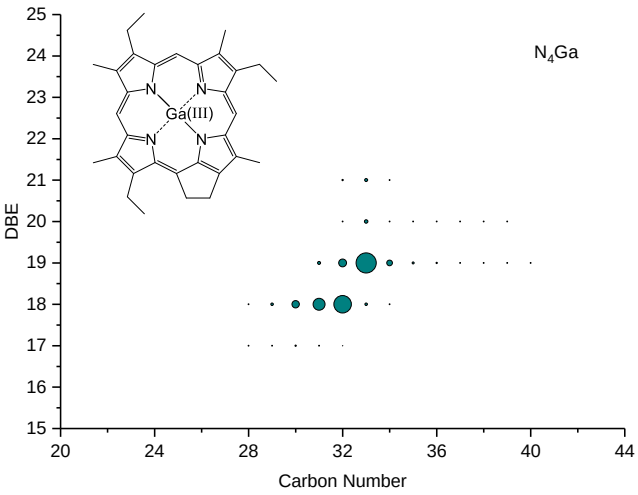

Figure 3.5 Relative ion abundance plots (DBE versus carbon number) of N_4Ga from positive-ion ESI FT-ICR MS

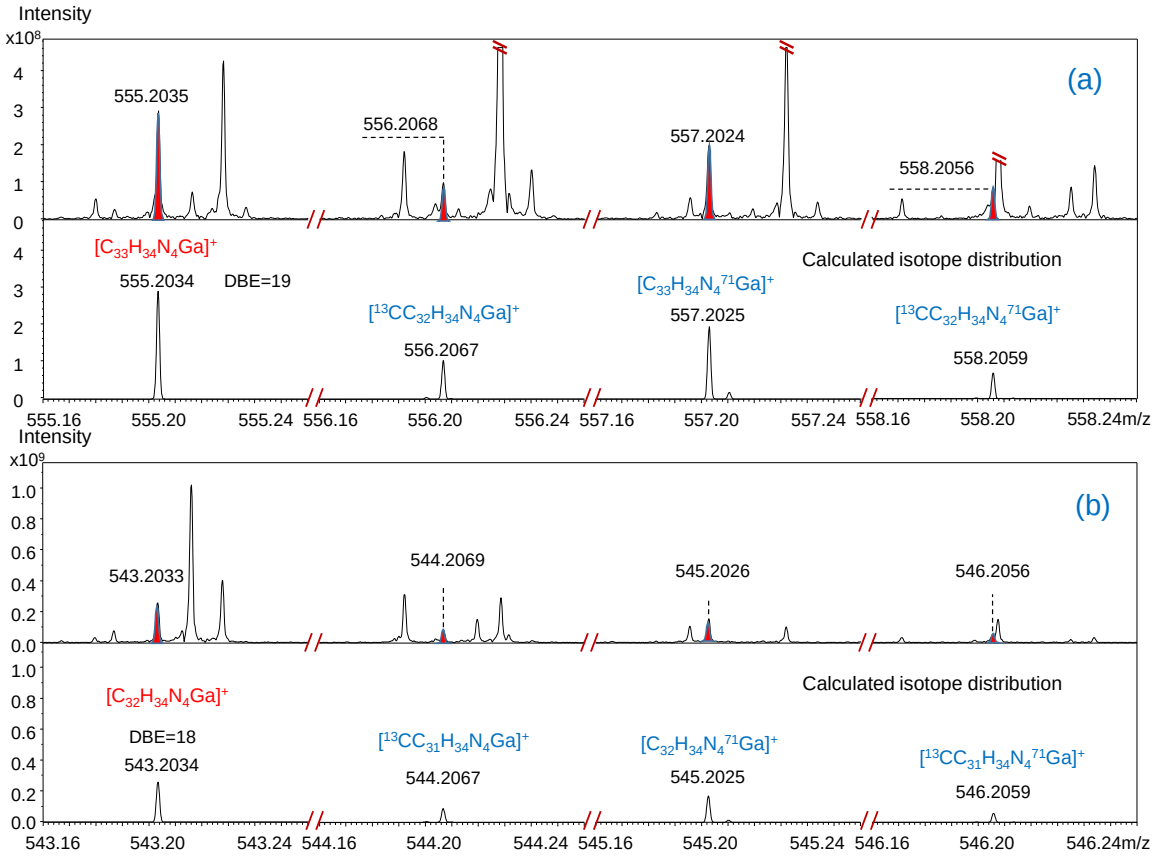

Figure 3.6 Comparison between measured and calculated mass spectra for ions of (a) $[C_{33}H_{34}N_4Ga]^+$ and (b) $[C_{32}H_{34}N_4Ga]^+$

3.3.3 The distributions of metalloporphyrins in asphaltenes of South Texas shale

Gallium, iron, nickel and vanadyl porphyrins were detected in asphaltene of South Texas shale by positive-ion ESI FT-ICR MS, with relative abundances of DBE series with and without $HCOONH_4$ as an ionization promoter[201] shown in Figure 3.7. Some low-polarity compounds in petroleum, such as $C_nH_mN_4VO_3$, $C_nH_mN_4Ni$ and $C_nH_mN_4NiO$ species, cannot be well-ionized in ESI but yield strong response with $HCOONH_4$ as an ionization promoter. The most abundant metalloporphyrins in the shale are iron porphyrins, followed by vanadyl and nickel porphyrins.

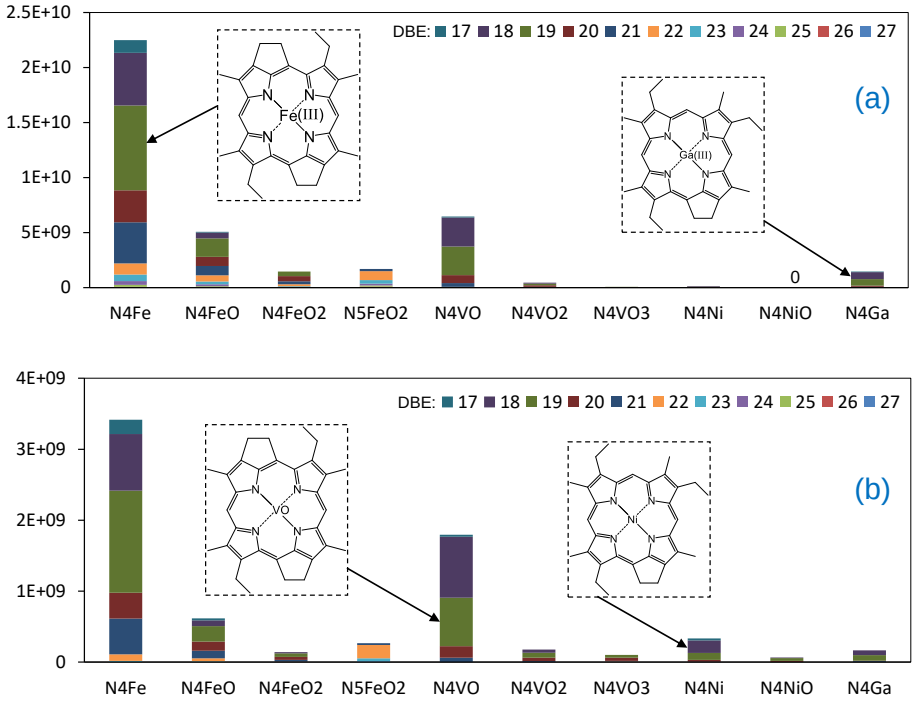

Figure 3.7 Relative abundances of metalloporphyrins in the asphaltenes detected by positive-ion ESI (a) without and (b) with $HCOONH_4$ as ionization promoter

Figure 3.8 is the relative ion abundance plots in DBE versus carbon number of the metalloporphyrins in asphaltenes obtained from positive-ion ESI FT-ICR MS. Six previously identified vanadyl porphyrin types are present, including species of high degrees of condensation (i.e., high DBE values). The DPEP ($C_nH_{2n-30}N_4VO$) of DBE=18 and di-DPEP ($C_nH_{2n-32}N_4VO$) of DBE = 19 are the most abundant vanadyl porphyrins, indicating low thermal maturity. There are four types of $C_nH_mN_4VO_2$ class species, with DBE values of 18, 19, 20 and 21. The $C_nH_mN_4VO_3$ class species are also present. Their peak intensities were greatly improved by the $HCOONH_4$ ionization promoter. Five types of nickel porphyrins, namely, ETIO, DPEP, di-DPEP, rhodo-ETIO and rhodo-DPEP, were found with $HCOONH_4$ as an ionization promoter. In addition, three types of $C_nH_mN_4NiO$ class species containing oxygen with DBE values of 18, 19 and 20 are also present,

with $C_nH_{2n-32}N_4NiO$ with DBE of 19 most abundant. The additional oxygen atoms in the nickel and vanadyl porphyrins are believed to be attributed to oxygen functional groups, as oxygen-containing iron porphyrins.

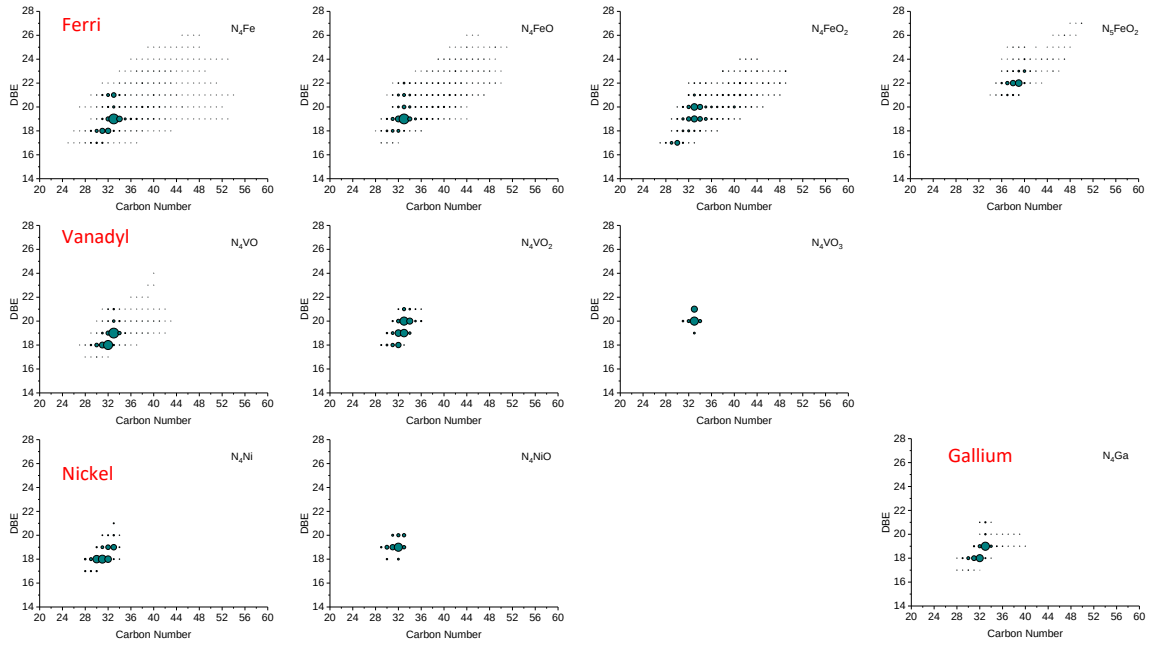

Figure 3.8 Relative abundance plots (DBE versus carbon number) for metalloporphyrins in the asphaltenes from positive-ion ESI FT-ICR MS. The data for $C_nH_mN_4Ni$ and $C_nH_mN_4NiO$ class species was from the spectra with $HCOONH_4$ as ionization promoter

3.4 Conclusions

Detailed characterization of metalloporphyrins was performed on the Late Cretaceous Eagle Ford shale, South Texas by positive-ion ESI FT-ICR MS. Iron, gallium, vanadyl and nickel porphyrins were detected simultaneously. All six types of iron porphyrins previously identified were found, including the species of high degrees of condensation. Three new types of oxygen-containing iron porphyrins corresponding to $C_nH_mN_4FeO$, $C_nH_mN_4FeO_2$ and $C_nH_mN_5FeO_2$ were also identified. For nickel and vanadyl porphyrins, the species containing additional oxygen atoms, i.e., $C_nH_mN_4NiO$, $C_nH_mN_4VO_2$ and $C_nH_mN_4VO_3$, were also present. These oxygen-containing metalloporphyrins are believed to be attributed to oxygen functional groups. Gallium porphyrins were identified in petroleum samples for the first time. The finding of gallium porphyrins and oxygen-containing porphyrins could provide new insights on the diagenetic pathway and the evolution of petroporphyrins, which may have important implications to decipher the development of Oceanic Anoxic Event 2.

Chapter 4. Molecular composition of vanadyl porphyrins in the gilsonite

4.1 Introduction

The gilsonite is a kind of stable natural asphalt which derives from petroleum through hundreds of millions of years and deposition with the effects of pyrolysis, oxidation, catalytic and biological degradation. It generally exists in the rock cracks and distributed in veins. The gilsonite has been found in many parts of the world, such as Utah in the United States, Bouton Island in southeastern Indonesia, Ragusa in Italy, Gard in France, Neuchatel in Switzerland, Karamay and Qingchuan in China.[202-206] The gilsonite can be used as road asphalt modifier, which can greatly improve the weather and ultraviolet aging resistance of the petroleum asphalt, and thereby extend the service life of the road. The reserve of gilsonite in Qingchuan County (Sichuan Province, China) is preliminary proved of over 1.4 million tons and of over 30 million tons is prospected. Considering the huge reserves, gilsonite in Qingchuan, as well in other places should has important value for commercial utilization.

The gilsonite has a carbon content greater than 80 wt% with a low H/C ratio. It contains a large amount of N, O, and S elements, which are existed in the formation of polar functional groups. In addition, the gilsonite also contains many metal elements, such as V, Ni, Fe, etc. It is well known that quite amount of metal in petroleum is existing in the form of metalloporphyrin, which are considered coming from chlorophyll and heme by demetallation, saponification, decarburization, reduction, aromatization, decarboxylation, and metal chelation in the long-term geological evolution.[55-56] Since the 1960s, significant progress has been made on the molecular composition and formation mechanism of petroleum porphyrins.[207-209] As a geological biomarker, porphyrins have been used in petroleum exploration to determine the source rock type, maturity, hydrocarbon generation threshold, and hydrocarbon expulsion migration. It also provided important information for the studies of oil-source rock comparison, oil and gas reservoir types, and oil/gas reservoir distribution.[210-211] The relative abundance of etio porphyrins (ETIO) and deoxophylloerythroetio porphyrins (DPEP) and the ratio of nickel porphyrins and vanadyl porphyrins were both used as important parameters for the investigation of oil source and its maturity.[207-208] It was found that DPEP porphyrins are preponderant and leading to a low ETIO/DPEP ratio in oils with low maturity,[212] while ETIO porphyrins become the main type with the thermal maturation. The composition of porphyrins was also used as an indicator for oil source comparison.

The presence of metal compounds in crude oil brings a lot of negative effects to the petroleum refining. Crude oils with high metal content often cause fouling in the furnace tubes and catalyst deactivation in the processing. The nickel and vanadium elements mainly exist in the form of porphyrin in heavy crude oil, which are quite stable and not easy to be removed. These elements could deposit on the catalyst surface and cause catalyst poisoning even directly deactivated. Specifically, the nickel mainly reduces the selectivity of

the catalyst; while the vanadium mainly affects the activity. Therefore, the existence form of these metal compounds in petroleum not only has geochemical significance, but also important for the research in petroleum refining.

In summary, the study of porphyrin has been paid much attention by petroleum chemists for a long time.[16, 213] The gilsonite, as a special state of heavy petroleum, should be rich in porphyrin compounds. But so far there is no research report about petroporphyrins in gilsonite. In this study, the bulk properties and molecular composition of Qingchuan gilsonite will be characterized by various techniques.

4.2 Experimental section

4.2.1 Materials and reagents

The gilsonite was taken from Guangyuan in Sichuan Province. After grinding and crushing, the gilsonite particles less 100 mesh were sieved, and then extracted with toluene to remove mineral impurities. A heavy crude oil was taken from Tahe oilfield. Analytical reagent grade toluene, methanol, n-hexane, and n-heptane were purified by distillation before use.

4.2.2 Instruments

Bruker Apex-Ultra Fourier transform ion cyclotron resonance mass spectrometry (FT-ICR MS) equipped with a 9.4 T superconducting magnet (Bruker Daltonic Inc.); electrospray ionization (ESI); gas chromatograph-mass spectrometer (GC-MS: TSQ 8000 Evo/Trace 1310, Thermo Scientific Inc.); Ultraviolet-visible spectroscopy (UV-vis: Angilent Cary 60); high-temperature gas chromatography-atomic emission detector (HT-GC: Agilent 7890, AED: JAS 2390AA); Inductively Coupled Plasma Optical Emission Spectrometer (ICP-OES); elemental analyzer (Elementar Analysensysteme GmbH).

4.2.3 SARA separation

The SARA separation of toluene-soluble gilsonite was conducted in accordance with the petrochemical industry standard SH/T 0509-92. The asphaltene fraction was precipitated by heptane, and the maltene was divided into saturates, aromatics, and resins by a Al_2O_3 column with the elution of hexane, toluene, and toluene/ethanol, respectively.

4.3 Results and discussion

4.3.1 Analysis of gilsonite and its fractions

Table 4.1 shows the element composition of the gilsonite. The element contents of C and H were 81.82 wt% and 7.81 wt%, respectively. The H/C ratio, 1.14, was lower than that of conventional petroleum asphaltenes, which indicates a high degree of molecular condensation. The contents of oxygen, nitrogen and sulfur

elements in the gilsonite were 2.72 wt%, 2.27 wt% and 4.06 wt% respectively. Heteroatoms could provide a large number of polar groups, resulting in strong polarity of the gilsonite. The gilsonite was also rich in metal elements, among which the content of V was the highest, presenting a value of 3888 $\mu g \cdot g^{-1}$. The contents of Ni, Fe and Ti were 366, 491 and 133$\mu g \cdot g^{-1}$, respectively. The Ni and V elements in petroleum are generally in the form of metal porphyrins. However, there are still many metal compounds whose forms have not been confirmed as well those in gilsonite.

Table 4.1 Elements contents of the Qingchuan gilsonite

Element	C	H	O	N	S	H/C	V	Ni	Fe	Ti
	w/%						*w*($\mu g \cdot g^{-1}$)			
Content	81.82	7.81	2.72	2.27	4.06	1.14	3888	366	491	133

SARA composition of the gilsonite was listed in Table 4.2. The yield of saturate fraction was very low, only 0.82 wt%; the yield of aromatics and resins were 6.43 wt% and 9.35 wt%, respectively. The abundance of light components in the natural gilsonite was very low, since it has been suffering a long-term geological evolution and biological degradation. The content of asphaltene fraction was as high as 81.5 wt%, implying that the gilsonite is high polarity and high-condensed.

Element analysis of SARA fractions showed that most of the V element was present in the asphaltene fraction, accounting for 95.5% of the total. The V element concentration in the resin fraction was1895 $\mu g \cdot g^{-1}$. The gilsonite and its fractions with high content of V element will be idea objects to investigate the morphology of metal compounds in asphaltenes.

Table 4.2 SARA composition and vanadium content in these fractions

	Yield *w*/%	V /($\mu g \cdot g^{-1}$)	V /%
Saturates	0.82		
Aromatics	6.43		
Resins	9.35	1895	4.48
Asphaltenes	81.5	4642	95.5
Sum	98.1		100

GC-MS analysis was performed to investigate the molecular composition of saturate and aromatic fractions of the gilsonite. Figure 4.1 shows the GC-MS chromatograms of the saturates and aromatics, as well as mass chromatograms of *m/z* 217 and *m/z* 191 of the saturates. As expected, most hydrocarbon less than C_{20} were absent in the sample. High relative abundance in normal alkanes implies that the oil in the gilsonite was not suffering from severe biodegradation although it was buried very shallow. Steranes and hopanes were

abundant in the saturate fraction. It is worth noting that the gilsonite contains high abundance of diginane and methyldiginane, which represents iron-deficient and sulfur-excess sedimentary environment. The chromatogram of the aromatic fraction looks like a baseline of the blank run, indicating that the compounds in the aromatics are non-volatile and cannot be eluted through the GC column.

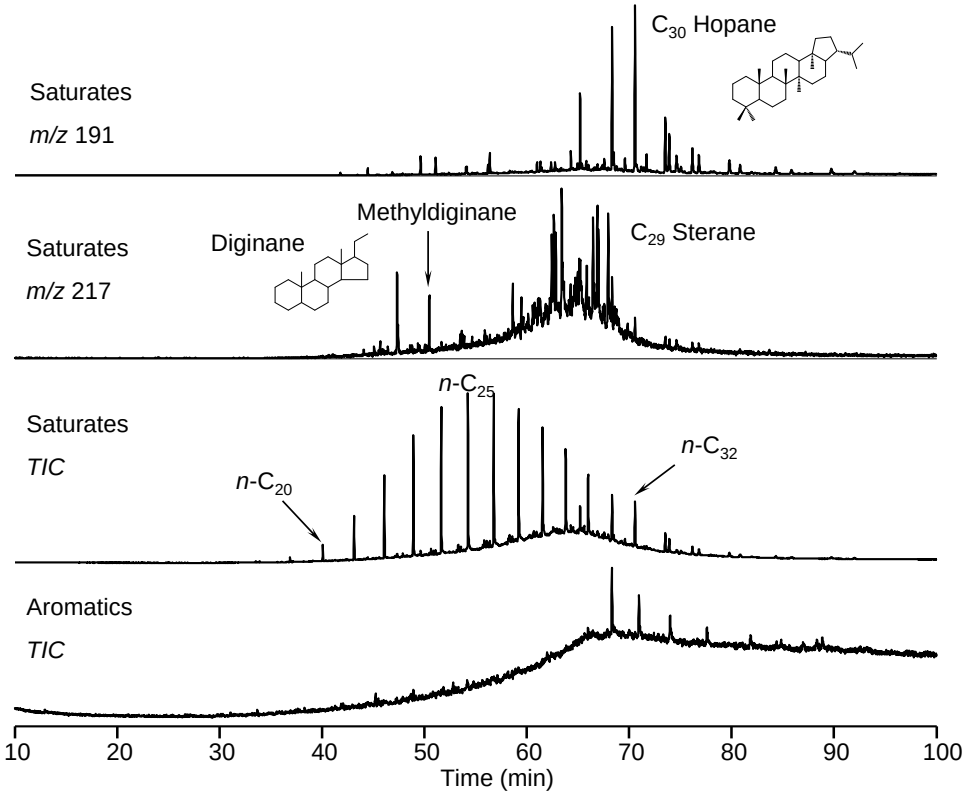

Figure 4.1 Total ion GC-MS chromatograms of the saturates and aromatics, and mass chromatogram of *m/z* 217 and *m/z* 191 for the saturates

4.3.2 Vanadyl porphyrins in the gilsonite

Elemental analysis results showed that the resin and asphaltene fractions contain a large amount of metal V elements. UV-vis analysis, which is one of the most effective methods for detecting porphyrins, was carried out to analyze the metal porphyrins in the gilsonite and its fractions. The UV−vis spectra of the gilsonite and its resins and asphaltenes were shown in Figure 4.2. Strong porphyrin characteristic absorptions were found in the gilsonite, as well the resin and asphaltene fractions. Although the concentration of V element in resins is lower than that of asphaltenes and the raw gilsonite, the UV absorption of the resins was the strongest. This is because less matrix material in the resins affects the absorption coefficient of the metalloporphyrins, while the asphaltene matrix has a greater impact on it.

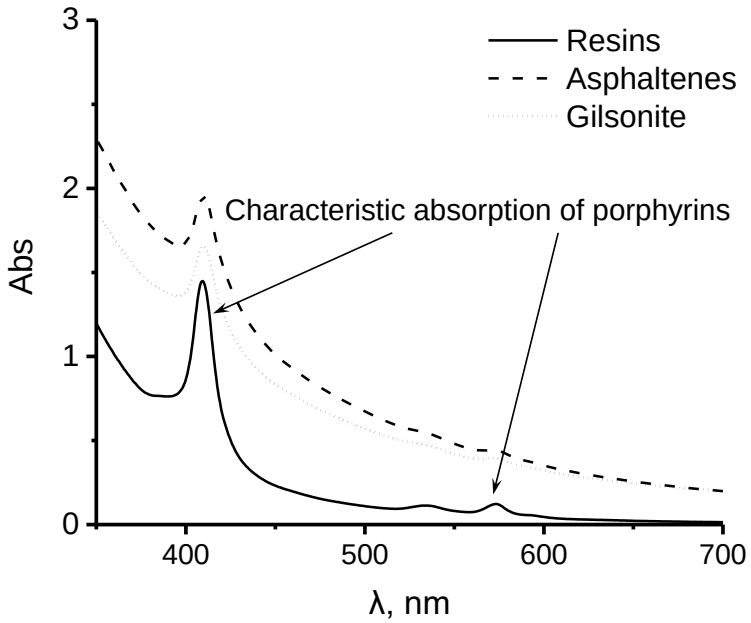

Figure 4.2 UV−vis spectra of the gilsonite and its resins and asphaltenes

Figure 4.3 shows the high-temperature GC-AED chromatograms of the gilsonite and its resins and asphaltenes. The distribution of vanadium compounds in the three samples were similar, in which the resins showed a higher intensity. The results implied that the separation for specific compounds between the resins and asphaltenes was not completed. It also should be noted that the same retention time in the chromatograms does not means the same compound for different fractions. The un-resolved humps of the chromatograms also indicate the composition of the vanadyl porphyrin are very complex. The asphaltene fraction has very high V content, but it showed a low intensity. This can be explained that most V-containing compounds in the asphaltenes are non-volatile and cannot be analyzed by GC even with a high temperature.

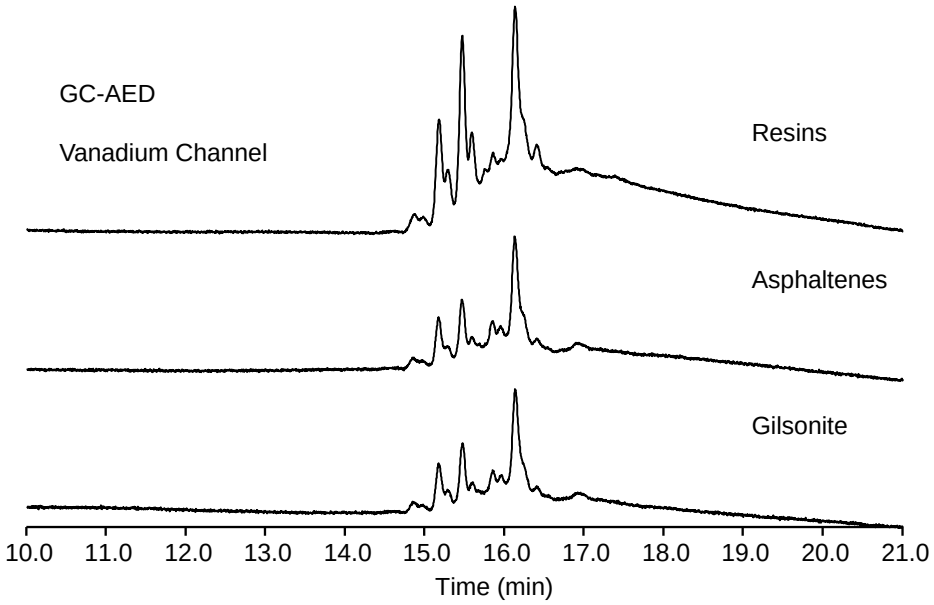

Figure 4.3 High temperature GC-AED chromatograms of the gilsonite and its resins and asphaltenes

High resolution FT-ICR MS has ultra-high resolution power and mass accuracy, which enables the unambiguously assignment on molecular composition. The (+) ESI FT-ICR MS spectra of Tahe heavy oil and Qingchuan gilsonite were shown in Figure 4.4. The V content of the Tahe heavy oil was more than 200 $\mu g \cdot g^{-1}$ which is very high for a crude oil. However, the mass peaks of vanadyl porphyrins did not show preponderance in relative abundance. For the gilsonite, surprisingly, almost all the abundant mass peaks were assigned as vanadyl porphyrins. As shown in Figure 4.4, DPEP vanadyl porphyrins were dominant, showing a normal distribution with a center at C_{31} in carbon number.

The relative ion abundance plots of N_4VO of the gilsonite and the heavy oil were shown in Figure 4.5. The distribution of N_4VO species in the gilsonite was more widespread than that of the heavy oil. N_4VO compounds in Tahe heavy oil were distributed in a DBE range of 17-20 and a carbon number range of 26-37; for the gilsonite the ranges for DBE and carbon number were 17-25 and 25-55, respectively. The most abundant vanadyl porphyrins (N_4VO class) in the heavy oil was ETIO porphyrins which have a DBE value of 17, while that in the gilsonite was DPEP porphyrins which have a DBE value of 18. The ETIO/DPEP values of heavy oil and the gilsonite were 4.16 and 0.52, respectively. Compared with the heavy oil, the maturity of the gilsonite was much lower. This indicates the petroleum in the gilsonite has not been subjected to high temperatures in its long geological history, although it looks remarkably similar to coal.

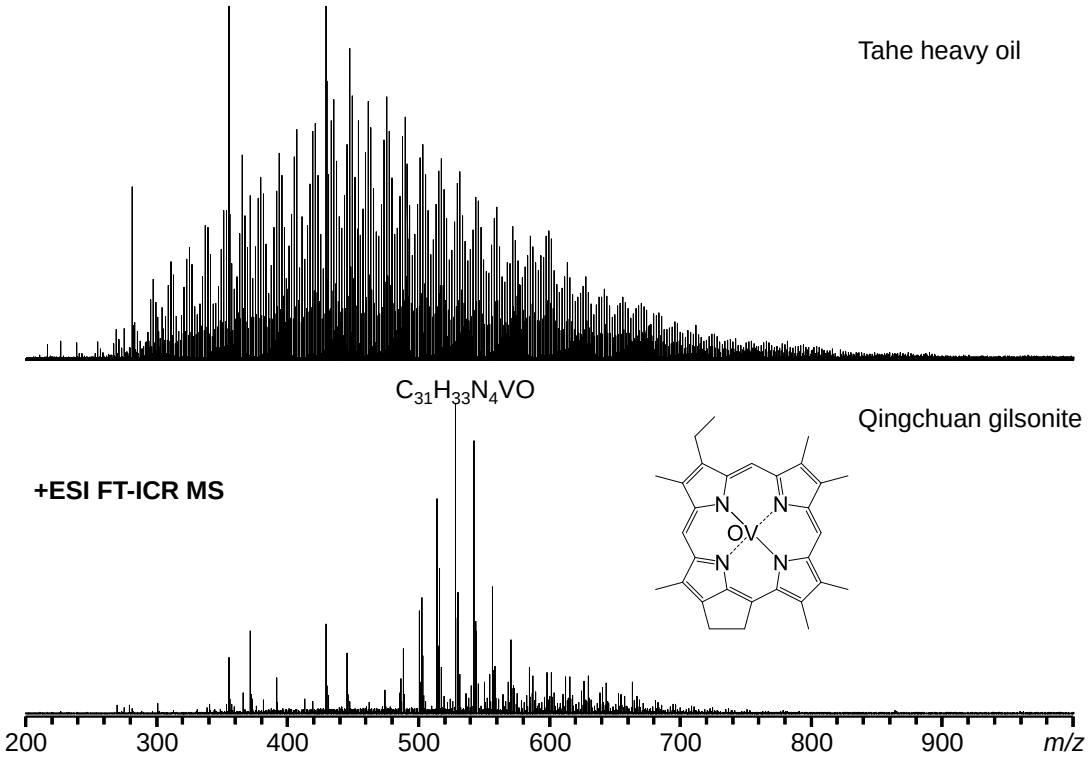

Figure 4.4 Positive-ion ESI FT-ICR mass spectra of the gilsonite and heavy oil

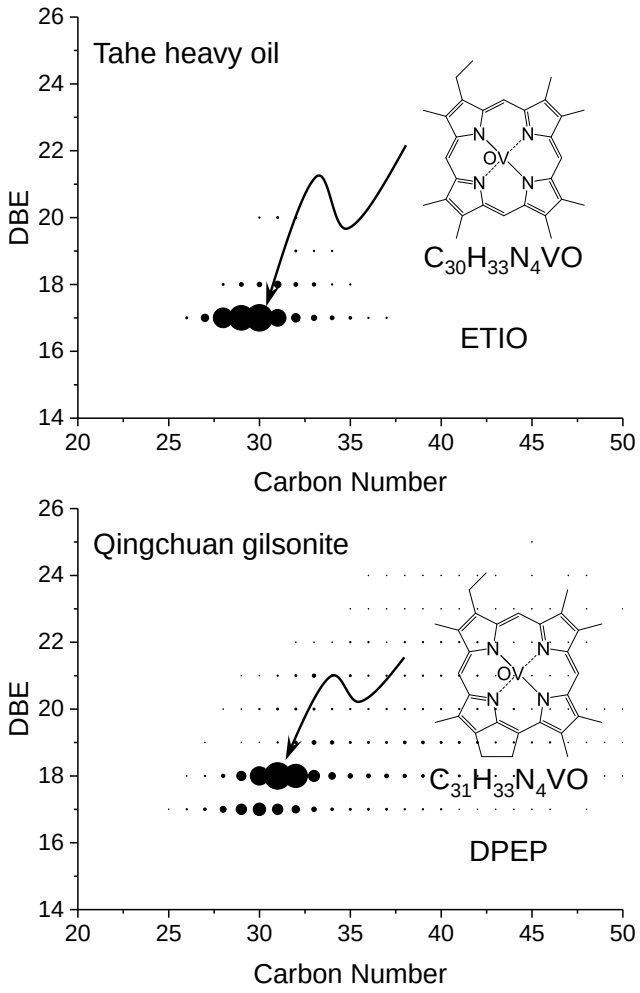

Figure 4.5 Relative ion abundance plots of DBE versus carbon number for N_4VO class species of the gilsonite and heavy oil assigned from the positive-ion ESI FT-ICR mass spectra

4.3.3 Vanadium compounds and the potential utilization of Qingchuan gilsonite

Elemental composition showed that the gilsonite is rich in metal elements, of which the V content was as high as 3888 $\mu g \cdot g^{-1}$. UV-vis analysis indicated that porphyrins exist in the gilsonite and its resin and asphaltene fractions. The chromatogram of HT GC-AED further supported that vanadium compounds in the gilsonite, mainly in the form of porphyrins. ESI FT-ICR MS unambiguously confirmed the molecular composition of these vanadium compounds. Results from various analytical techniques implied that the vanadium compounds in the gilsonite are vanadyl porphyrins. The most abundant vanadyl porphyrins (N_4VO class) in the gilsonite was DPEP type which have a DBE value of 18. Vanadyl porphyrins in Qingchuan gilsonite and Tahe heavy oil have the same distribution center in carbon number (C_{31}), but the distribution range of the former was remarkably wider.

Qingchuan gilsonite has abundant reserves and high metal content, which implies important utilization value. Firstly, the gilsonite can be used as a modifier to improve the performance of road asphalt and extend the service life of the road. Secondly, the gilsonite can be used as energy source. Compared with coal, gilsonite has a higher H/C ratio, corresponding to a greater calorific value. The gilsonite can also be mixed with crude oil to produce light oil products. Thirdly, nickel and vanadium metal are mainly acquired from ores with complicate extraction process and costing much. Qingchuan gilsonite with affluent nickel and vanadium can be utilized as raw material for metal extraction. Specifically, nickel and vanadium can be extracted from the burning residue of the gilsonite. Fourthly, composition and properties of petroporphyrins have always been one of the most important issue for petrochemistry. Qingchuan gilsonite has super-high vanadium and vanadyl porphyrin contents, which is potential to be used as a natural standard material for further studies.

4.4 Conclusions

Qingchuan gilsonite contained a large number of heteroatoms (i.e., N, O and S) and metals, among which the content of V was the highest, presenting a value of 3888 $\mu g \cdot g^{-1}$. The H/C ratio of the gilsonite was as low as 1.14, indicating high degree of molecular condensation. The yield of saturate fraction was only 0.82 wt%, while the content of asphaltene fraction was as high as 81.5 wt%. The V content of the asphaltenes was 4642 $\mu g \cdot g^{-1}$, and the asphaltenes contributed 95.5% of the total V element. Most hydrocarbon less than C_{20} were absent due to the long-term geological evaporation. High abundant vanadyl porphyrins in the gilsonite were determined by UV-vis, HT GC-AED, and ESI FT-ICR MS. The most abundant vanadyl porphyrins (N_4VO class) in the gilsonite was DPEP porphyrin. The molecular composition of vanadyl porphyrins indicated the maturity of the gilsonite is very low. Considering the huge reserves and high metal content, Qingchuan gilsonite should has important utilization value.

Chapter 5. Aggregation of petroporphyrins and fragmentation of porphyrin ion

5.1 Introduction

Composition of asphaltenes has always been one of the most important issue for petrochemistry. During the past decades, many researches have been conducted for the characterization of physicochemical properties of asphaltenes via various analytical methods. Asphaltene molecules are highly condensed and relatively high in undesired heteroatoms and metals, leading to stubborn self-aggregation.[18] Molecular aggregation is a common phenomenon encountered in many chemical and biochemical systems due to strong aggregation interaction between molecules.[144] Aggregation of asphaltene molecules is considered to be an important factor leading to its special properties.[18, 145]

The ultrahigh resolution mass spectrometry, such as Fourier transform ion cyclotron resonance mass spectrometry (FT-ICR MS) has been an indispensable tool for the molecular characterization of asphaltenes,[128-130, 214-217] as well as petroporphyrins.[53-54] Petroporphyrins are considered coming from chlorophyll and heme via demetallation, saponification, decarburization, reduction, aromatization, decarboxylation, and metal chelation in the long-term geological evolution.[55-56] Undoubted fact is that a portion of metals in asphaltenes deposits in the form of petroporphyrins.[53-54] However, the exact molecular form of these metal-containing compounds remains the focus of controversy among researchers in the field.[16]

Ion mobility spectrometry (IMS), a technique that separate ions in the IMS cell according to the size and shape difference of ions, could provide the structural information of the analytes, such as collision cross section (CCS) values and mobility[218-223]. IMS-MS provides another perspective compared with MS-only detection and has been used for petroleum analysis[224-233]. The protonation sites of model porphyrin ions have been investigated by trapped ion mobility spectrometry (TIMS) coupled to FT-ICR MS.[225] Considering the complexity of petroleum, the characteristic signals of petroporphyrins in TIMS should be more fascinating.

Herein, we used trapped TIMS coupled to time of flight mass spectrometry (TOF MS) and FT-ICR MS to investigate the petroporphyrins. The aggregation behavior and fragmentation pathways of porphyrin ions during the transmission were investigated. TIMS-TOF MS provides direct observation of porphyrin cluster ions produced by electrospray ionization (ESI) and dissipated before arriving the mass spectrometer detector. Our results suggest that aggregation of porphyrins with asphaltene molecules is a common form of metal-containing compounds present in asphaltenes. In addition, we may need to re-evaluate the interpretation of mass spectrometry data obtained in recent years on petroporphyrin characterization.

5.2 Materials and methods

5.2.1 Sample pretreatment

Venezuelan Orinoco heavy crude oil was selected to enrich petroporphyrin compounds. The elemental contents of sulfur and nitrogen in the crude oil were 3.90 wt% and 0.74 wt%, respectively. The density at 20 °C was 1.03 g/cm^3. The concentrations of nickel and vanadium were 68.93 and 513.31 μg/g, respectively. The crude oil was subjected to solvent extraction and silica gel chromatography fractionation. Five grams of crude oil was dissolved in 60 mL dichloromethane (DCM), and then 40 g of 200-800 mesh kieselguhr was added to make a slurry mixture by stir. The DCM in the slurry mixture was evaporated in a fume hood at room temperature, with stirring constantly. The solid mixture was placed in a filter paper bucket and extracted with 300 mL methanol (MeOH) for 48 hours, and the methanol solvent was updated once in the middle to prevent the extract from being heated for so long time. The MeOH soluble fraction was obtained after volatilizing the solvent. The MeOH soluble fraction was introduced into a glass column (1 × 80 cm) that filled with 100-200 mesh silica gel (about 50 cm high), and eluted sequentially with solvents of increasing polarity (50 mL each), which were divided into several subfractions. The sample fractionation scheme was shown in Figure 5.1, which was modified from that used by Zhao *et al.*[54]

Ten milligrams of the subfractions after volatilizing the solvent was mixed with 1 mL of toluene. Twenty microliters of the toluene solution were diluted with 1 mL of 1:3 toluene: methanol for the analysis of FT-ICR MS, Orbitrap MS, and TIMS-TOF MS.

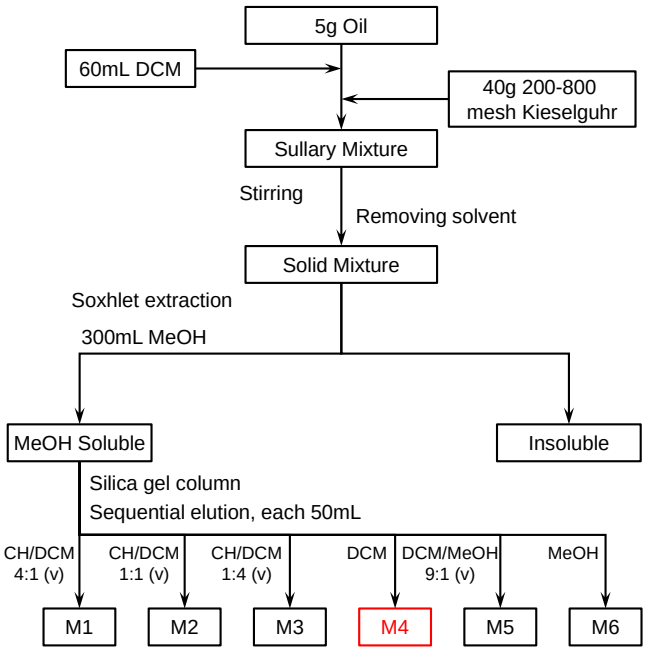

Figure 5.1 Separation scheme of vanadyl porphyrins in Venezuela Orinoco crude oil (CH, cyclohexane; DCM, dichloromethane; and MeOH, methanol)

5.2.2 Chemicals and reagents

Porphine, octaethylporphine, tetraphenylporphine, metal octaethylporphyrins (Me-OEP; Me=Zn, Cu, Ni, and VO) and metal meso-tetraphenylporphyrin (Me-TPP; Me=Zn, Cu, Ni, VO and Fe; Fe-TPP is Iron(III) meso-tetraphenylporphine chloride) were purchased from J&K Scientific. Standard solutions were prepared for Zn-OEP, Zn-TPP, VO-OEP, VO-TPP and Fe-TPP to a concentration of 1 mg/L in toluene/methanol (v:v, 1:3), porphine, octaethylporphine, tetraphenylporphyrin, Cu-OEP, Cu-TPP and Ni-OEP to a concentration of 10 mg/L in toluene/methanol (v:v, 1:3) , and Ni-TPP to a concentration of 100 mg/L in toluene/methanol (v:v, 1:3). The standard solutions were stored in glass vials at 4 °C.

Analytical grade reagents, dichloromethane, cyclohexane, methanol, and toluene were purified by distillation before use.

5.2.3 TIMS-TOF MS analysis

The diagram of the ESI TIMS-TOF MS (Bruker Daltonics, Inc., Billerica, MA) is shown in Scheme 1. The TIMS analyzer is composed of three regions: the entrance funnel, TIMS tunnel, and exit funnel. Unlike the drift tube ion mobility spectrometry (IMS) where the ions are pushed by the electric field through the stationary gas, TIMS uses an electric field to immobilize the ions in moving gas. In addition, with its unique design of ion funnel and analyzer, the TIMS has a high resolution up to about 200.[234] The followed hexapole is used to transport and focus the ions. With an analytical quadrupole and a collision cell, the TIMS-MS achieves the capability to isolate and fragment parent ions prior to mass analysis by the TOF mass spectrometer. The analytical quadrupole is used as a mass filter to isolate ions with certain mass or mass range. For TIMS analysis, the quadrupole region enables collision induced dissociation (CID) with the electron energy added by the terminal electrodes. The ions were transfused into TOF by an orthogonal acceleration stage and detected by the detector. The collision cross section (CCS) of a certain mass ion can be calculated by the equation:

$$\mathrm{CCS} = 18500\frac{z}{K_0}\sqrt{T\frac{Mm}{M+m}}$$

where z is the charge on the ion, K_0 is the reduced mobility as a function of temperature, pressure and electric field, T is temperature, M is the mass of the ions, and m is the mass of collision gas. Detailed instrument construction and theory can be found elsewhere[234].

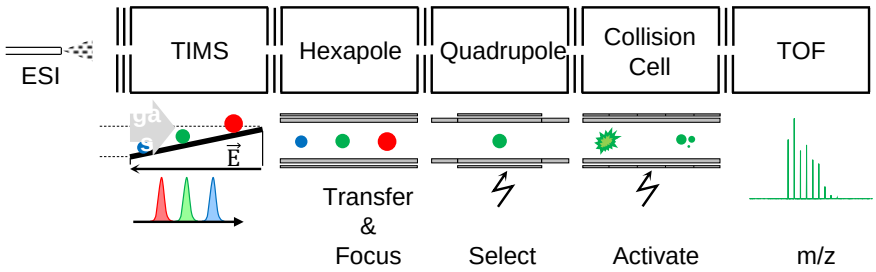

Scheme 5.1 Schematic of ESI TIMS-TOF MS

The sample solutions were injected into the nebulizer at a rate of 180 μL/h using a syringe pump. The positive-ion ESI was run with a 3.2 kV capillary voltage and a 200 ℃ dry temperature. Nitrogen was used as dry gas with a flow rate of 1.5 L/min and the nebulizer pressure was 0.3 Bar. A mass range from 200 to 2000 was selected in order to observe the fragment ions and their aggregation ions of porphyrins. The TIMS was operated with a $1/K_0$ value range of 1.08-2.33 V•s/cm^2. RF amplitudes of the Funnel 1 and Funnel 2 were 150 Vpp and 300 Vpp, respectively. The transfer hexapole was operated at a 40 V deflection delta voltage and a 350 Vpp RF. The quadrupole ion energy was 10 eV and the "low mass" was set to *m/z* 300. A typical collision energy of 10 eV was chosen of the collision cell. Transfer time and pre-pulse storage time were 65 μs and 20 μs, respectively.

TIMS and TOF systems were tuned and calibrated using the electrospray calibration standard (BCBQ6953V; Sigma-Aldrich, AG, Switzerland) in positive-ion mode and the mass error is controlled within 1 ppm. The mass window width of extracted ion mobility (EIM) was (±)0.002 Da. The repeatability of the experimental results was stable, and the deviation of CCS values was less than 1% in the same operating condition.

5.2.4 FT-ICR MS analysis

The porphyrin-rich fraction was analyzed using a Bruker Apex-Ultra FT-ICR MS equipped with a 9.4 T superconducting magnet. The sample solution was infused into an Apollo II electrospray ionization source at 180 μL/h using a syringe pump. The mass spectral peaks were calibrated using an Agilent "Tuning Mix" standard acetonitrile solution with 7 peaks covering a mass range from 118 to 1500 Da. In general, 1 ppm mass accuracy can be achieved with external calibration.

The conditions for positive ion operation were -4.5 kV spray shield voltage, -5.0 kV capillary column front end voltage, and 310 V capillary column end voltage. Ions accumulated for 0.001 s in a hexapole with 2.0 V DC voltage and 500 Vpp RF amplitude. Optimized mass for Q1 was 300 Da. Hexapoles of the Qh-Interface were operated at 5 MHz and 800 Vpp RF amplitude, in which ions accumulated for 1.2 s. The delay was set to 1.3 ms to transfer the ions to an ICR cell by electrostatic focusing of transfer optics. ICR was operated at 13.84 dB attenuation, 200-1000 Da mass range. The Collision Voltages of collision cell were chosen -2.0V,

-4.0V, -8.0V and -10.0V to study the changes in the mass spectrum of petroporphyrins. Detailed instrument calibration and data processing procedures have been described elsewhere.[53]

5.2.5 Orbitrap MS analysis

An Orbitrap Fusion MS (Thermo Scientific) was used to conduct isolation collision experiments to determine the existence form of petroleum porphyrin aggregates. The sample solution was introduced using a syringe pump via an ESI source at a rate of 10 μL/min. The operating conditions were as follows: sheath, auxiliary and purge gas flow rates were 8, 3 and 0.1 arbitrary units, respectively. The temperature of the ion transfer tube and evaporator were 300 and 20 ºC, respectively. The mass range was 200-1000 Da, and a total of 1 minutes of spectrum was scanned. Tandem mass spectrometry (MS/MS) experiments were performed by high-energy collisional dissociation (HCD) with a normalized collision energy of 0-30 eV.

5.3 Results and discussion

5.3.1 Ion mobility spectra of petroporphyrins

Figure 5.2 shows the positive-ion ESI TIMS-TOF MS spectra of vanadyl porphyrin fraction. The abundant mass peaks were vanadyl porphyrins. Intense peaks appeared at the range of *m/z* 500-600 were identified as vanadyl porphyrins and their isotopic. The deoxophylloerythroetio porphyrins (DPEP) which have a DBE value of 18, were the most abundant vanadyl porphyrins.

The ion mobility spectra of DPEP type vanadyl porphyrins were extracted and shown in Figure 5.3 a). Obviously, their extracted ion mobilities (EIM) have two series of peaks with different CCS values, series 1 and series 2. The peak widths of both series are larger than that of individual porphyrin model compounds. Different side chain substitutions of petroporphyrins may be responsible for the large range of mobility. The peaks in series 2 are wider than that in series 1, which may be due to the aggregation involving porphyrin ions.

The CCS value of each mobility peak was calculated and had a good fit with *m/z*. It should be stated here that the CCS values were the highest point values of the smoothed mobility diagrams. As shown in Figure 5.3 b), the R^2 values of the fitting curves of Series 1 and Series 2 are 0.9972 and 0.9983, respectively. The ion mobility spectra and fitting curves of ETIO type vanadyl porphyrins were shown in Figure 5.4. They also have two series peaks with good fit on CCS value and *m/z*.

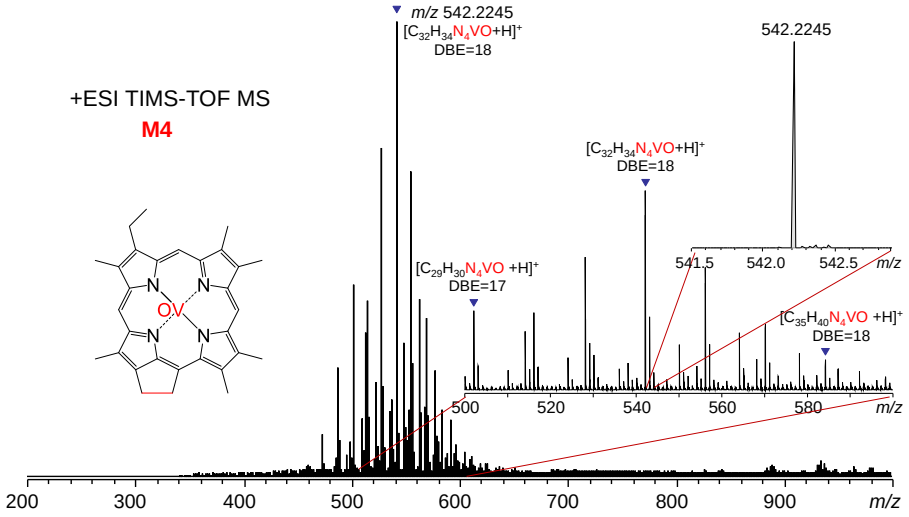

Figure 5.2 Broadband and expanded mass spectra of vanadyl porphyrin fraction from the positive-ion ESI TIMS-TOF MS

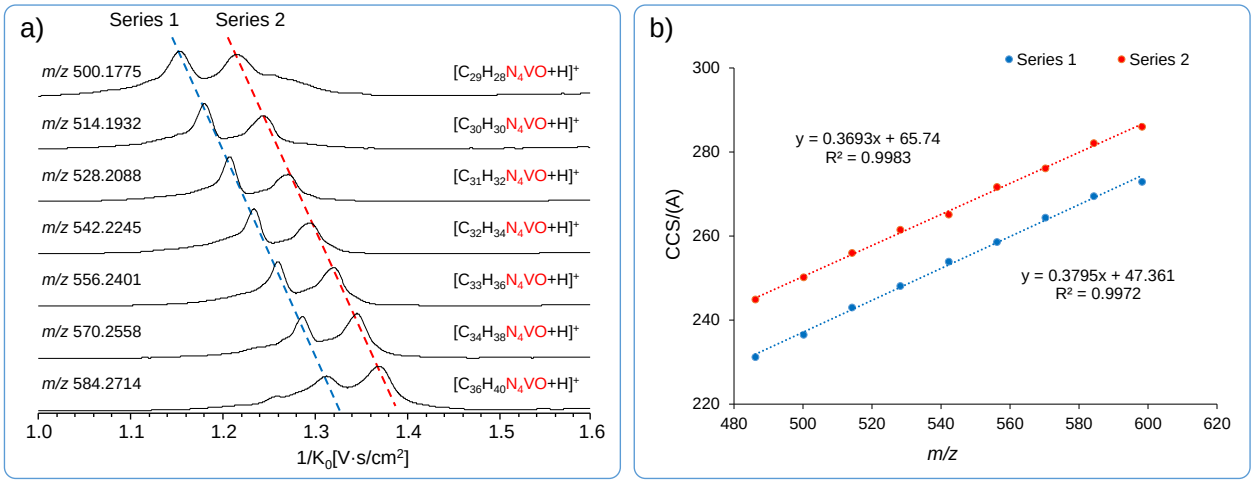

Figure 5.3 Extracted ion mobility (EIM) spectra of DPEP type vanadyl porphyrins analyzed by TIMS-TOF MS (a), and fitting curves for m/z and CCS value of the two series peaks of vanadyl porphyrins (b)

It was abnormal that two diverse mobility peaks appeared on the EIM spectrum of a certain ion. Series 2 is presumed to be the mobility peaks of the aggregated ions of the porphyrin ions with other small molecular compounds in petroleum. To verify this inference, we tried to find the mass peaks of the aggregated ions in the mass spectrum, but failed. This may be because these ions were disaggregated during the transport process due to the occurrence of gas in the TIMS-TOF MS. Hence, FT-ICR MS was utilized to find these aggregated ions, which has a higher vacuum and allows better observation on ions that are easily disaggregated.

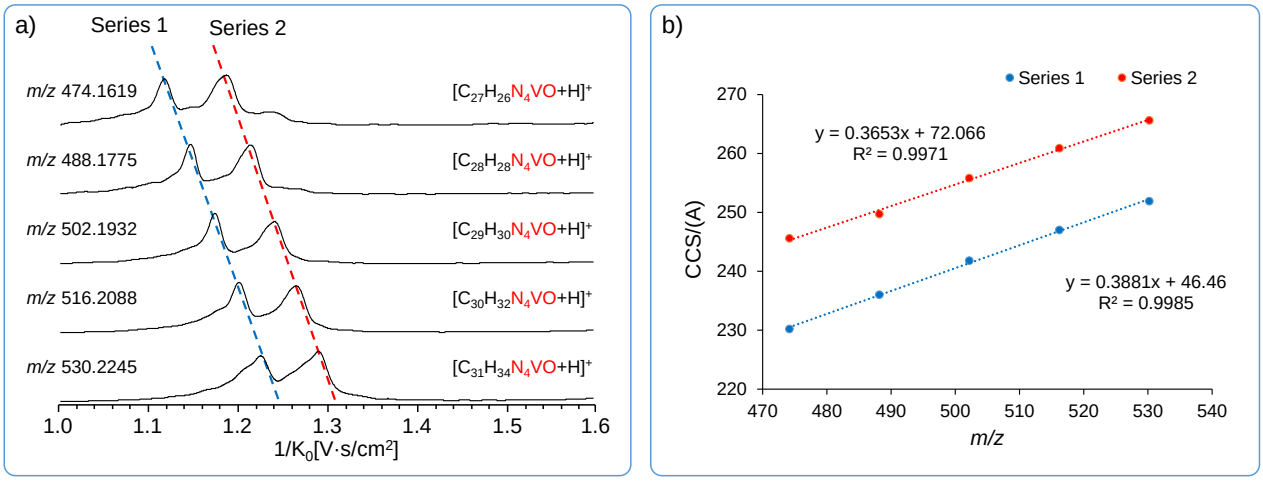

Figure 5.4 a) Extracted ion mobility (EIM) spectra of ETIO type vanadyl porphyrins analyzed by TIMS-TOF MS and b) Fitting curves for *m/z* and CCS value of the two series peaks of vanadyl porphyrins

There is parameter at collision cell of FT-ICR MS named Collision Voltages, which can be adjusted to achieve a CID test on the full mass range. If combined with the isolation function of the previous quadrupole, isolation collision experiments can also be carried out. The CID experiment of vanadyl porphyrin fraction were performed on full mass range with (+) ESI FT-ICR MS. As shown in Figure 5.5 a), when the Collision Voltages was -2.0 eV, the most abundant peaks were N_5VO species, marked with red dots. The abundance of the N_4VO species were much lower, marked with blue inverted triangle. When Collision Voltages increased to -4.0 eV, the abundances of N_4VO and N_5VO species were comparable and the spectrum showed a clear bimodal distribution. As Collision Voltages continue to increase, the abundance of the N_5VO species decreased sharply, and basically disappears at -10eV. These results indicated that N_5VO compounds would crack to N_4VO compounds with very low dissociation energy. Generally, the breaking of the C-C bond requires a dissociation energy greater than 10 eV, so the N_5VO compounds here should be the aggregated ions involving porphyrins.

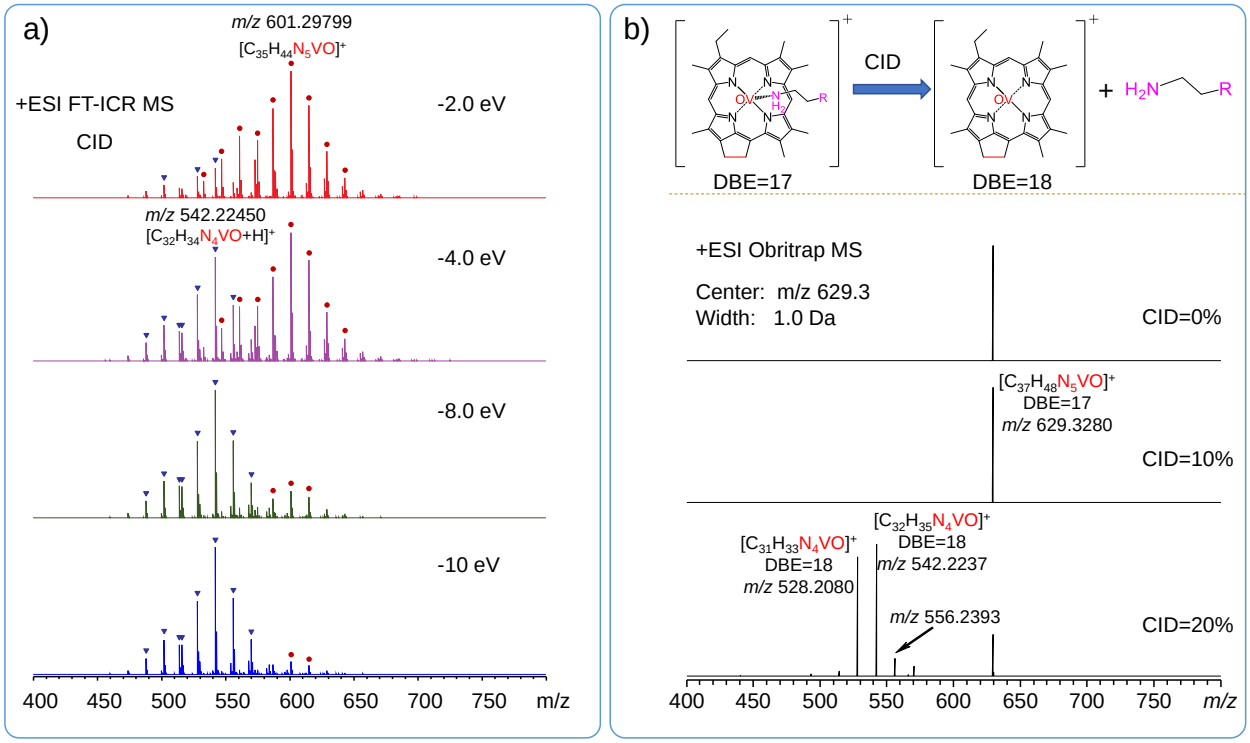

Figure 5.5 Spectra of CID analysis on vanadyl porphyrin fraction by FT-ICR MS a), and isolation collision analysis on *m/z* 629.3 by Orbitrap MS b)

To further confirm this inference, multi-stage isolation collision experiments were conducted on the vanadyl porphyrin fraction using Orbitrap MS. Orbitrap has an ultrahigh-resolution second only to FT-ICR, and can implement multi-stage MS function. Figure 5.5 b) shows the spectra of isolation collision analysis on vanadyl porphyrin fraction with (+) ESI Orbitrap MS. $[C_{37}H_{48}N_5VO]^+$ porphyrin ion with a molecular weight of 629.3280 Da and a DBE value of 17 was well isolated and the width of isolation window was 1.0 Da. When the CID energy set to 10%, no fragment ions had been detected revealing that these cluster ions have a certain stability. When the CID energy increased to 20%, the vast majority of $[C_{37}H_{48}N_5VO]^+$ fragmented and produced several kinds of N_4VO type porphyrin ions with a DBE value of 18. The occurrence of these N_4VO peaks indicated that $[C_{37}H_{48}N_5VO]^+$ is the aggregated ions of porphyrin ions with molecules having the formula $C_nH_{2n+3}N_1$, which corresponds to small amine molecules. MS^3 experiment was also performed to exclude the possibility of N_4VO peaks producing by C-C bond breaking at 20% CID. $[C_{36}H_{48}N_5VO]^+$ (has a DBE value of 16) was selected as the parent ion, and $[C_{31}H_{35}N_4VO]^+$ produced by the fragmentation was selected as the secondary precursor ion. $[C_{31}H_{35}N_4VO]^+$ (has a DBE value of 17) is the ion of porphyrin belong the ETIO type, without naphthenic ring on the side chain substituent. As shown in Figure 5.6, almost no $[C_{31}H_{35}N_4VO]^+$ ions fragmented when CID energy was set as 20%.

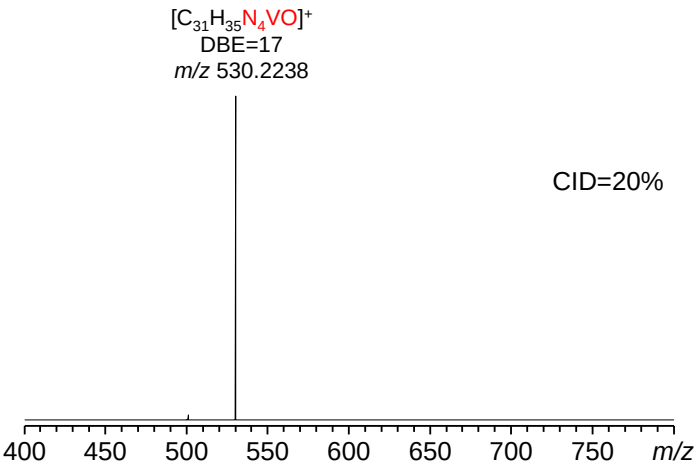

Figure 5.6 MS3 spectrum of $[C_{31}H_{35}N_4VO]^+$. The precursor ion was $[C_{36}H_{48}N_5VO]^+$ (DBE=16) the isolation width values were 1.0 Da, the Collision Voltages were 20%

Hence, the N_4VO type ions generated by CID were not from C-C bond fragmentation but disaggregated from aggregated ions. These ions fragmented during the transmission in TIMS-TOF MS and produced the corresponding N_4VO porphyrin ions and amine molecules, failed to appear on the mass spectra. The peaks of series 2 should be correspond with these aggregated ions of porphyrins and amines. The series 1 presents the mobility peaks of N_4VO type porphyrin compounds. The ions of N_5VO type disaggregated and formed N_4VO before arriving the mass spectrometer detector. The EIM peaks of series 2 were wider than those of series 1 due to the diversity of composition.

Moreover, these N_5VO type would absence when ionization promoter such as $HCOONH_4$ was added into the solution, revealing that the aggregate will be destroyed when other charged particles intervene. Aggregation of porphyrins with other compounds in petroleum should be common especially in asphaltene fraction due to the special distribution of electron cloud, possessing pi-electrons[235-238]. The observation of porphyrin cluster ions via ESI TOF MS indicated that part of the porphyrins in crude oil are present in form of aggregated molecules. The difficulty for these aggregated ions to reach the mass detector should attribute to external influence, such as ionization promoter and collision during transmission.

5.3.2 Characterization of model compounds by TIMS-TOF MS

Twelve porphyrin standards were analyzed by (+) ESI TIMS-MS for a fuller understanding of the behaviors of porphyrins ion in mass spectrometry. Figure 5.7 shows the EIM spectra of $[M+H]^+$, $[M+Na]^+$, $[2M+H]^+$, $[2M+Na]^+$ and $[M+MP+H]^+$ for VO-OEP porphyrin ions. $[M+H]^+$, $[M+Na]^+$, $[2M+H]^+$ and $[2M+Na]^+$ were observed with CCS values of 299.0 $Å^2$, 306.6 $Å^2$, 402.4 $Å^2$, and 418.2 $Å^2$, respectively.

There are three peaks in Figure 5.7, Peak α, Peak β and Peak γ, should be expounded. Peak α is the EIM of porphyrin-morpholine aggregated ions captured by TIMS and cracked into porphyrin ions during the

transmission. The aggregated ions cleaved and produced $[M+H]^+$ fragment, and their ion mobility peaks fell on the EIM spectrum of $[M+H]^+$, which is similarly to series 2 shown in Figure 5.3. Morpholine may come from pump oil or even air because it can be used as a metal corrosion inhibitor and rust inhibitor. Peak β should be smaller ions than $[2M+H]^+$ ion captured by TIMS but aggregated to form $[2M+H]^+$ during transmission and detected by mass spectrometry. This indicated that the aggregation and disaggregation processes of ions may occur simultaneously during mass spectrometry transmission. Of course, from the current results, the disaggregation process is dominant. Peak γ should be the aggregated ions of $[M+MP+H]^+$ with an unknown contaminant, which have a similar mechanism to Peak α.

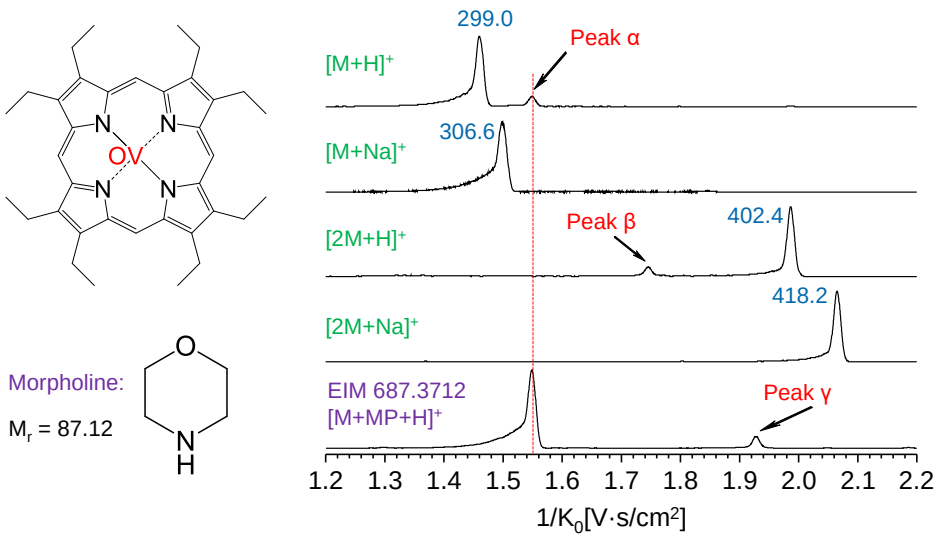

Figure 5.7 EIM spectra of $[M+H]^+$, $[M+Na]^+$, $[2M+H]^+$, $[2M+Na]^+$ and $[M+MP+H]^+$ for VO-OEP. MP: morpholine

The EIM spectra of 11 other porphyrin standards are shown in Figure 5.8. Each porphyrin produces different ions when ionized, and their EIMs also have different characteristics. It should be noted that the ionization products of TPPs were less than that of OEPs. This could contribute to the steric hindrance of the phenyl groups made them difficult to form dimer. The CCS values for these porphyrins determined by TIMS-MS could be used as a CCS value reference. Although CCS values of specific molecules vary with different instrument and parameter setting the CCS values in this paper can facilitate the presentation. Dimeric porphyrin ions were detected here confirming that the aggregated porphyrins by π-π interaction can be well ionized. There is no signal of dimeric porphyrin ions in vanadyl porphyrin fraction maybe because the concentration is not enough, even if enrichment pretreatment was performed. Considering the wealthiness of aromatics in petroleum especially asphaltene fraction, the existence of these aggregated porphyrin molecules is very reasonable. But whether they can be ionized in ESI is unascertainable.

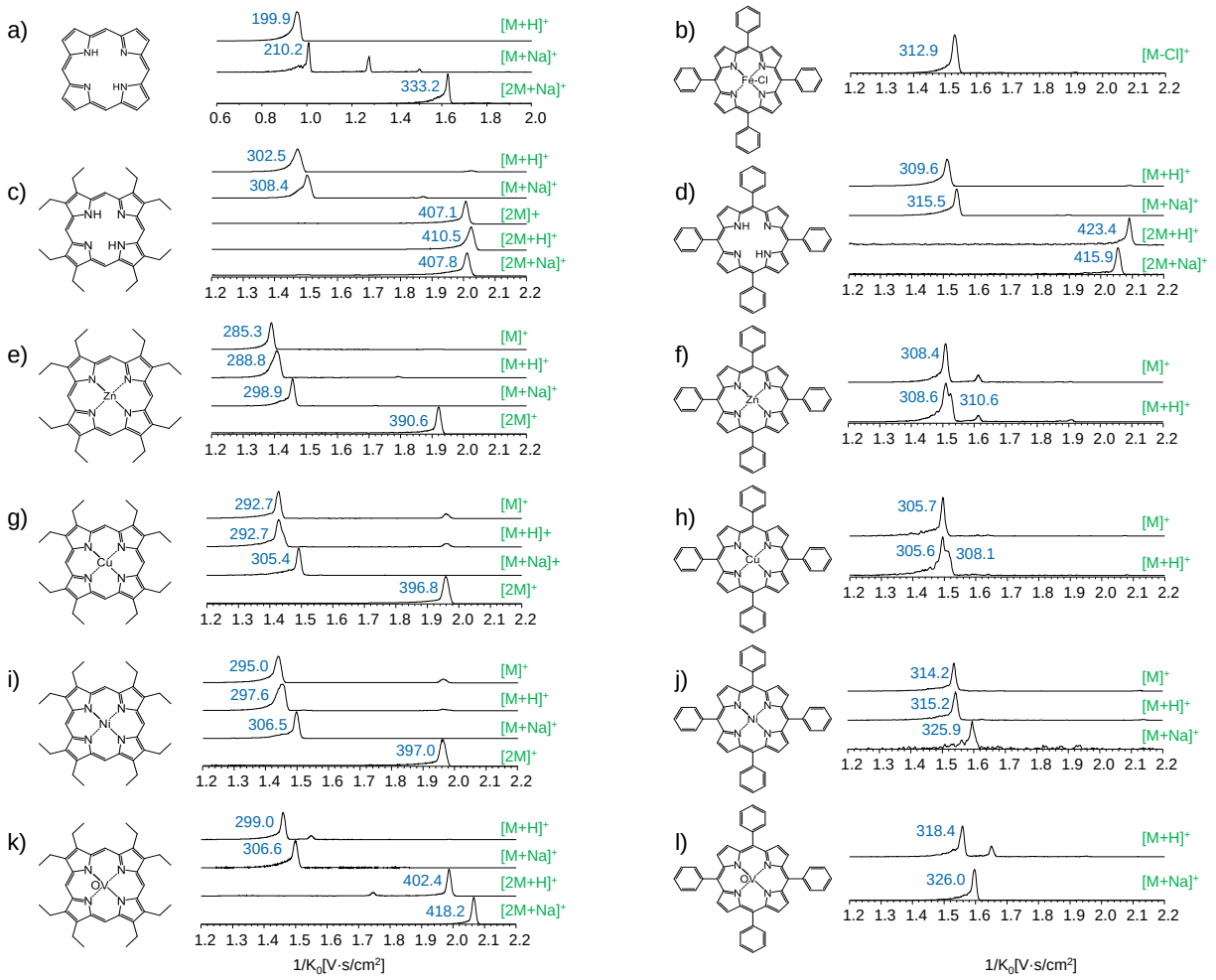

Figure 5.8. Molecular structures of porphyrins and their extracted ion mobility (EIM) spectra analyzed by TIMS-TOF MS of (a) $[M+H]^+$, $[M+Na]^+$,$[2M+Na]^+$ for porphine, (b) $[M-Cl]^+$ for Fe-TPP, (c) $[M+H]^+$, $[M+Na]^+$, $[2M]^+$, $[2M+H]^+$ and $[2M+Na]^+$ for octaethylporphine, (d) $[M+H]^+$, $[M+Na]^+$, $[2M+H]^+$ and $[2M+Na]^+$ for tetraphenylporphyrin, (e) $[M]^+$, $[M+H]^+$, $[M+Na]^+$ and $[2M]^+$ for Zn-OEP, (f) $[M]^+$ and $[M+H]^+$ for Zn-TPP, (g) $[M]^+$, $[M+H]^+$, $[M+Na]^+$ and $[2M]^+$ for Cu-OEP, (h) $[M]^+$ and $[M+H]^+$ for Cu-TPP, (i) $[M]^+$, $[M+H]^+$, $[M+Na]^+$ and $[2M]^+$ for Ni-OEP, (j) $[M]^+$, $[M+H]^+$ and $[M+Na]^+$ for Ni-TPP, (k) $[M+H]^+$, $[M+Na]^+$, $[2M+H]^+$ and $[2M+Na]^+$ for VO-OEP, (l) $[M+H]^+$ and $[M+Na]^+$ for VO-TPP. The numbers marked are CCS values of the corresponding mobility peaks determined by TIMS-TOF MS. The unit of the CCS values is $Å^2$

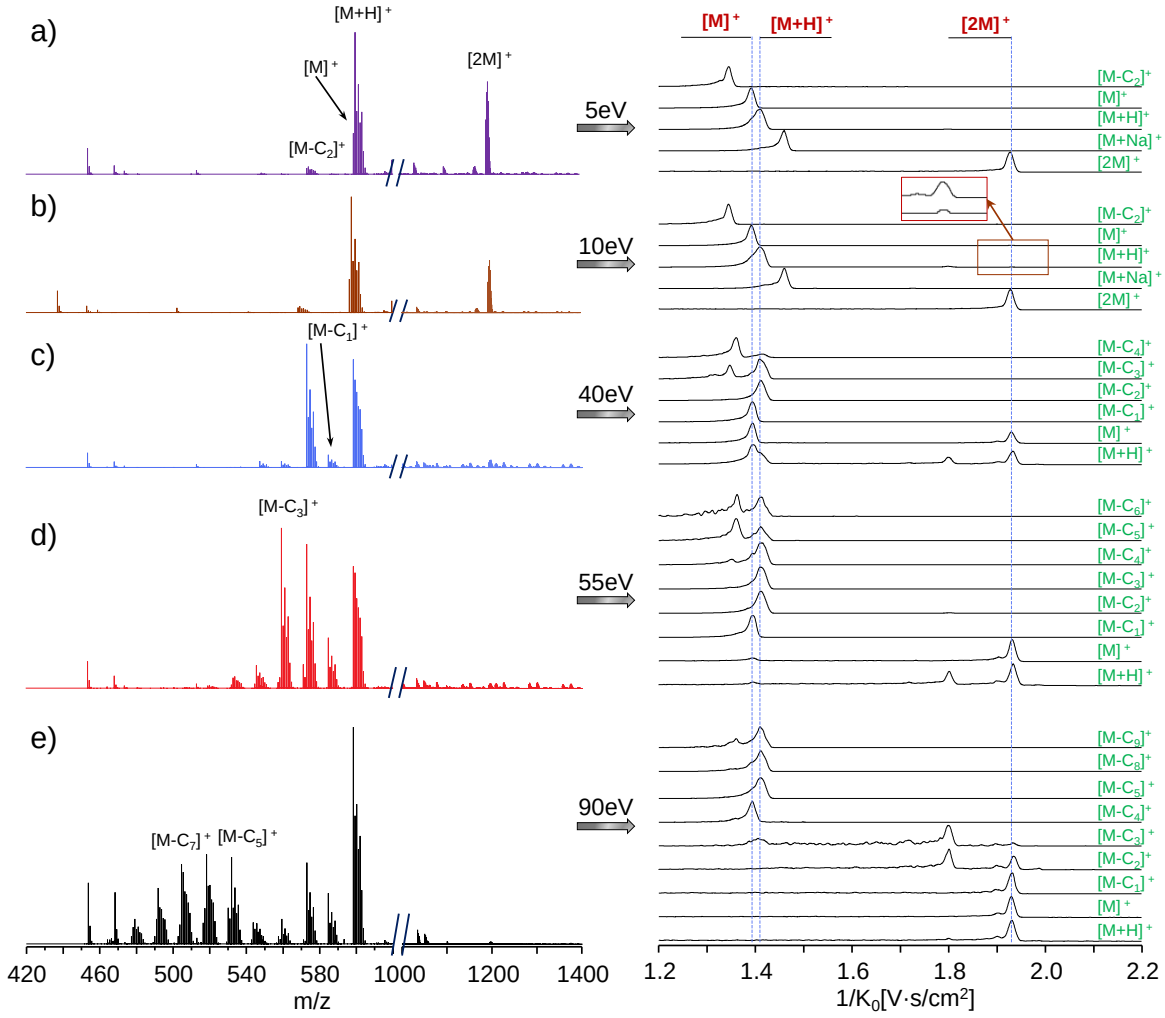

Figure 5.9 Mass spectra (left) and their corresponding EIM spectra (right) of Zn-OEP under different CID conditions. The molecular weight of Zn-OEP is 596.2852

CID experiments were performed on Zn-OEP via TIMS TOF MS, for comprehensive understanding of the ionization and fragmentation behavior of petroporphyrins. Zn-OEP was chosen because it does not contain oxygen atoms, avoiding the aggregation caused by oxygen, and Zn-OEP is the closest to planar. Mass spectra and their corresponding EIM spectra of Zn-OEP under different CID conditions were shown in Figure 5.9. More fragment ions were detected with the increasing of collision energy. The peak clusters in the left side of the $[M]^+$ corresponded to ions lost methyl or methylene groups.

Precursors did not conduct fragmentation at the collision energy of 5 eV. As shown in Figure 5.9a, $[M\text{-}C_2]^+$, $[M]^+$, $[M+H]^+$, $[M+Na]^+$, and $[2M]^+$ were detected. $[M\text{-}C_2]^+$ was captured by TIMS and an individual mobiligram was generated indicating the $[M\text{-}C_2]^+$ was produced before ion mobility tube instead of fragments for other ions. Gas chromatography analysis confirmed that deethylation product of the Zn-OEP existed in the raw sample (see Figure 5.10). When CID was set to 10 eV, the MS and IMS spectra were similar to that

of 5 eV CID, except that the abundance of $[2M]^+$ decreased. The enlarged view of the spectra showed that trace amount dimers began to fragment and form $[M]^+$ or $[M+H]^+$. $[M-C_4]^+$, $[M-C_3]^+$, and $[M-C_1]^+$ appeared on the mass spectrum when CID increased to 40 eV (Figure 5.9c). The sharply increase of $[M-C_2]^+$ indicated that Zn-OEP ions were liable to lose an ethyl group. The mass peaks of $[2M]^+$ and $[2M+H]^+$ were disappeared from the mass spectrum indicated these ions were cleaved into $[M]^+$ and/or $[M+H]^+$. With a 55 eV CID, almost all of the $[M]^+$ and $[M+H]^+$ detected by mass spectrometry were from the fragmentation of aggregated ions (Figure 5.9d). The $[M]^+$ and $[M+H]^+$ generated in ionization source were completely cleaved into smaller ions. With high CID, fragmentation was more severe, which was step by step cleavage from aggregated ions to monomer then to dealkylated fragments.

The EIMs in Figure 5.9c) showed that $[M+H]^+$ ions were easier to fragment to generate smaller fragment ions than $[M]^+$. This indicated that $[M+H]^+$ has a lower dissociation energy. The vast majority of $[M-C_4]^+$ came from deethylation product of the Zn-OEP. No $[M+Na]^+$ were broken into $[M]^+$ or smaller ions for Zn-OEP. The $[M+Na]^+$ would disintegrate instead of stepwise cleavage like $[M+H]^+$ when the collision energy was enough. This may because the entire $[M+Na]^+$ clumped together with the presence of sodium ion.

A peak was found in some EIM spectra with a $1/K_0$ value of about 1.8. It should be from the cluster ions of Zn-OEP with an unknown contaminant, which has a molecular weight of 356.28, however the composition of this compound was not assigned. The phenomenon further illustrates the porphyrins have strong aggregation ability with other molecules, not only between porphyrins by pi-stacking. It is conceivable that aggregation of porphyrins would be common and very complex when they are occurring in a complex matrix such as petroleum. The results imply that we need to re-evaluate the interpretation of mass spectrometry data obtained in recent years on petroleum porphyrin characterization.[54] By comparing data from different operation conditions, structural information could be obtained, especially for that of "non-porphyrins",[239] which might be large molecules containing petroporphyrin structural unit.

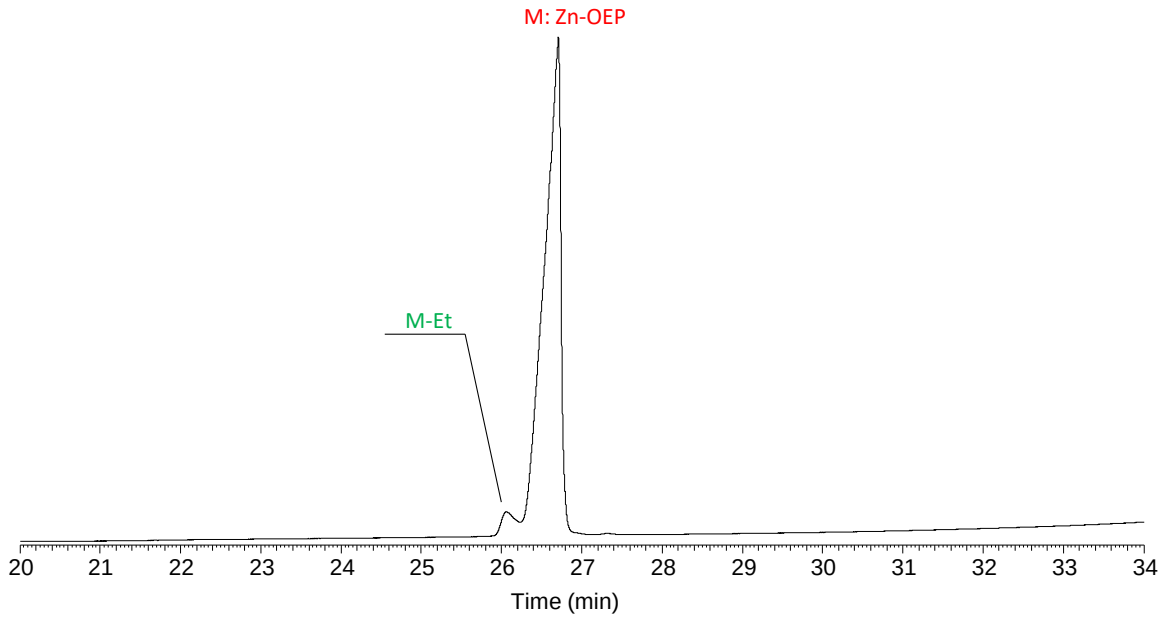

Figure 5.10 GC chromatogram of the Zn-OEP. The experiment was carried out in an Agilent 6890N chromatograph, equipped with an Analytical Control HT790 column 5 m long, 0.53 mm internal diameter, and 0.1 μm thick stationary phase. A flame ionization detector (FID) with a flame of air and hydrogen at a temperature of 430 ℃ was used. The initial temperature of the column oven is 40 ℃ , and it is heated to 430 ℃ using a rate of 15 ℃ /min. Then temperature remains constant for 5 min

5.3.3 Aggregation and fragmentation behavior of porphyrin ions

It can be appreciated from the previous results that petroporphyrin ions have undergone complex changes during transmission after the ionized in ionization source and finally detected by the detector. $[M]^+$, $[M+H]^+$, $[M+Na]^+$ and cluster ions of petroporphyrins could be produced in (+)ESI. The dissociation energy of dimeric porphyrin ions such as $[2M]^+$ and $[2M+H]^+$ are very low. Even in transport channel, no collision energy function, the ions will be disaggregated into $[M]^+$ and $[M+H]^+$ because the collide between ions themselves, or with gas molecules. With the increasing of collision energy, $[M]^+$ and $[M+H]^+$ will lose the side chain substituents (i.e., methyl, ethyl and phenyl), and break up into smaller ions. The dissociation energy of $[M+H]^+$ is lower than $[M]^+$. Disaggregation of dimers and fragmentation of monomers to $[M\text{-}C_n]^+$ occur simultaneously.

When vanadyl porphyrins from petroleum were characterized by (+)ESI TIMS-TOF MS, $[M+H]^+$ and cluster ions such as $[M+H]^+$ & porphyrin, $[M+H]^+$ & amine and $[M+H]^+$ & unknown species in petroleum were detected by TIMS. Therefore, we propose that a portion of porphyrin molecules exist in the form of aggregates in petroleum. The previous characterization on vanadyl petroporphyrins by mass spectrometry usually can only detect the signal of $[M+H]^+$, which should be attributed to the disaggregation of these cluster ions during transmission as well the absence of these aggregates caused by ionization promoter. TIMS, close

proximity to the ionization source, provided the direct observation of porphyrin aggregates reside in petroleum rather than $[M+H]^+$ only detected by MS. The complex process of the porphyrin ions suffering during transmission observed here suggests re-evaluate the interpretation of mass spectrometry data obtained in recent years on petroporphyrin characterization.

5.4 Conclusions

The characterization of vanadyl porphyrins from the heavy crude oil showed that part of vanadyl porphyrins in petroleum exist as aggregated molecules. These aggregates could be ionized in ESI but most of the cluster ions will disaggregate and generate $[M+H]^+$ before reaching the mass spectrometer detector. These aggregates of porphyrins will absence when other charged particles intervene, such as ionization promoter. The results of CID showed that $[M]^+$ and $[M+H]^+$ were damaged into fragment ions and porphyrin cluster ions were disaggregated into $[M]^+$ and $[M+H]^+$ simultaneously. The application of the combination of IMS with Q-q-TOF MS reveals the ionization, aggregation and fragmentation status of porphyrin ions in ion produce and transfer.

Chapter 6. Existence form of "non-porphyrin" in asphaltenes

6.1 Introduction

The "non-porphyrin" in petroleum refers to those nickel and vanadium metal compounds that have no characteristic absorption in UV-vis. At the same time, these metal compounds are also difficult to be ionized and detected by mass spectrometry. However, no “non-porphyrin” compounds have been confirmed to date.

There are three inferences about the existence of "non-porphyrin": First, “non-porphyrin” is aggregates of petroporphyrins with asphaltene molecules. Due to the influence of asphaltene matrix, these porphyrin compounds are no characteristic absorption in the ultraviolet spectrum; secondly, “non-porphyrin” is coordination compounds formed by heteroatom compounds such as N, O, S with petroleum porphyrin. The effect of coordination makes the characteristic absorption peaks of porphyrin compounds deviate to varying degrees. After the superposition, the absorption peak tends to be smooth, and then the characteristic absorption peak disappears; third, the “non-porphyrin” has a different structure from the petroporphyrins. However, there is no strong evidence for the identification “of non-porphyrins”, and no “non-porphyrin” compounds have been confirmed yet.

This chapter, Canadian oilsands bitumen, Venezuelan crude oil asphaltenes, and Qingchuan gilsonite were taken as the objects and several of chemical derivatization methods were designed to process the asphaltenes to definite the existence of metal compounds inside, such as acid treatment, hydropyrolysis, methanesulfonic acid demetalization, and silanization. With the help of UV-Vis and positive-ion ESI FT- ICR MS, high temperature GC-AED and GPC-ICP MS, the possible forms of "non-porphyrin" were confirmed as well the existence of metallic nickel and vanadium compounds in asphaltenes.

6.2 Experiment section

6.2.1 Samples and reagents

Sample: n-C_7 asphaltenes derived from Venezuelan crude oil; SFEF fractions of Canadian oilsands bitumen-derived vacuum residue; Qingchuan gilsonite toluene soluble fraction.

Reagents: methanesulfonic acid, hydrochloric acid, N, O-bis(trimethylsilyl)trifluoroacetamide (BSTFA), trimethylchlorosilane (TMCS), pyridine, isopropanol, ultrapure water, diatom soil, sodium hydroxide (NaOH), dimethylformamide (DMF), tetrahydrofuran (THF), VO-OEP, octaethylporphine, n-butylamine and other reagents were purchased from Sigma-Aldrich Reagent Company. Analytical grade n-heptane, dichloromethane (DCM), toluene, methanol (MeOH) and other solvents were purchased from Beijing Chemical Reagent Company, and used after re-evaporation to improve purity.

6.2.2 Methanesulfonic acid demetallization of Qingchuan gilsonite

100 mg Qingchuan gilsonite was dissolved in 10 mL of toluene, and 5 mL of isopropanol and 5 mL of methanesulfonic acid were added, heating at 100 ℃ for 1 h for the reaction. Then the temperature was increased to 130 ℃ and heating for another 2 h. After the reaction, 60 mL of ultrapure water and 20 mL of n-heptane were added. Ultrasonic was used for 5 minutes to mix the mixture thoroughly. Then to separate the upper oil phase and the lower water phase by centrifuged. This step was repeated three times. The solvent the organic phases was evaporated, and 10 mL of n-heptane was added to obtain the n-heptane soluble organic phase (oil phase); solid sodium bicarbonate powder was added in the water phases to neutralize unreacted methanesulfonic acid until there is no bubbles. DCM was used to extract the organic compounds (DCM 1 phase) from the water phase. The stripped phase was washed three times with pH=10 sodium hydroxide aqueous solution, and then the water phase was extracted with DCM to get organic compounds (DCM 2 phase).

6.2.3 Acid treatment on Qingchuan gilsonite

10 mg Qingchuan gilsonite was dissolved in 0.5 mL toluene, and 0.5 mL of methanol containing 10% (v) hydrochloric acid was added. The treatment time was 10 minutes, and intermittent ultrasound was performed. After reaction, the mixture was washed with 20 mL of ultrapure water for 4 times. Collect the water phase and adjust the pH of the aqueous phase to 10 with NaOH aqueous solution. Then extracted the organic components with 100 mL of DCM for 5 times. The DCM was then volatilized to the remaining 3 mL for subsequent analysis.

6.2.4 Acid treatment on Venezuela VR asphaltenes

The asphaltenes was loaded on diatomaceous earth, which was derived from Venezuelan VR. The loaded solid mixture was extract with n-heptane (n-C_7) and then with methanol (MeOH) to obtain the MeOH-1 extraction fraction; after acidification with MeOH solution containing 7% volume concentration HCl for 3 h, MeOH extraction was performed again to obtain the MeOH-2 extraction fraction; stripped phase was then extracted with DCM to obtain the DCM fraction. After evaporating the solvent, each component was desalted and deacidified with silica gel saturated with 80% water.

6.2.5 Hydrogen pyrolysis experiments on Venezuela VR asphaltenes

1.0 g of n-heptane asphaltene was dissolved with DCM and 15 g of diatomaceous earth was added for loading. Hydrogen pyrolysis experiments were performed on the loaded solid mixtures. The temperature settings were 330 ℃ (1#), 350 ℃ (2#), 370 ℃ (3#), 390 ℃ (4#) and 410 ℃ (5 #). The hydrogen pressure was 2 MP, and the reaction time was 2 h. 0# served as the control group without pyrolysis. After the reaction, the mixtures were extracted with toluene methanol 1:1 to obtain the solute. The product quality yields were 64%, 60%, 51%, 45%, 19% and 98%, respectively.

6.2.6 Silanization experiment on DMF insoluble of Venezuelan crude oil asphaltene

0.5 g of DMF-insoluble fraction (DMFSI) of Venezuelan crude oil heptane asphaltene was dissolved with 50 mL THF. 3 mL pyridine, and silanization reagents (1 mL BSTFA and 0.5 mL TMCS) were added. The mixture was heated and condensed to reflux for 1 h, and the heating temperature was 80 ℃. The air in the device was replaced with nitrogen before heating. After the reaction, 1.5 mL of the reaction solution was taken out and evaporated to dryness, then dissolved in THF, and analyzed by GPC-ICP MS.

6.2.7 GC-NCD analysis

The GC-NCD analysis was carried out in an Agilent 7890B chromatograph coupled with a Nitrogen chemiluminescence detector, equipped with an Analytical Control HP-5 column 30 m long, 0.25 mm internal diameter, and 0.25 μm thick stationary phase. The initial temperature of the column oven is 80 ℃, and it is heated to 3000 ℃ using a rate of 10 ℃/min. Then temperature remains constant for 10 min. The temperature NCD burner was set to 900 ℃, the burner pressure was maintained at 260 Torr, the detector temperature and pressure were set to 260 ℃ and 10.2 Torr, and the flow rates of oxygen and hydrogen were 10.2 L/min and 3.4 L/min, respectively.

6.2.8 GPC-ICP MS analysis

The sample was diluted 200-fold with THF for GPC-ICP-HR-MS detection. A 20 μL sample was injected and eluted with a THF flow rate of 1 mL/min for 120 min. A splitter was used after the columns to obtain a low-flow outlet (50 μL/min) to feed the ICP-HR-MS. A custom-made Microsoft Excel spreadsheet was used to deconvolute the chromatograms by summing the Gaussian curves.

6.3 Results and discussion

6.3.1 Coordinated petroporphyrin compounds - N_5VO

In chapter 5.2.1, N_5VO type coordination porphyrin compounds were characterized in detail. In Figure 2.7, the peaks of vanadium porphyrins in the SFEF12 and SFEF13 fractions showed obvious bimodal distribution. The positive-ion ESI FT-ICR MS spectrum of SFEF13 is shown in 6.1.

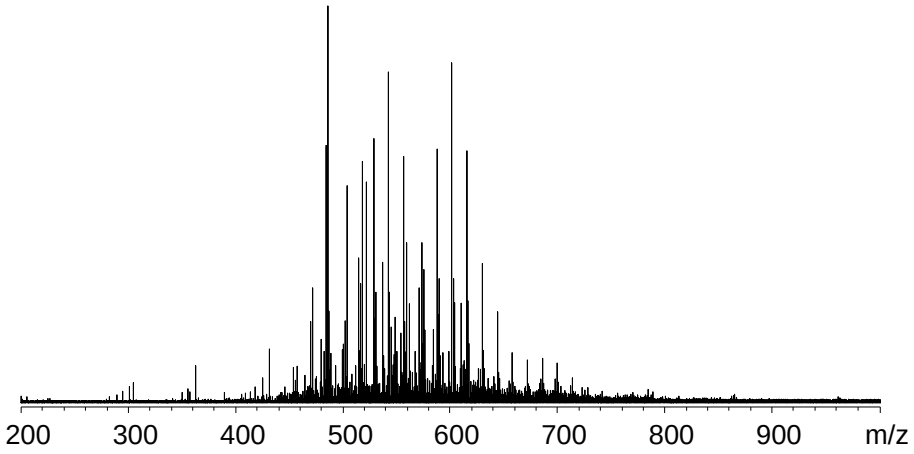

Figure 6.1 Positive-ion ESI FT-ICR MS broadband spectrum of SFEF fraction SFEF13

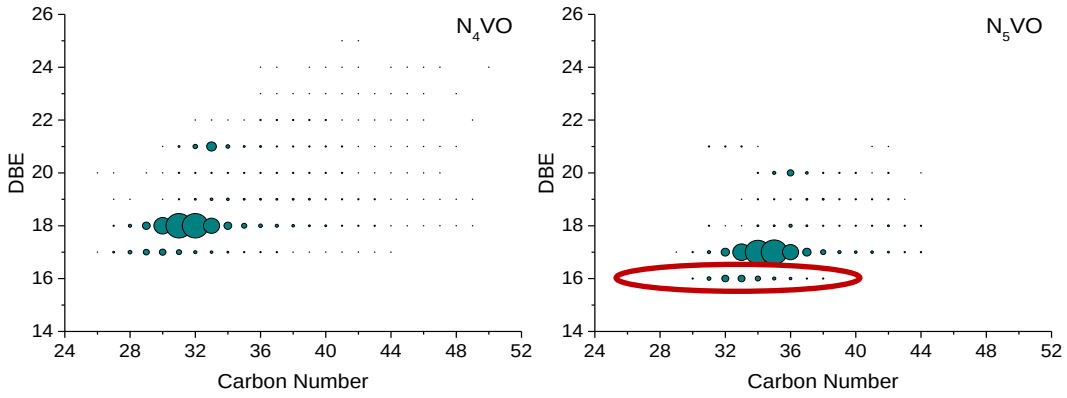

Figure 6.2 Relative ion abundance plots of DBE as a function of carbon number derived from positive-ion ESI FT-ICR mass spectra for N_4VO and N_5VO class species in SFEF13

The peaks in the range of *m/z* 470-550 are the peaks of N_4VO type vanadyl porphyrins' hydrogenated ions, and the peaks in the range of *m/z* 550-650 was identified as the hydrogenated ions of N_5VO type vanadyl porphyrin. Detailed analysis of the DBE and carbon number distribution of these two vanadium-containing compounds is shown in Figure 6.2. The DBE and carbon number range of N_4VO compounds are 17-25 and 16-50, respectively. And the center of mass distribution is at DBE=18, carbon number 31/32. The DBE and carbon number range of N_5VO compounds are between 16-21 and 28-44, respectively. And the center of mass distribution is at DBE=17, carbon number 34/35. Comparing the distribution of N_4VO and N_5VO compounds carefully, it could be found that the latter one is like the former one shifted down by one unit and shifted to the right by 3 units. It is speculated that the porphyrin compound of the N_5VO type should be the N_4VO compound plus the carbon number of about 3. It is formed by saturated ammonia molecules, and it

can only be formed by coordination, not the side chain amine molecular structure, because the DBE of N_5VO compounds starts at 16, not 17.

6.3.2 Quantification of demetalloporphyrin by demetallization on gilsonite

When the vanadium compound in Qingchuan gilsonite was characterized in Chapter 4, there was obvious characteristic absorption peak in the UV-vis. VO-OEP was used as standard sample to quantify the content of petroporphyrins and it was found that the porphyrin compound only about 15% of the nickel and vanadium metal content. The results of GC-AED and FT-ICR MS both showed that gilsonite contains a large amount of vanadyl porphyrins. This seems to be consistent with the definition of "non-porphyrin". Methanesulfonic acid demetallization experiment was conducted to verify whether there is "non-porphyrin" in the gilsonite, or it is just the influence of the asphaltene matrix that leads to the deviation of the UV spectra and the fact is that all nickel and vanadium exist in the form of porphyrin. With the function of methanesulfonic acid, the V-N and Ni-N bonds in the porphyrin will be broken and eventually form free demetallized porphyrin. By measuring the amount of demetalloporphyrin, the actual content of the metalloporphyrin compound in the gilsonite can be estimated.

Figure 6.3 shows the UV-vis spectra of DCM 1, DCM 2, oil phase of demetallized gilsonite by methanesulfonic acid, and the spectrum of raw gilsonite. It can be found that a large amount of demetallized porphyrin was concentrated in the DCM 1 phase, and the interference caused by matrix had been very slight. However, there were still UV characteristic absorption signals in DCM 2 and the oil phase, indicating that they also contain some metalloporphyrins, which also reflected that the elution method after demetallization of methanesulfonic acid is not perfect. The characteristic ultraviolet absorption wavelengths in porphyrins in DCM 2 and oil phase are slightly different from those in DCM 1, but they are the same as raw gilsonite. This may be because the structure of the porphyrin compounds in these two components is different from that of DCM 1, or due to the influence of the asphaltene matrix (DCM 2 and the oil phase are darker in color, containing some petroleum molecular compounds of gilsonite).

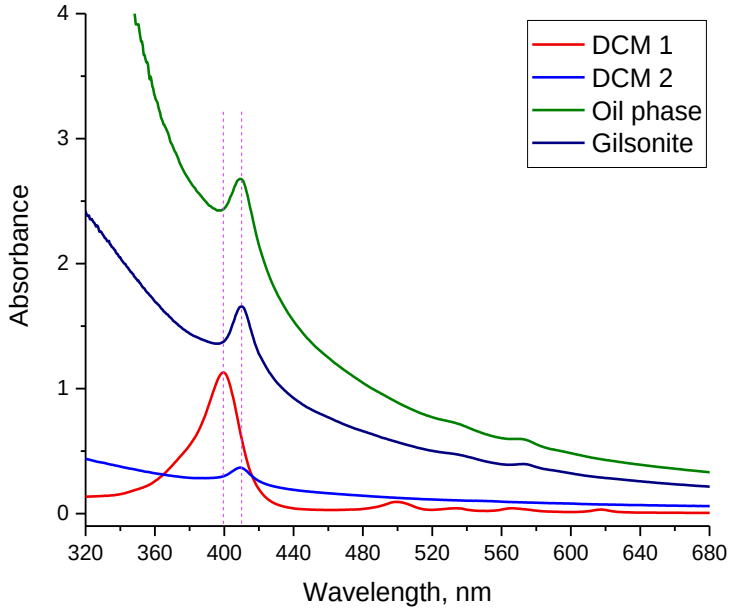

Figure 6.3 UV-vis spectra of the fractions of Qingchuan gilsonite after demetallization by Methanesulfonic acid

The characteristic absorption wavelength of demetalloporphyrin in DCM 1 fraction is the same as that of octaethylporphine. The UV-vis characteristic absorption peak areas of different concentrations of octaethylporphine were used to drew a standard curve as shown in Figure 6.4(b), and the R^2 value was 0.9999. The concentration of the demetallized porphyrins in the tested samples were calculated by taking the UV characteristic absorption peak areas of DCM 1, DCM 2 and the oil phase into the fitted curve, and then the percentage of demetalloporphyrin in the fractions could be calculated, which is shown in Table 6.1. The mass percentage of demetallized porphyrin compounds in the DCM 1 is the highest, reaching 48.4%, indicating that the demetallization experiment was very good, and most of the demetallized free porphyrin compounds were concentrated in the acidic water phase (DCM 1). The oil phase also contains a considerable amount of porphyrin compounds. UV-vis quantitative results showed that these porphyrin compounds in oil phase account for 29.2% of the total amount of nickel and vanadium in the gilsonite. The different positions of the UV-vis characteristic absorption peaks indicated that the porphyrin compounds in the oil phase and the DCM 2 fractions may be different from the demetallized porphyrin in DCM 1, but all the porphyrins in the three fractions occupied 81.7% of the total nickel and vanadium elements in the gilsonite. Although the results of this experiment failed to confirm the form of all nickel and vanadium compounds in gilsonite, at least 81.7% of them were confirmed. It is undeniable that some porphyrins will still be contained in the stripped phase (solid). Therefore, we can conclude that most (>81.7) of the nickel and vanadium metal compounds in gilsonite exist in the form of petroporphyrin, which is far greater than the direct quantification by UV-vis. It

further shows that there is a significant deviation in the quantitative analysis of porphyrin compounds by UV-vis, which will be affected by many factors.

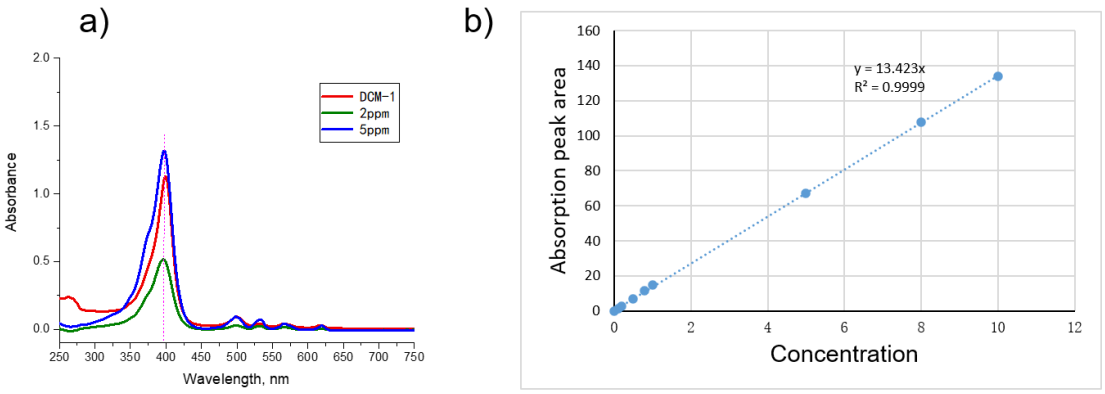

Figure 6.4 UV-vis spectra of the DCM 1 fractions and octaethylporphine (a); and fitting curves for absorption peak area and concentration of octaethylporphine

Table 6.1 Quantification of the demetalloporphyrin in the fractions

Fraction	DCM 1	DCM 2	Oil phase	Sum
γ	48.4%	4.1%	29.2%	81.7%

The analysis of DCM 1 fraction with positive ion ESI FT-ICR MS found that the demetallized porphyrin compounds occupied absolute abundance. Because of the high purity, there were many peaks of the demetalloporphyrin dimers at *m/z* 900-1000 (Figure 6.5). In the mass spectrum of DCM 1, the abundance of demetalloporphyrin with DBE=17 is the most, which corresponds to the DPEP (DBE=18) porphyrins in gilsonite. Due to the release of the metal atom in the center of the petroporphyrin, the DBE of the demetalloporphyrin reduced 1 unit. The distribution range of N_4 species is very wide, of which DBE distribution range is 16-26 and carbon number distribution range is 24-56. This is consistent with the distribution of vanadium porphyrin compounds in gilsonite.

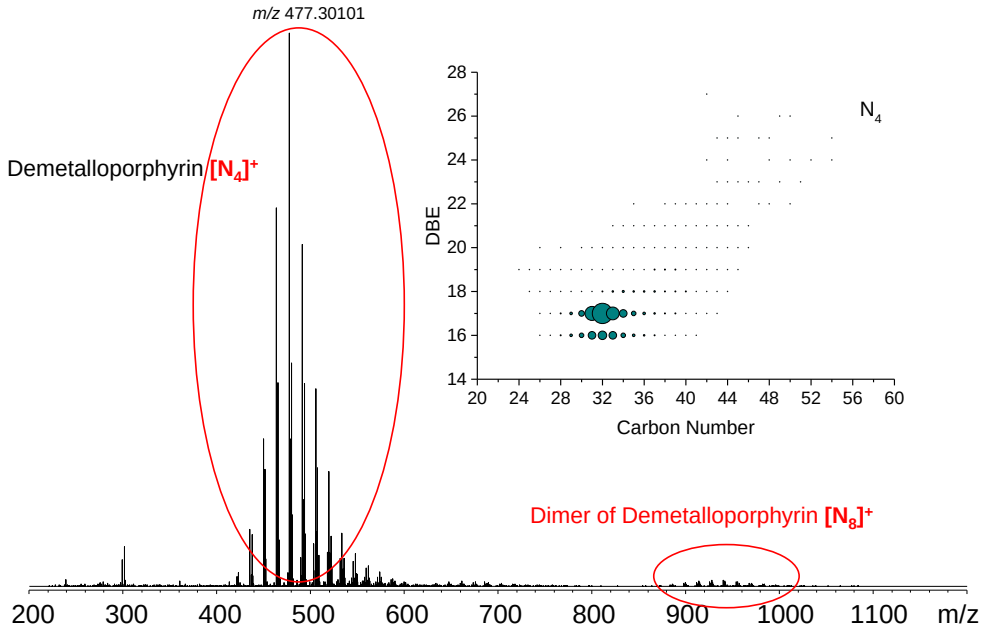

Figure 6.5 Positive-ion ESI FT-ICR MS broadband spectrum of DCM 1 fraction and relative ion abundance plots of DBE as a function of carbon number for N_4 class species

6.3.3 Quantification of ligand amines in HCl treated gilsonite

According to reports in the literature, the ligands on the porphyrins could be released with strong acids. The previous study confirmed the existence of N_5VO type coordinated porphyrin compounds in asphaltenes. In this section, concentrated hydrochloric acid was used to treat gilsonite and collect small molecular amine compounds released by eliminating coordination. The result of the GC-NCD is shown in Figure 6.6. Several types of small molecule amine compounds were detected. In order to quantify these amines, a fitting curve was drawn using n-butylamine as a standard sample, and then the molar quantity of these small-molecular amine compounds was quantitatively. The result showed that the molar quantity of these amines was 3.0 times of the content of nickel, vanadium, and iron element in the gilsonite.

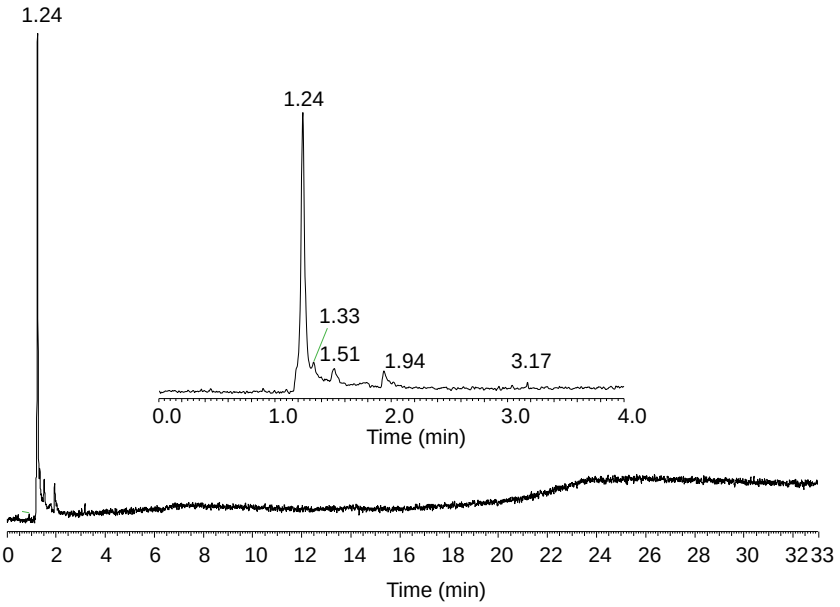

Figure 6.6 GC-NCD chromatograms of DCM fraction from HCl treated gilsonite

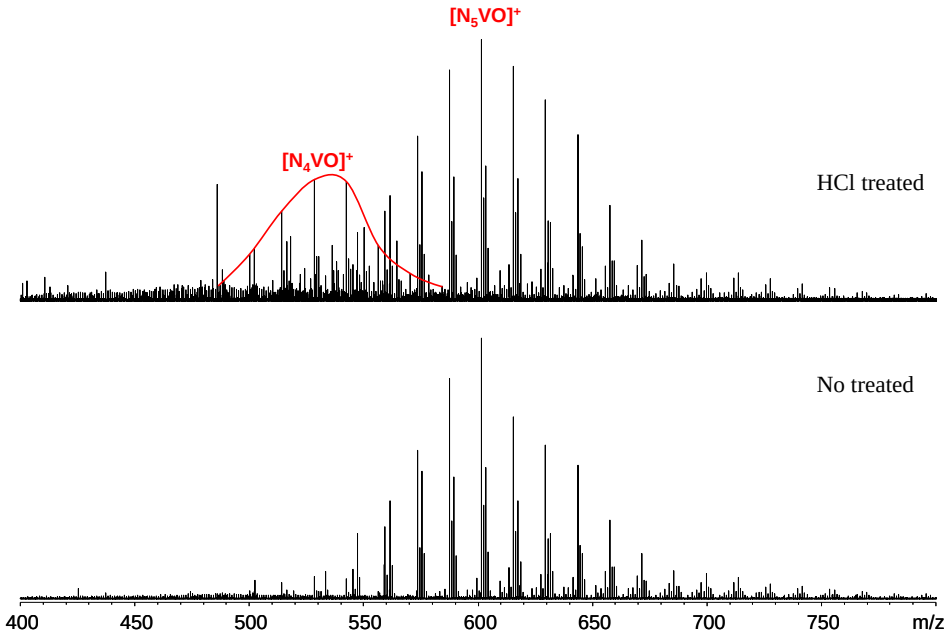

Figure 6.7 Positive-ion ESI FT-ICR MS broadband spectrum of gilsonite before and after HCl treatment

The positive ion ESI FT-ICR MS analysis results of the gilsonite before and after treated with HCl are shown in Figure 6.7. In the mass spectrum of raw gilsonite, N_5VO specie coordination compounds occupied an absolute abundance. However, after the HCl treatment, the peaks of N_4VO specie came out on the left side of the mass spectrum, which indicated that part of the coordinated porphyrins was relieved with HCl treatment. With the elution of alkaline water, the small molecule amines (ligands) were removed, and these

N_4VO specie can be directly ionized and detected by mass spectrometry. The previous GC-NCD results show that the molar quantity of small amines was 3.0 times of the nickel and vanadium metal content. This shows that these amines detected by GC-NCD have other sources, such as the hydrolysis of amide bonds, and the basic ligands of other unidentified metal compounds in petroleum.

6.3.4 Secondary extraction of porphyrins from asphaltene after acid treatment.

After HCl treatment of the asphaltenes from the Venezuelan VR, some petroporphyrins could be obtained by second extraction with methanol. The UV spectrum is shown in Figure 6.8. The MeOH-2 fraction had a characteristic absorption peak in UV-vis, but it was affected by the asphaltene matrix with a high baseline. There was still a considerable amount of porphyrin compounds in the DCM fraction of the stripped phase, indicating that methanol solvent extraction can't separate all porphyrins from the asphaltenes, even after HCl treatment. The extraction process of porphyrins in asphaltenes was dissolution equilibrium. The methanol can't extract all of the petroporphyrins due to the aggregation between porphyrins and asphaltene molecules.

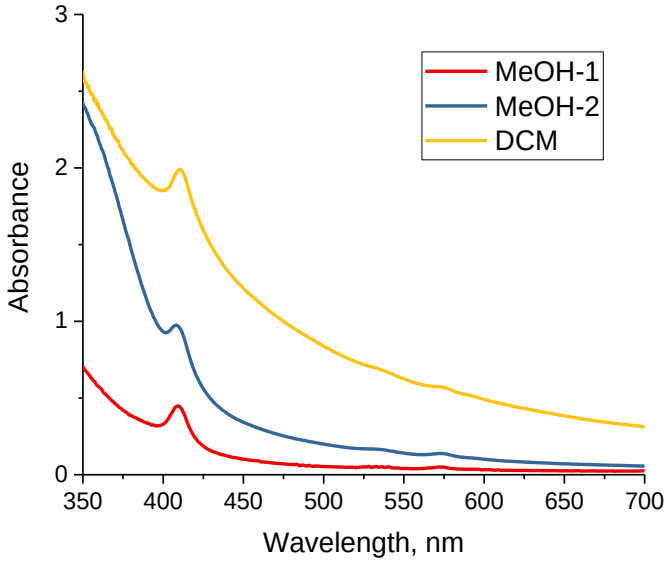

Figure 6.8 UV-vis spectra of the HCl treated fractions of asphaltenes derived from Venezuela VR

In order to quantify these metalloporphyrin compounds, the high temperature GC-AED analysis was conducted (Figure 6.9). And a quantitative curve was drawn with VO-OEP as the standard sample. The types of porphyrin compounds in MeOH-1 and MeOH-2 were similar, but the latter one was more affected by the asphaltene matrix. The quantitation results showed that the molar quantity of vanadyl porphyrins in MeOH-2 was 42.3% of that in MeOH-1. A considerable amount of vanadyl porphyrins can be extracted again by methanol after the HCl treated. The second extraction with methanol of asphaltenes without acid treatment can only obtain a vanadium yield of about 2% of the first extract. This shows that strong acids can release

the associated metalloporphyrins in asphaltenes. It also proves that a large part of the porphyrin compounds in asphaltenes exist in the associated form, so they are difficult to be separated by solvent extraction.

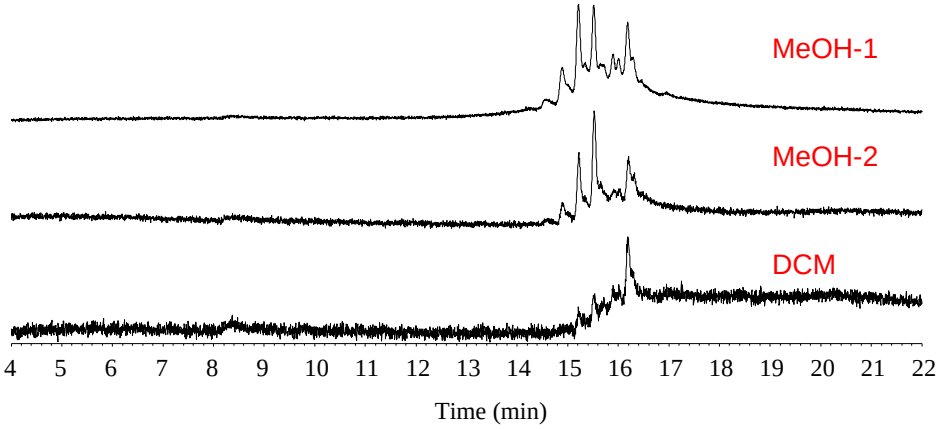

Figure 6.9 High temperature GC-AED chromatograms of the HCl treated fractions of asphaltenes derived from Venezuela VR (V element)

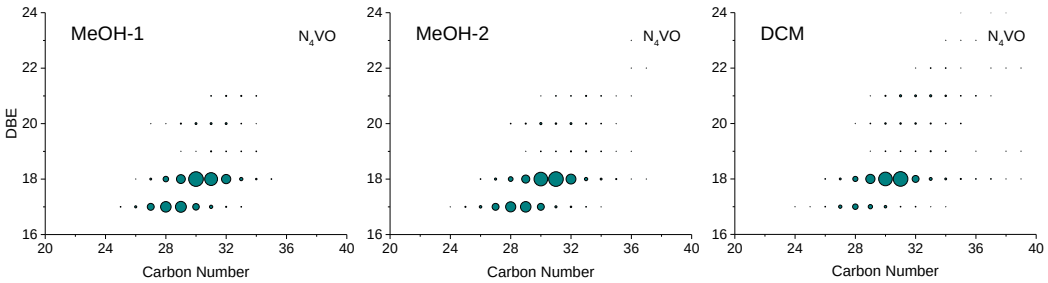

Figure 6.10 Relative ion abundance plots of DBE as a function of carbon number derived from positive-ion ESI FT-ICR mass spectra for N_4VO class species in the HCl treated fractions of asphaltenes derived from Venezuela VR; $HCOONH_4$ as ionization promoter

The positive ion ESI FT-ICR MS analysis of each fraction showed that the molecular composition of the porphyrin compounds in MeOH-1 and MeOH-2 was similar. However, the MeOH-2 fraction contained a small amount of macromolecular porphyrin compounds with higher carbon numbers and higher DBE. The porphyrin compounds in the DCM fraction had a wider distribution range, and contained more vanadyl porphyrins with high carbon number and high degree of condensation. It shows that there are larger petroporphyrins in asphaltenes, and these porphyrin compounds are tightly bound to the asphaltene matrix and difficult to be extracted by solvents such as methanol.

6.3.5 Release of associated porphyrins by hydropyrolysis of asphaltenes

There was no significant difference in the characteristic absorption spectra of the samples in UV-vis, which derived from the asphaltenes of Venezuelan VR subjected to hydropyrolysis treatments with different

temperatures. Similar to the control group (0#), all of these samples had a small characteristic absorption peak around 407 nm. No enrichment and release of petroporphyrins happened according to the UV-visible spectra.

However, the high temperature GC-AED chromatograms of these samples were obviously different. With the increased of pyrolysis temperature, nickel and vanadium compounds that could be detected by GC-AED gradually increased, especially for nickel. The signals of nickel in samples 1# and 2# were very low. Multiple peaks appeared on the GC-AED chromatogram of 3#. The signal intensity of nickel in the 5# was comparable with that of vanadium. Although the mass yield of soluble components in sample 5# was only 19%, due to the condensation and carbonization of the asphaltene matrix, more nickel and vanadyl porphyrins were released and detected by GC-AED. The GC-AED spectra of vanadium and nickel were different in the high temperature region. The spectra of nickel showed an upward trend after the peak time of about 15 minutes, while that of vanadium gradually decreased. This indicates that some aggregates of nickel porphyrins and asphaltene molecules can be vaporized in high temperature chromatography (the high temperature part has signal), while the aggregates of vanadyl porphyrins and asphaltene molecules are difficult to be vaporized in high temperature gas chromatography (there is no signal in high temperature region). This should be related to the O atom on the vanadyl porphyrin. The presence of the O atom makes the aggregation between the vanadyl porphyrins and the asphaltene molecules stronger, and the size of the aggregates might be larger, which can't be vaporized in high temperature gas chromatography. As the pyrolysis temperature increasing, smaller porphyrin compounds were continuously appearing, indicating that the side chains of porphyrin compounds are also constantly breaking when the temperature is high enough.

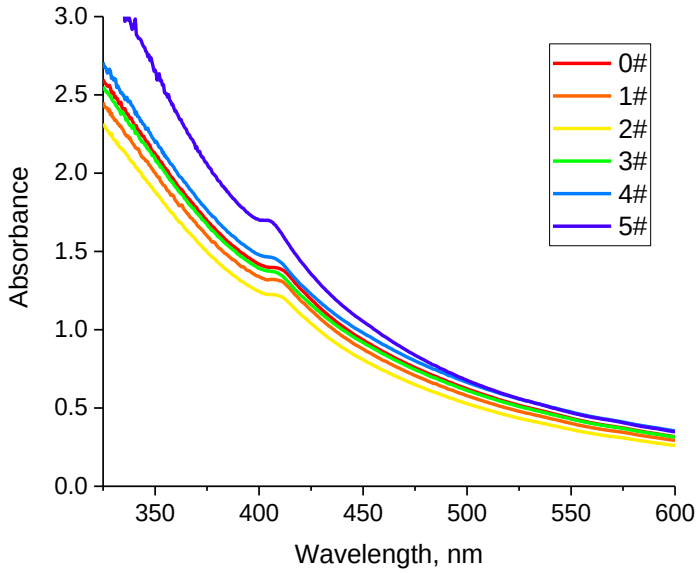

Figure 6.11 UV-vis spectra of the pyrolysis treated in hydrogen of asphaltenes derived from Venezuela VR

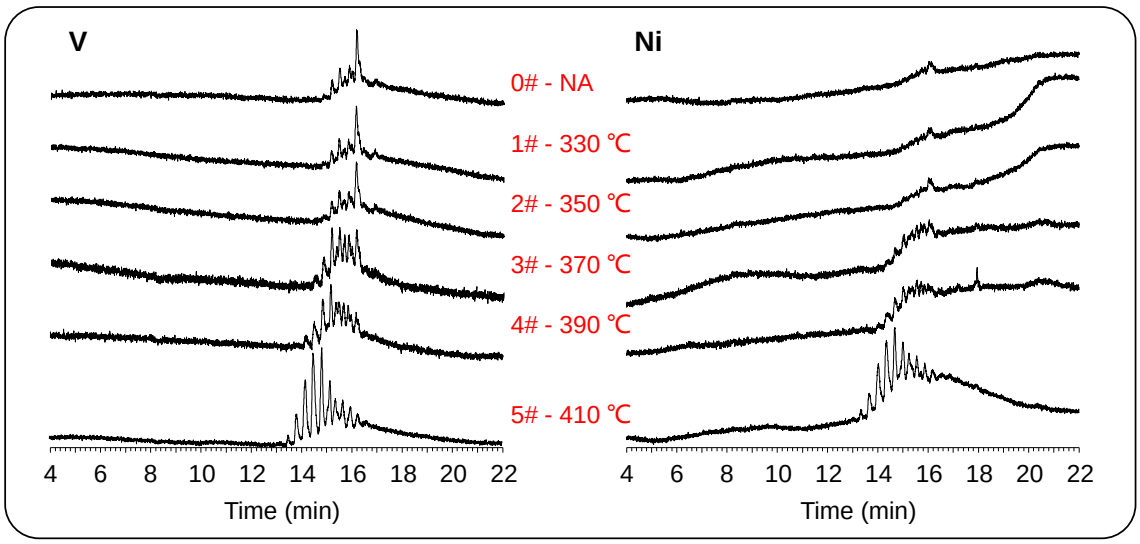

Figure 6.12 High temperature GC-AED chromatograms of the pyrolysis treated in hydrogen of asphaltenes derived from Venezuela VR (V and Ni element)

The quantitation of vanadium and nickel by ICP-MS and GC-AED in the samples are shown in Table 6.1. The standard samples were VO-OEP and Ni-OEP. The ICP-MS results showed that vanadium and nickel were not enriched with the increase of cracking temperature. The content of the Ni and V in 5# sample even decreased. However, the results of GC-AED on these samples showed that as the pyrolysis temperature increasing, the content of porphyrin that could be detected increasing. This shows that a large amount of porphyrin compounds can be released with the coking and carbonization of asphaltene molecules during the process of hydropyrolysis. Even if there was no significant difference in UV-vis, the influence of the asphaltene matrix on the UV characteristic absorption still exists. It should be pointed out that GC-AED result of vanadyl porphyrin in sample 5# was higher than vanadium content by ICP-MS. This may be because these two methods have their own instrument and operating errors. However, the results of longitudinal comparison of data still have high reference value.

Table 6.1 Quantification of V and Ni elements after pyrolysis treatment of asphaltenes derived from Venezuela VR

	ICP		GC-AED			
	V (wppm)	Ni (wppm)	V (wppm)	Fold	Ni (wppm)	Fold
0#	1895.775	438.9912	612.20	1.00	16.09	1
1#	1639.954	398.8386	536.46	0.88	15.37	0.95
2#	1399.687	412.1172	561.88	0.92	21.37	1.33
3#	1172.702	354.0189	619.41	1.01	29.73	1.85
4#	1609.347	440.6241	690.03	1.13	60.30	3.75
5#	1305.814	310.1163	2212.63	3.61	232.33	14.44

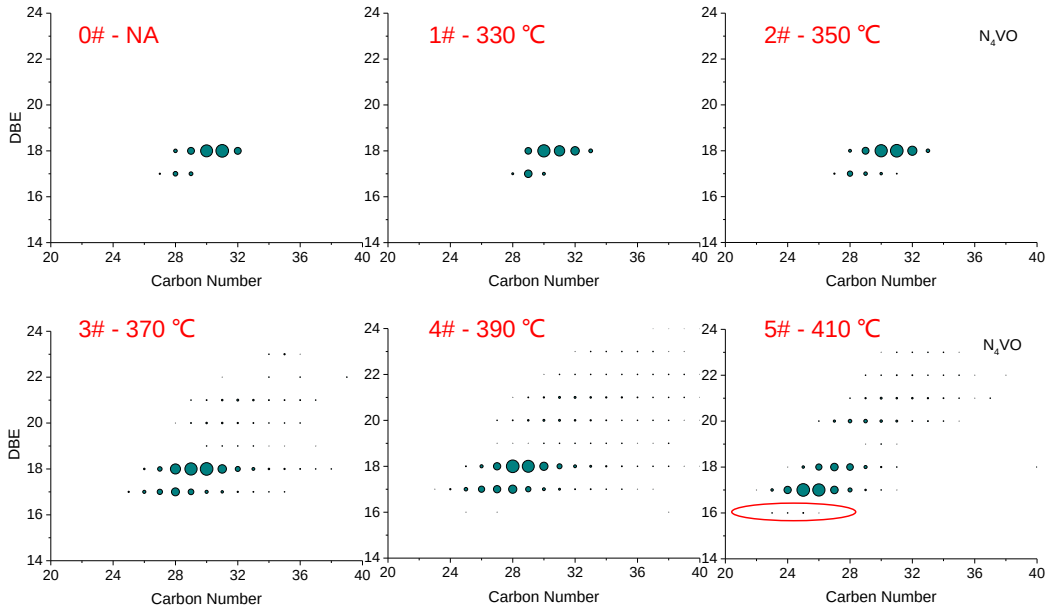

Figure 6.13 Relative ion abundance plots of DBE as a function of carbon number derived from positive-ion ESI FT-ICR mass spectra for N_4VO class species of the pyrolysis treated in hydrogen of asphaltenes derived from Venezuela VR；HCOOH as ionization promoter

The distribution of vanadyl porphyrins in each sample was characterized by positive ion ESI FT-ICR MS, as shown in Figure 6.13. The distribution of N_4VO class species in samples 1# and 2# were almost the same as those in the control group (0#), indicating that when the pyrolysis temperature below to 350 ℃, the porphyrins in the asphaltenes can't be released. More vanadyl porphyrins with high carbon number and high DBE (degree of condensation) were detected when the temperature higher than 370 ℃, indicating that vanadyl porphyrins in asphaltenes can be released at high temperatures. This is consistent with the results of GC-AED. With the increasing of temperature, the mass center of N_4VO class species in each sample shifted from DBE=18 to DBE=17, and the corresponding carbon number center was also decreasing. It is worth noting that we have detected traces of N_4VO compounds with DBE=16 in sample 5#, which belongs to the dehydrogenated vanadyl porphyrins. It shows that when the pyrolysis temperature is sufficient, the side chain hydrogen atoms of the porphyrin compound can also be broken and fall off.

6.3.6 Release of reveals hydrogen bonding in asphaltenes aggregation by silanization

Hydrogen bonding is common in petroleum systems, which plays an important role in the aggregation of asphaltene molecules. The literature also pointed out that the metalloporphyrin molecules in the asphaltenes will associate with the asphaltene molecules due to hydrogen bonding.[240] In order to prove this theory from the experimental level, and to further explore the existence of metal compounds in asphaltenes, the DMF insoluble fraction of Venezuelan crude oil n-C_7 asphaltenes was taken as the research object to do the

silanization experiment. The changes of nickel, vanadium, and sulfur elements before and after silanization were analyzed by GPC-ICP MS, and the result of vanadium is shown in Figure 6.14. Obviously, the distribution of vanadium in the asphaltene shifted to the right after the silanization. This shows that the hydrogen bond between the porphyrins and the asphaltene molecules in the asphaltene makes the them aggregated together. But the contribution of the hydrogen bond is only part of intermolecular forces, and it does not occupy an absolute role. After silanization, the spectra of nickel and sulfur also shifted to the right which were similar to vanadium. The experimental results showed that the aggregation caused by hydrogen bonds in asphaltenes is exists, and part of the hydrogen bonds can be eliminated via silanization.

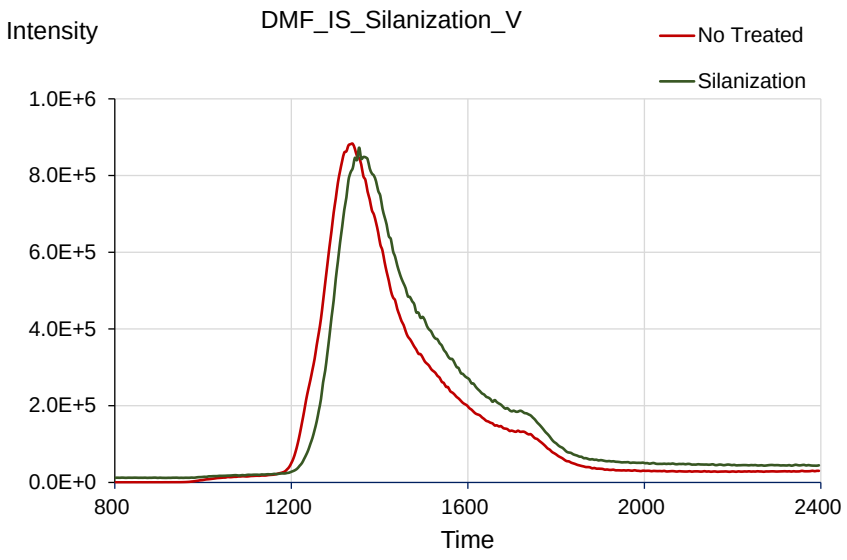

Figure 6.14 GCP-ICP MS spectra of DMF insoluble fraction before and after silanization of n-C_7 asphaltenes derived from Venezuelan crude oil

6.4 Conclusions

This chapter designed several experiments to find the trail of "non-porphyrin", and explored the existence form of metal compounds in asphaltenes. The results of high-resolution mass spectrometry showed that there are a large number of N_5VO class species coordinated porphyrins in petroleum and asphaltenes, but they are easily de-coordinated by external environment such as mass spectrometry collision voltage and other charged particles. The UV quantitation of the free demetallized porphyrins by methanesulfonic acid demetallization showed that at least 81.7% of the nickel and vanadium compounds in the Qingchuan gilsonite were in the form of petroporphyrin. The GC-NCD results showed that a large amount of amine molecules weas released with acid treatment. The second extraction with methanol of asphaltenes with acid treatment obtained a vanadium yield of about 42.3% of the first extract. Hydropyrolysis experiments showed that when the temperature is high enough, a large number of petroleum porphyrins would be released as the asphaltene

molecules coking and carbonized. Especially, porphyrin molecules with larger sizes can be well detected after hydropyrolysis. The silanization experiment results of the DMF insoluble fraction of asphaltenes proved that there are obvious hydrogen bonds between asphaltene molecules and porphyrin molecules. But hydrogen bonding is not the main driving force of aggregation. All of the experimental results showed that the so-called "non-porphyrin" should have a core structure of porphyrin compounds, which may be metalporphyrin molecules with a larger molecular weight and higher degree of condensation than conventional petroleum porphyrin compounds; it is the coordinated porphyrin unit forming with other ligands; the aggregates with the asphaltene molecule by various intermolecular forces.

Chapter 7. Study of asphaltene nanoaggregates

7.1 Introduction

Previous studies have found that the molecular weight of asphaltene molecules is not very large, mainly distributed in the range of 500-1000 Da.[127] However, due to the aggregation, the apparent molecular weight of asphaltene molecules would be tens of thousands or even hundreds of thousands, which brings great difficulties to the study of asphaltene.

The metals and sulfur (S) elements in petroleum have brought many negative effects on the petroleum refining, especially the deactivation of the catalyst.[4-5, 17] Hydrodemetalization (HDM) and hydrodesulfurization (HDS) processes can effectively remove metals and S elements from petroleum.[241] But these metals and S in the asphaltene nanoaggregates are difficult to be removed even in extremely harsh reaction conditions.

Coupling gel permeation chromatography (GPC) with inductively coupled plasma high-resolution mass spectrometry (ICP-HR-MS) has been proved to be an effective method for studying asphaltene nanoaggregates.[27, 93] The distribution of metals and sulfur in asphaltene could be divided into high-, medium-, and low-molecular-weight (HMW, MMW, and LMW) fractions, and quantitative studies could be performed for further investigation.

It was proved that the interaction between Ag^+ and the porphyrins surroundings led to a decrease in the size of the nanoaggregates and an increase in the "free" V porphyrin compounds in an atmospheric residue (AR). In this study, the asphaltene nanoaggregates were studied in detail by silver triflate reaction and GPC ICP-MS characterization. Our results showed that there is an equilibrium in the formation of asphaltene nanoaggregates. Silver ions can cut off this equilibrium and led to a shift of nanoaggregates (HMW region) to "free" asphaltene molecular (MMW and LMW region).

7.2 Experiment section

7.2.1 Reagents, samples and materials

n-heptane (C_7) was used to precipitate the asphaltenes. Tetrahydrofuran (THF), toluene (Tol) and methanol (MeOH), all HPLC-grade from Scharlau, were used for the fractionation of the asphaltenes. THF, ACS-grade multisolvent GPC, stabilized with 250 ppm butyl butylated hydroxytoluene (BHT) (Scharlau), was used for dilution and as the mobile phase for gel permeation chromatography. Spiking with silver was performed using Silver triflate (AgOTf, Sigma-Aldrich).

Asphaltene sample (AC7) was obtained by the standard method ASTM D6560-12 for precipitation of C_7 insoluble applied to Middle East atmospheric residue (AR). Another asphaltene sample (A2017) was derived

from same AR, but it was fully eluted with hot n-heptane. Elemental analysis for the atmospheric residue and its asphaltene has been described somewhere else.[242]

7.2.2 Asphaltene fractionation by extrography

Asphaltene sample, A2017, was adsorbed on silica gel with a mass loading of 1%. The dried mixture was extracted in a Soxhlet apparatus using three different solvents: acetone (100%), Hep/Tol (1:1), and Tol/THF/MeOH (10:10:1). These three fractions were named ACE, C_7T and TTM respectively. These fractions were dried under nitrogen and stored in the dark for subsequent analyses.[242]

7.2.3 GPC fractionation for AR and asphaltenes

The GPC fractionation was performed with an AKTA purifier liquid chromatography system equipped with a UV-900 multiwavelength UV absorbance detector and a Frac-950 fraction collector (GE Healthcare Bio-Sciences, Pittsburgh, U.S.A.). Three polymeric Shodex preparative GPC columns were connected in series. The mobile phase consisted of 100% ACS xylene. Preparative-scale separations were performed at a flow rate of 3 mL/min.[243]

7.2.4 HDS & HDM processes

An hydrotreatment study have been performed at pilot scale on the AR sample. A two reactors pilot have been used, allowing the sampling of intermediate effluent after the first reactor (Eff 1) and total effluent (Eff 2). As classically used in hydrotreatment of AR in fixed bed unit, reactors were loaded with large pore hydrodemetalation catalyst in the first reactor, and smaller pore transition and hydrodesulfurization catalyst in the second reactor.

7.2.5 Silver triflate reaction

The AR, asphaltenes samples and their extrography samples were diluted 50 times in THF. The preparative GPC subfractions of AR and asphaltenes were diluted 200 times in THF. Spiking with silver was performed using AgOTf (Sigma-Aldrich) with a concentration of 100 ppm.[244]

7.2.6 GPC ICP MS/UV analysis

The chromatographic system was composed of a Dionex high-performance liquid chromatography (HPLC) system with an UltiMate 3000 microflow pump, an UltiMate 3000 autosampler, a low port-to-port dead-volume microinjection valve, and an Ultimate UV system (following the 420 nm wavelength). Three GPC columns (from 1000 to 600 000 Da) connected in series were used. A Styragel guard column (4.6 mm inner diameter, 30 mm length, 10 000 Da exclusion limit) was used before the columns, and the flow rate was 1 $mL \cdot min^{-1}$ for 90 min. A splitter of 1/20 was used to send only 40 $\mu L \cdot min^{-1}$ into a double focusing sector field inductively coupled plasma mass spectrometer (Element XR, Thermo Fisher Scientific, Germany) ICP-HR-MS. Samples were analyzed as solutions prepared two days before injection to ensure that the reaction

proceeded adequately. The detailed instrument parameters and operating procedures have been described somewhere else.[244]

7.3 Results and discussion

7.3.1 Nano-aggregate and asphaltene

Figure 7.1 shows the GPC ICP MS and UV chromatograms of AR, AC7 and A2017 with and without the addition of AgOTf. In the AR sample, there was a main part of HMW region for V-containing compounds and UV signal, which indicated abundant nano-aggregates. But the proportion of HMW in S-containing compounds was small showing that on the overall the proportion of S in large aggregate is less than the proportion of V. The molecular weight of the asphaltenes fraction was more concentrated in the HMW region, as shown by the blue lines of AC7 and A2017 in Figure 7.1. The profiles of S species changed a lot and is fitting more with the V chromatogram during the phase separation of the asphaltene fraction, which suggested S species were mainly link to asphaltene nano-aggregate with HMW fraction. This part leaved under nano-aggregate from after re-dissolution of asphaltene or that S and V are in the same molecule.

When AgOTf was added, as shown by the red lines in Figure 7.1, the V species in AR and asphaltenes shifted significantly, mainly from HWM to MMW. It should be pointed out that the shift of S species in AR was not obvious due to the fact that the main proportion of S-containing compounds in an AR do not exist in the form of aggregates. This shows that the S species distributed in the MMW area, only a few asphaltene nano-aggregates. As the retention time of the appearing peak after silver addition is different between AR sample and asphaltene samples (AC7 and A2017), it seems that the disaggregation process was promoted by silver lead to smallest molecule/aggregate in the case of AR. During the asphaltene precipitation, from AR to AC7, there is an increase of HMW for both V and S compounds with precipitation of compounds present MMW, LMW and tailing fraction. In asphaltene, the aggregated part (mainly HMW) is more present than in AR. From AC7 to A2017, the washing step is not changing drastically the fraction proportion with a small increase of HMW showing that this washing is not changing the aggregation. Before and after Ag addition, the profiles of AC7 and A2017 are same. The peak of elution with Ag addition from AR to the AC7 and A2017 samples were different, peak at 26 min in AR and 23 min in asphaltene, as shown with the dash-dot-dash lines for V in Figure 7.1. The addition of Ag on AR lead to species at a higher retention time indicting smaller molecular size.

During all the study, the HMW, MMW, LMW and Tailing region percentages of profiles of ^{32}S and ^{51}V were calculated, as shown in Table 7.1. These quantitative data also showed a decrease in the percentage of HMW compounds and an increase in those of MMW and LMW compounds. It is worth noting that the tailing area were larger than LMW area for AC7 and A2017 without AgOTf, which may be caused by the interaction

between some petroleum molecules and the column phase. And the percentage of tailing region decreased with the addition of Ag ions, which indicated that Ag ions may help to eliminate this interaction.

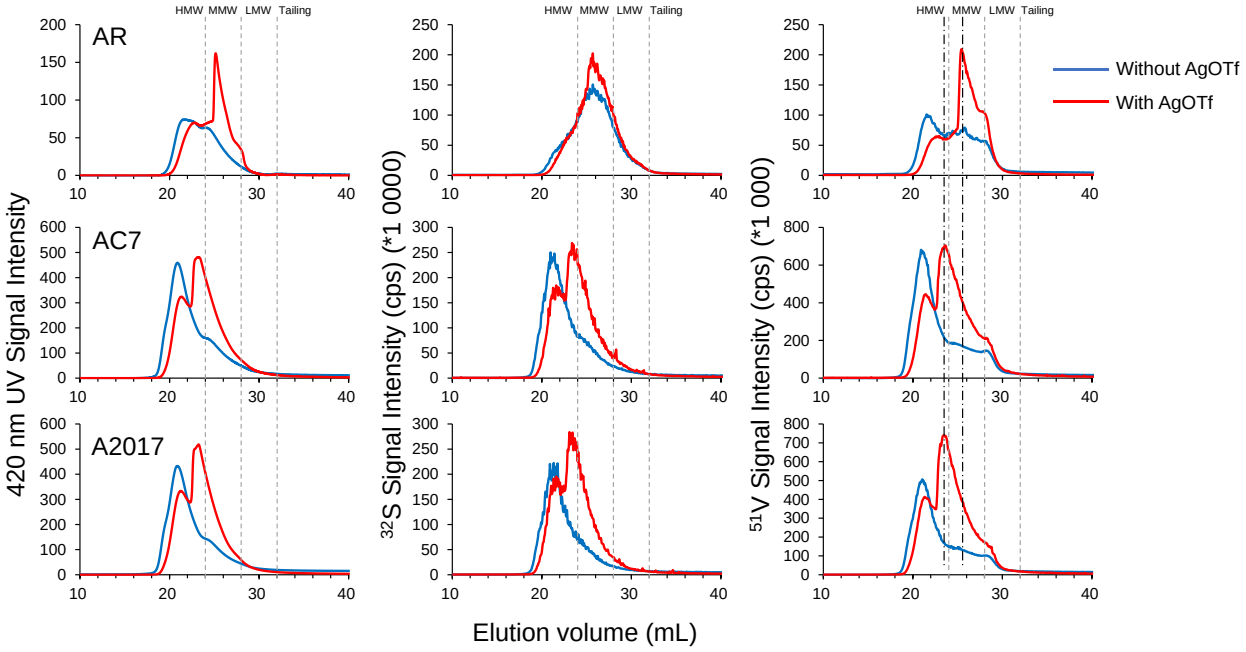

Figure 7.1 420 nm UV and ^{32}S and ^{51}V GPC ICP-HR-MS chromatograms of AR, AC7 and A2017 with and without the addition of AgOTf

Table 7.1 Molecular weight distribution of ^{32}S and ^{51}V in the chromatograms of AR, AC7 and A2017

Sample			HMW area (%)	MMW area (%)	LMW area (%)	tailing area (%)
S	AR	no AgOTf	26.4	57.0	12.8	3.8
		AgOTf	20.6	63.3	13.4	2.8
	AC7	no AgOTf	69.5	16.9	4.3	9.4
		AgOTf	59.7	31.6	5.2	3.4
	A2017	no AgOTf	69.5	14.5	3.8	12.2
		AgOTf	63.7	28.8	3.9	3.6
V	AR	no AgOTf	46.8	38.6	8.3	6.3
		AgOTf	24.4	65.7	8.8	1.1
	AC7	no AgOTf	63.0	19.6	6.3	11.2
		AgOTf	53.0	36.4	7.0	3.5
	A2017	no AgOTf	60.8	18.6	6.1	14.6
		AgOTf	55.8	34.6	5.7	3.8

7.3.2 Ag^+ reaction on asphaltene extrography fractions

When A2017 asphaltene was eluted by acetone which are dominated by the island type molecules, the only remaining metalloporphyrins and sulfur-containing molecules, which surround the asphaltene aggregates, were removed. As shown by profiles of ACE in Figure 7.2, no shift happened on the molecular weight distribution of the ACE fraction when AgOTf was added, except a small peak appearing in LMW regions. It is inferred that ACE fraction has low aggregation

For the C_7T and TTM fractions, the vast majority of asphaltene nanoaggregate molecules were in the HMW GPC domain. A part of the S and V species of HMW were shifted to the MMW and/or LMW regions after AgOTf was added. However, a considerable amount of these aggregates was stubborn and difficult to be disassociated by Ag ions. The addition of AgOTf shows that a part of S and V species can be released from the nanoaggregate; This result is in agreement with the presence of this species linked to the side chain of the nanoaggregate formed by Archipelago type molecule (TTM fraction) and by Island with side chain (C_7T fraction).[242]

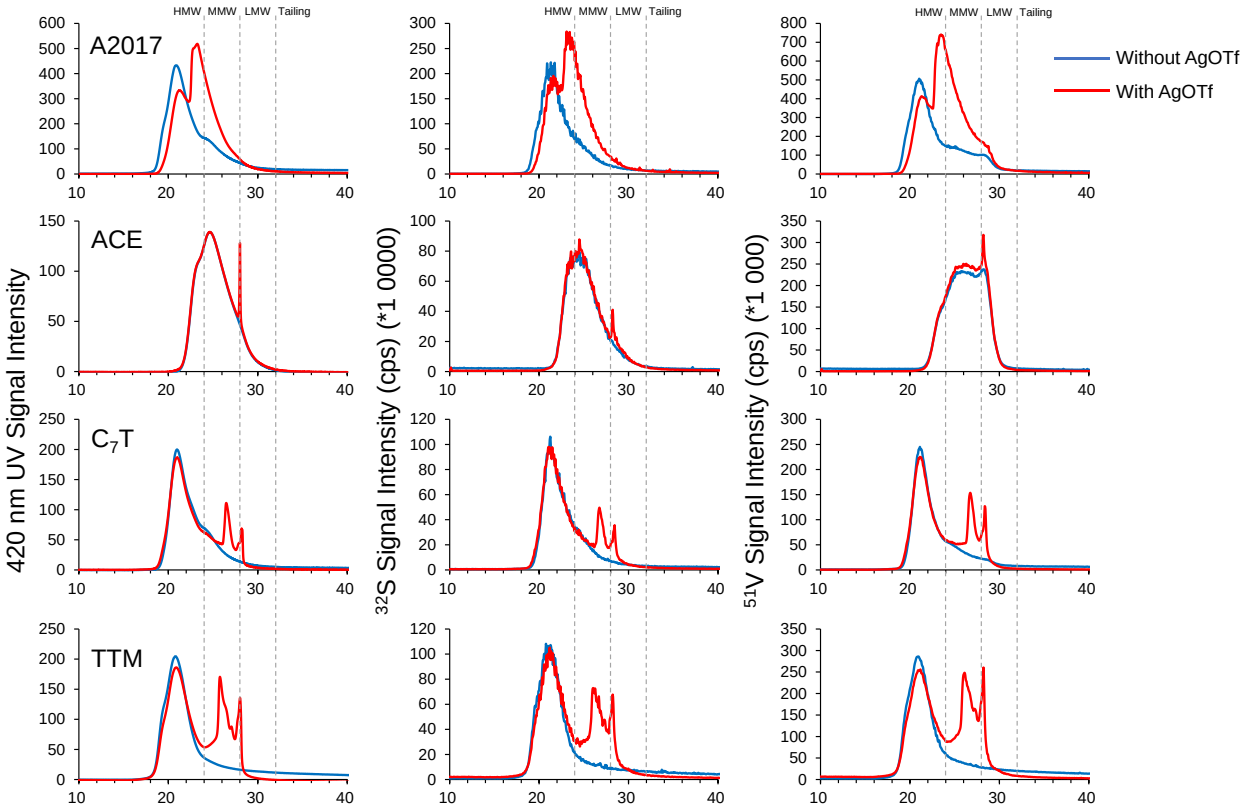

Figure 7.2 420 nm UV and ^{32}S and ^{51}V GPC ICP-HR-MS chromatograms of A2017, ACE, C_7T and TTM with and without the addition of AgOTf.

7.3.3 Ag^+ reaction on preparative GPC subfractions

To further study the mechanism of Ag ion on asphaltene aggregates, these AR and asphaltenes samples were divided into HWM, MMW, LMW and Tailing subfractions by preparative GPC. GPC profile of the sample with and without AgOTf allow to follow the molecular mass distribution modification link to Ag interaction for each subfraction.

Concerning the AR sample, Figure 7.3 shows the 420 nm UV and S and V GPC ICP-HR-MS chromatograms of size fractionation. Figure 7.4 and Figure 7.54 are these chromatograms for AC7 and A2017 size fraction's, respectively.

As previously reported,[93, 243] the reinjection of HMW, MMW, LMW and tailing fraction show that HMW fraction elute again in HMW and thus shows the stability of this nanoaggregate after evaporation and dilution for reinjection. The MMW fraction elute with a part in HMW showing a possible re-aggregation of a part of this fraction. LMW is also mainly in HMW/MMW part of the chromatogram but with some re-aggregation that was more present in asphaltene than in AR samples, which could be clearly seen by the molecular weight distribution of LMW subfraction re-injection in Table 7.2. Tailing fraction is eluting after the permeation volume to the GPC column, so, this fraction, is corresponding to compounds or nanoaggregate that have an interaction with the phase of the GPC column. After evaporation and re-injection of this fraction, main compounds are now eluting in HMW, MMW and LMW part of the chromatogram, showing that these compounds can form some nanoaggregate that have less interaction with the column and thus elute before. Addition of Ag on this fraction is leading to a small de-aggregation that produce an intense peak at 28 min.

Table 7.2 Molecular weight distribution of ^{51}V in the chromatograms of re-injection for LMW subfractions of AR, AC7 and A2017

Sample		HMW area (%)	MMW area (%)	LMW area (%)	tailing area (%)
AR	no AgOTf	21.3	46.6	23.3	8.8
	AgOTf	10.5	63.8	21.8	3.8
AC7	no AgOTf	26.8	40.8	22.9	9.4
	AgOTf	11.3	66.2	20.8	1.8
A2017	no AgOTf	33.1	36.1	17.1	13.7
	AgOTf	13.7	70.5	13.9	2.0

For the GPC subfractions of AR, the modification of Ag ions was less important compare to Asphaltenes samples. The main effect appears to be on HMW fraction, the disappearance of the highest part to the benefit of LMW part. This is clearly shows a de-aggregation of some surrounding compounds of nanoaggregate as previously reported by *Moulian et al*. The MMW and LMW fraction present slightly no difference for the S chromatogram between Ag addition of not, showing that these fractions are stable. Concerning UV and V of

the HMW part of the profile, with Ag addition, is moving to LMW, demonstrating that this part should be due to a re-aggregation process and not to some stable nanoaggregate in solution. On Tailing fraction, the effect of Ag is also showing a de-aggregation of HMW part to LMW part. This small change on the AR subfraction, are, to our point of view, link to the fact that in AR the HMW nanoaggregate are the one "naturally" present in the crude oil since its origin and are thus difficult to disaggregate. These "original nanoaggregates" may be extremely complex due to the entanglement of chain link molecules.

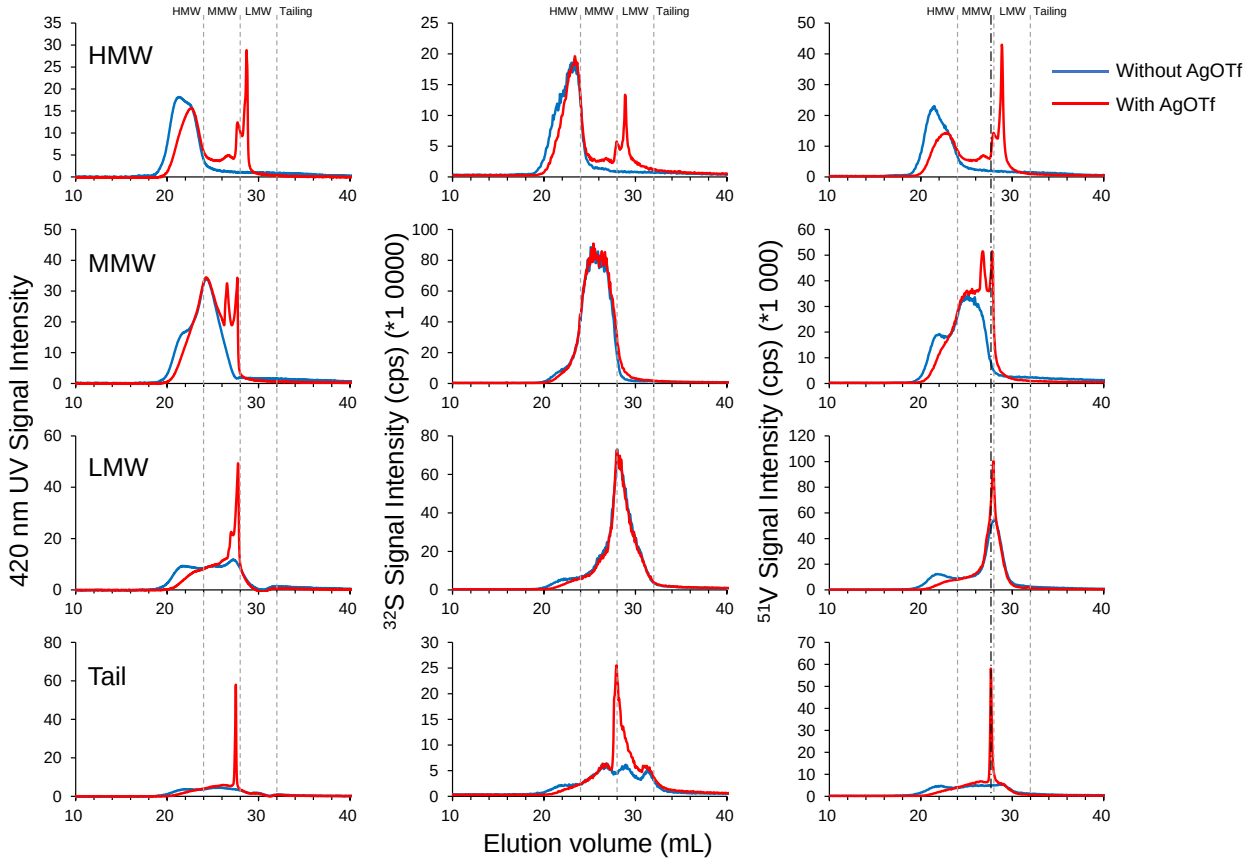

Figure 7.3 420 nm UV and ^{32}S and ^{51}V GPC ICP-HR-MS chromatograms of preparative GPC fractions of the AR with and without the addition of AgOTf

However, the modification induced by Ag on the GPC subfractions of AC7 and A2017 were stronger. Each profile of these subfractions has a significant shift from HMW to MMW and/or LMW. This indicated that the Ag has a poor modification on the original nanoaggregates that exist in AR, but for the secondary nanoaggregates formed during asphaltene precipitation. Ag exhibits an effective disaggregation function of this "non" original nanoaggregate. In other words, Ag is cutting the reaggregation that occur during asphaltene precipitation.

The aggregation promoted during asphaltene precipitation should be an equilibrium process. An equilibrium between HMW with MMW and/or LMW. When AgOTf was added to the asphaltene, the equilibrium was shifted to lower molecular weights. Each Preparative GPC fraction would reach the aggregation equilibrium again, forming a considerable amount of HMW (bimodal profile on MMW and LMW blue chromatogram of figure 7.4). The addition of Ag cut this equilibrium, made a large part of HMW turn into MMW and LMW.

Compared with Asphaltene, the aggregation in AR was not so obvious. This is because the dispersion of maltene. However, when the asphaltenes precipitated, the equilibrium would shift, a large amount of HMW produced and reached the equilibrium of HMW. But the addition of Ag ions shift this equilibrium.

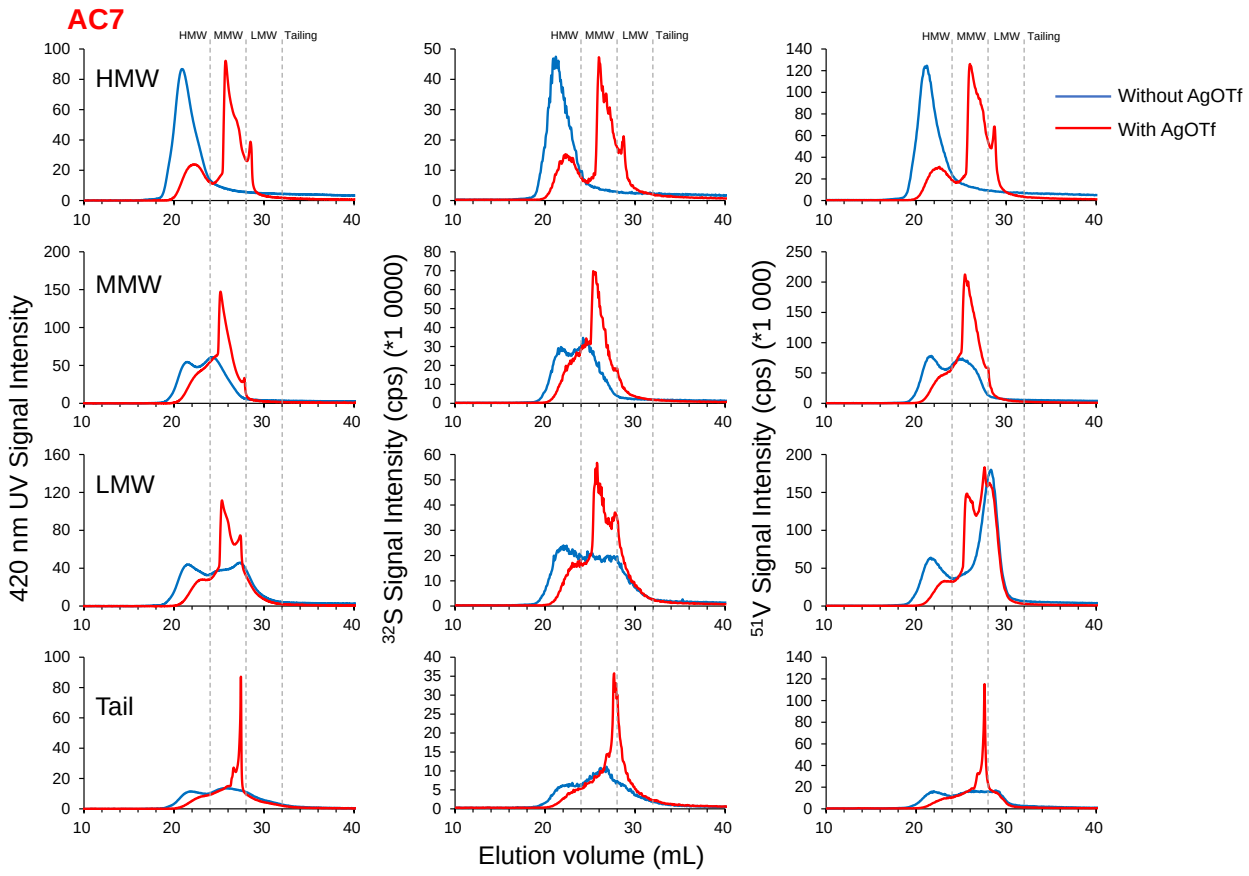

Figure 7.4 420 nm UV and ^{32}S and ^{51}V GPC ICP-HR-MS chromatograms of preparative GPC fractions of AC7 with and without the addition of AgOTf

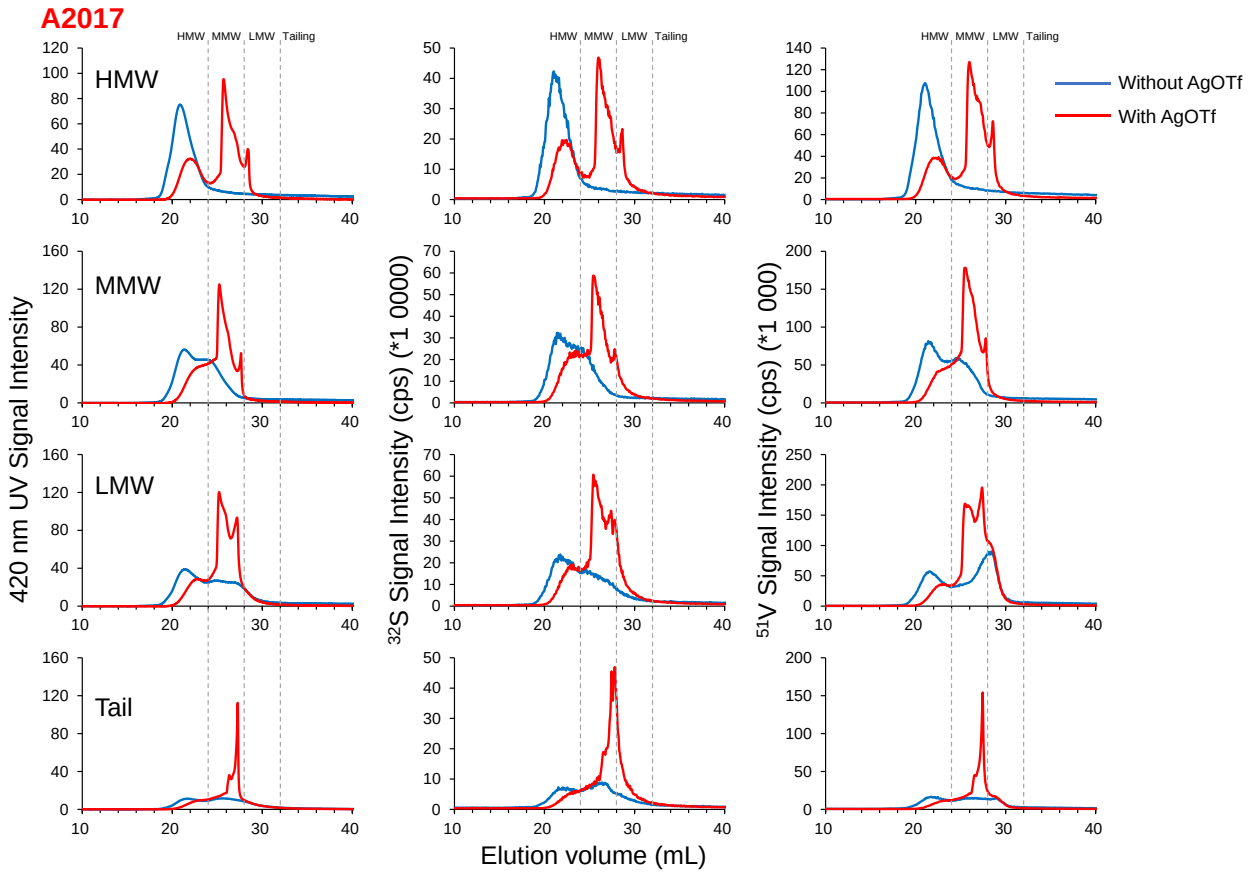

Figure 7.5 420 nm UV and ^{32}S and ^{51}V GPC ICP-HR-MS chromatograms of preparative GPC fractions of A2017 with and without the addition of AgOTf

7.3.4 Ag^+ reaction link to hydrotreatment

Sulfur and metal elements in AR can be effectively removed by hydrotreatment. As shown in Figure 7.6 and 7.7, the abundance of S and V species decreased in Eff 1, and the content of these elements were much lower in Eff 2 with a more severe reaction. The specific area and the decrease of the area from AR to Eff 1 and Eff 2 are shown in Table 7.3. However, there was no change of the molecular weight distribution of S species before and after hydrotreatment, which were mainly distributed in the MMW region. Moreover, no obvious change happened on the profiles with the addition of AgOTf.

Concerning the UV and V chromatograms, we can see, as already reported,[91, 241] species in the MMW and LMW regions were first removed in hydrotreatment. In Eff 1 and Eff 2, the vast majority of V species existed in the HMW region. Although the proportion of V species in the MMW and LMW regions increased with the addition of AgOTf, the content of V species in HMW region was still considerable. Therefore, it is difficult for Ag to disaggregate the asphaltene nano-aggregates completely after hydrotreatment. The change of the profiles for V indicated that the mechanism of the Ag ion on the metal-containing aggregates is different from that of the hydrotreatment.

Concerning the MMW and LMW V-containing compounds that appearing after Ag addition in AR, Eff 1 and Eff 2 samples, they are at successively longer retention times but all linked to decrease in size of the HMW part (Figure 7.6). Also, the species that are released are different from AR, Eff 1 and Eff 2 (V red chromatograms in Figure 7.6 and UV chromatograms in figure 7.7). It's seems that Ag is de-aggregating the same V species that will lead to Eff 1 chromatogram and then to Eff 2 chromatogram. Each time a skin around the main central nanoaggregate is removed by hydrotreatment or Ag, firstly some larger V species (that appearing with Ag in the HMW region) and then some smaller species (appearing in MMW/LMW on Eff 1 and Eff 2 V chromatogram after Ag addition).

Table 7.3 The area of sulfur and vanadium chromatograms of AR to Eff 1 and Eff 2 and the decrease of the area from AR to Eff 1 and Eff 2

	Sample	AR	Eff 1	Eff 2
S	Total area	12 924 640	7 027 570	2 225 840
	Decrease (%)	-	45.6	82.8
V	Total area	622 090	257 000	70 060
	Decrease (%)	-	58.7	88.7

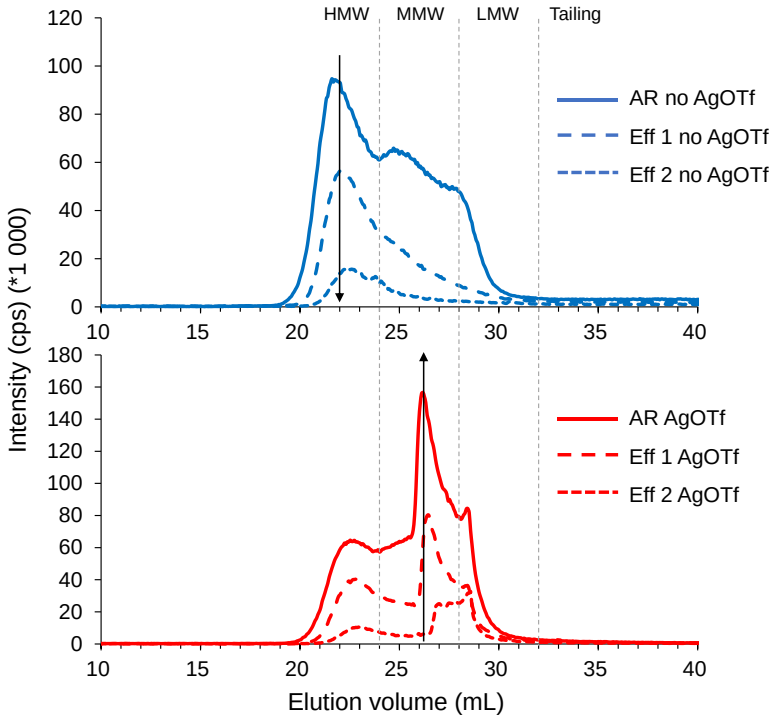

Figure 7.6 Graphs of AR Eff1 Eff2 with and without Ag for V

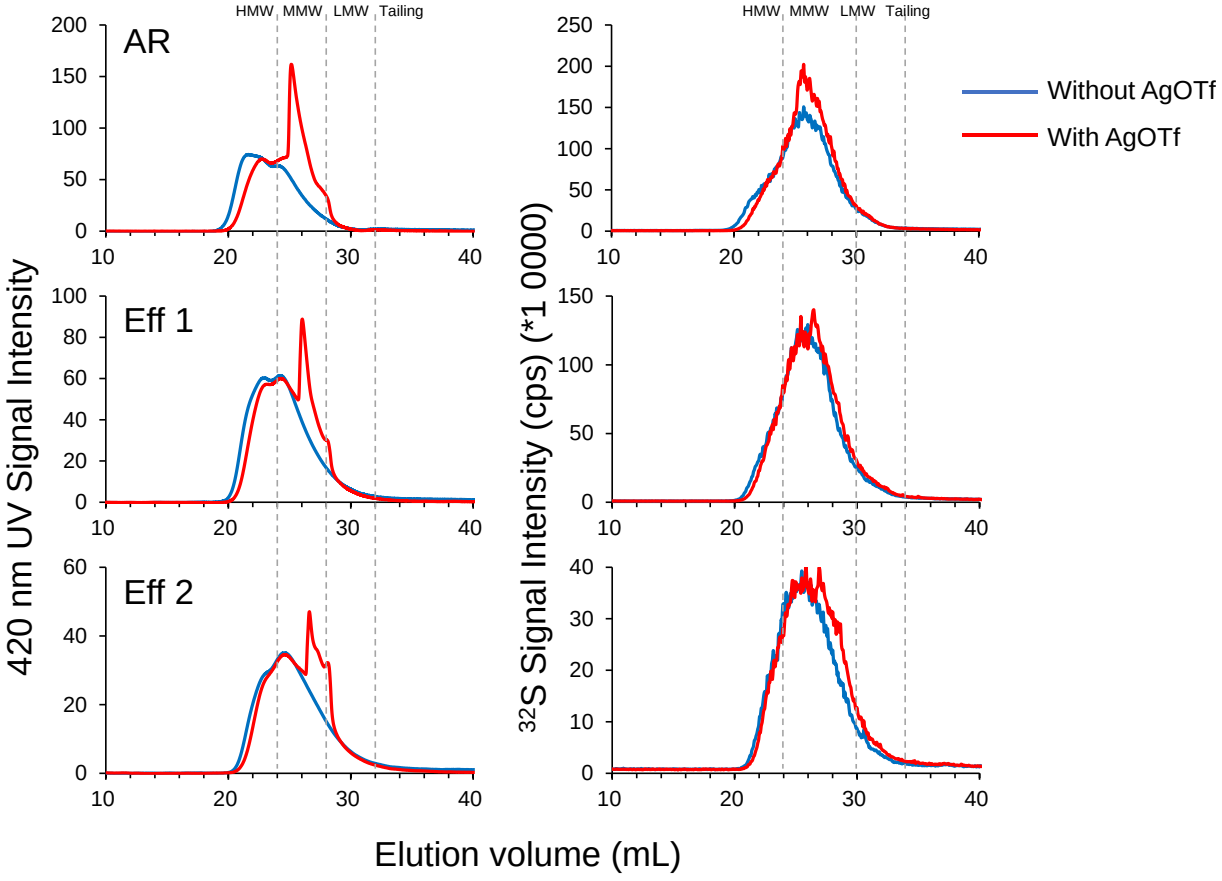

Figure 7.7 Graphs of AR Eff1 Eff2 with and without Ag for UV and S

7.4 Conclusions

This chapter proved the molecule aggregation in asphaltene is an equilibrium process. In petroleum samples, AR or asphaltenes, the aggregation equilibrium would move and form a new one during fractionation or asphaltene precipitation. Ag ion can cut off this equilibrium. The addition of Ag made the equilibrium turned into lower molecular weights, showing a significant shift from HMW to MMW and/or LMW. However, Ag ion is powerless for the "original nanoaggregates" with side chain entanglement, which may be the essential core of asphaltene aggregates. Ag ions also have a substantial disaggregation effect on the metal-containing aggregates in the hydrotreated product.

Concluding remarks

This thesis took Canadian oilsands bitumen, Venezuelan heavy oil asphaltenes, Qingchuan gilsonite, Texas immature marine shales and Middle East AR and asphaltenes as the research objects. A variety of analysis methods and chemical derivatization methods were used, such as acid treatment, hydropyrolysis, methanesulfonic acid demetalization, silanization and AgOTf reaction, to process the asphaltenes and to definite the existence of metal compounds inside. Focused on the metal compounds in asphaltenes to fully confirm their existing forms, and to provide partial information of the asphaltene composition. Summarized as follows:

The mass ranges of mass spectra and DBE value of polar heteroatom species in Canadian oilsands bitumen increased as the SFEF fraction became heavier. The distributions of various class species were shifted as the SFEF fraction became heavier. The abundance of vanadyl porphyrins increased dramatically in heavy fractions, and accounted for 98% in the end-cut.

Gallium porphyrins were identified in petroleum samples for the first time. Three new types of oxygen-containing iron porphyrins corresponding to $C_nH_mN_4FeO$, $C_nH_mN_4FeO_2$ and $C_nH_mN_5FeO_2$ were also identified.The finding of gallium porphyrins and oxygen-containing porphyrins could provide new insights on the diagenetic pathway and the evolution of petroporphyrins, which may have important implications to decipher the development of Oceanic Anoxic Event 2.

The molecular composition of Qingchuan gilsonite has been characterized in detail by various techniques, which provide reference information for the existence of metalloporphyrins in natural asphalt. The molecular composition of vanadyl porphyrins indicated the maturity of the gilsonite is very low. Considering the huge reserves and high metal content, Qingchuan gilsonite should has important utilization value.

The characterization of vanadyl porphyrins from the heavy crude oil showed that part of vanadyl porphyrins in petroleum exist as aggregated molecules, but they are easily de-coordinated by external environment such as mass spectrometry collision voltage and other charged particles. These aggregates of porphyrins will absence when other charged particles intervene, such as ionization promoter. The application of the combination of IMS with Q-q-TOF MS reveals the ionization, aggregation and fragmentation status of porphyrin ions in ion produce and transfer.

Several experiments were designed to find the trail of "non-porphyrin", and explore the existence of metal compounds in asphaltenes. All of the experimental results showed that the so-called "non-porphyrin" should have a core structure of porphyrin compounds, which may be metalporphyrin molecules with a larger molecular weight and higher degree of condensation than conventional petroleum porphyrin compounds; it is the coordinated porphyrin unit forming with other ligands; the aggregates with the asphaltene molecule by various intermolecular forces. The aggregation causes the porphyrin compounds in the asphaltenes to form

an apparent macromolecular structure, which is difficult to be separated, difficult to ionize, difficult to vaporize, and ultraviolet characteristic absorption is weakened or even disappeared. The molecule aggregation in asphaltene is an equilibrium process that can be cut off by externally charged particles.

Based on the results of this thesis, the existence of nickel and vanadium compounds in asphaltenes is clarified, which can be divided into three forms: the first one is free porphyrin molecules, which can be extracted, separated and detected directly; the second one is the porphyrin molecules around the asphaltene aggregates. Compared with the first one, their molecular weight is larger, the DBE is also higher, and there is a certain force between the asphaltene aggregates and porphyrins; the third one is the porphyrin inside the asphaltene aggregates. It is an important part of the asphaltene aggregate, which is difficult to separate and detect. A more vivid description of the existence of porphyrins in asphaltenes is shown in Figure 8.1.

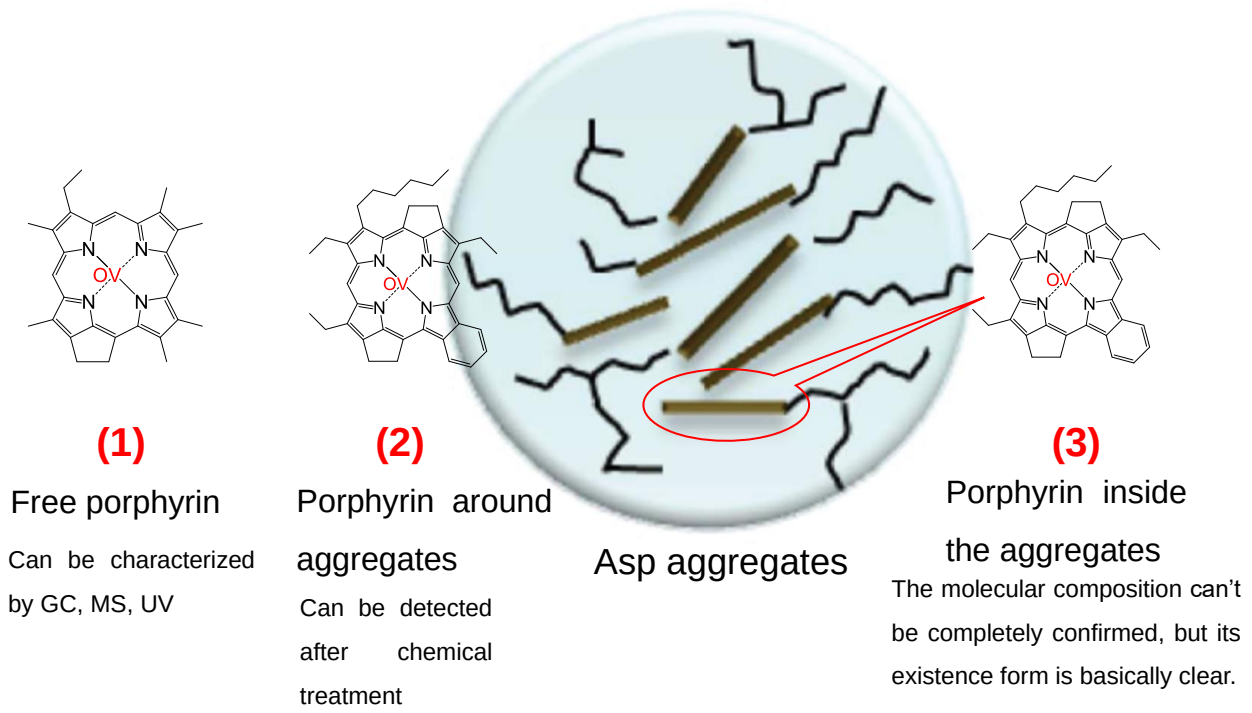

Figure 8.1 Schematic diagram of porphyrins in asphaltene

References

1. Chilingarian, G. V.; Yen, T. F., *Bitumens, asphalts, and tar sands*. Elsevier: 1978.
2. E, H.; Watkinson, P., A study of asphaltene solubility and precipitation. *Fuel* **2004,** *83* (14), 1881-1887.
3. Enayat, S.; Rajan Babu, N.; Kuang, J.; Rezaee, S.; Lu, H.; Tavakkoli, M.; Wang, J.; Vargas, F. M., On the development of experimental methods to determine the rates of asphaltene precipitation, aggregation, and deposition. *Fuel* **2020,** *260*, 116250.
4. Nascimento, P. T. H.; Santos, A. F.; Yamamoto, C. I.; Tose, L. V.; Barros, E. V.; Gonçalves, G. R.; Freitas, J. C. C.; Vaz, B. G.; Romão, W.; Scheer, A. P., Fractionation of Asphaltene by Adsorption onto Silica and Chemical Characterization by Atmospheric Pressure Photoionization Fourier Transform Ion Cyclotron Resonance Mass Spectrometry, Fourier Transform Infrared Spectroscopy Coupled to Attenuated Total Reflectance, and Proton Nuclear Magnetic Resonance. *Energy & Fuels* **2016,** *30* (7), 5439-5448.
5. Speight, J. G., Petroleum Asphaltenes - Part 2: the Effect of Asphaltene and Resin Constituents on Recovery and Refining Processes. *Oil & Gas Science and Technology* **2004,** *59* (5), 479-488.
6. Akbarzadeh, K.; Hammami, A.; Kharrat, A.; Zhang, D.; Allenson, S.; Creek, J.; Kabir, S.; Jamaluddin, A.; Marshall, A. G.; Rodgers, R. P., Asphaltenes—problematic but rich in potential. *Oilfield Review* **2007,** *19* (2), 22-43.
7. Ribeiro, F. S.; Souza Mendes, P. R.; Braga, S. L., Obstruction of pipelines due to paraffin deposition during the flow of crude oils. *Int. J. Heat Mass Transfer* **1997,** *40* (18), 4319-4328.
8. Wen, C. S.; Chilingarian, G.; Yen, T. F., Properties and structure of bitumens. *Bitumens, asphalts and tar sands* **1978,** *7*, 155.
9. Speight, J. G., Petroleum Asphaltenes - Part 1: Asphaltenes, Resins and the Structure of Petroleum. *Oil & Gas Science and Technology* **2004,** *59* (5), 467-477.
10. Mullins, O. C.; Sheu, E. Y., *Structures and dynamics of asphaltenes*. Springer Science & Business Media: 2013.
11. Badre, S.; Carla Goncalves, C.; Norinaga, K.; Gustavson, G.; Mullins, O. C., Molecular size and weight of asphaltene and asphaltene solubility fractions from coals, crude oils and bitumen. *Fuel* **2006,** *85* (1), 1-11.
12. Mullins, O. C.; Sheu, E. Y.; Hammami, A.; Marshall, A. G., *Asphaltenes, heavy oils, and petroleomics*. Springer Science & Business Media: 2007.
13. Simanzhenkov, V.; Idem, R., *Crude oil chemistry*. Crc Press: 2003.
14. Sheu, E. Y.; Mullins, O. C., *Fundamentals and applications*. Springer: 1995.
15. Yen, T. F.; Chilingarian, G. V., *Asphaltenes and asphalts, 2*. Elsevier: 2000.
16. Dechaine, G. P.; Gray, M. R., Chemistry and Association of Vanadium Compounds in Heavy Oil and Bitumen, and Implications for Their Selective Removal. *Energy & Fuels* **2010,** *24* (5), 2795-2808.
17. Ok, S.; Mal, T. K., NMR Spectroscopy Analysis of Asphaltenes. *Energy & Fuels* **2019,** *33* (11), 10391-10414.
18. Vargas, F. M.; Tavakkoli, M., *Asphaltene deposition: Fundamentals, prediction, prevention, and remediation*. CRC Press: 2018.
19. Bunger, J. W.; Li, N. C., *Chemistry of asphaltenes*. American Chemical Society: 1981.
20. Czogalla, C.-D.; Boberg, F., Sulfur Compounds in Fossil Fuels I. *Sulfur Reports* **1983,** *3* (4), 121-161.
21. George, G. N.; Gorbaty, M. L., Sulfur K-edge x-ray absorption spectroscopy of petroleum asphaltenes and model compounds. *J. Am. Chem. Soc.* **1989,** *111* (9), 3182-3186.
22. Waldo, G. S.; Mullins, O. C.; Penner-Hahn, J. E.; Cramer, S. P., Determination of the chemical environment of sulphur in petroleum asphaltenes by X-ray absorption spectroscopy. *Fuel* **1992,** *71* (1), 53-57.
23. Bava, Y. B.; Geronés, M.; Giovanetti, L. J.; Andrini, L.; Erben, M. F., Speciation of sulphur in asphaltenes and resins from Argentinian petroleum by using XANES spectroscopy. *Fuel* **2019,** *256*, 115952.
24. Zhang, L.-l.; Wang, C.-l.; Zhao, Y.-s.; Yang, G.-h.; Su, M.; Yang, C.-h., Speciation and quantification of sulfur compounds in petroleum asphaltenes by derivative XANES spectra. *Journal of Fuel Chemistry and Technology* **2013,** *41* (11), 1328-1335.
25. Vargas, V.; Castillo, J.; Ocampo Torres, R.; Bouyssiere, B.; Lienemann, C.-P., Development of a chromatographic methodology for the separation and quantification of V, Ni and S compounds in petroleum products. *Fuel Process. Technol.* **2017,** *162*, 37-44.
26. Gascon, G.; Vargas, V.; Feo, L.; Castellano, O.; Castillo, J.; Giusti, P.; Acavedo, S.; Lienemann, C.-P.; Bouyssiere, B., Size Distributions of Sulfur, Vanadium, and Nickel Compounds in Crude Oils, Residues,

and Their Saturate, Aromatic, Resin, and Asphaltene Fractions Determined by Gel Permeation Chromatography Inductively Coupled Plasma High-Resolution Mass Spectrometry. *Energy & Fuels* **2017,** *31* (8), 7783-7788.
27. Gascon, G.; Negrín, J.; Montoto, V. G.; Acevedo, S.; Lienemann, C.-P.; Bouyssiere, B., Simplification of Heavy Matrices by Liquid–Solid Extraction: Part II—How to Separate the LMW, MMW, and HMW Compounds in Asphaltene Fractions for V, Ni, and S Compounds. *Energy & Fuels* **2019,** *33* (9), 8110-8117.
28. Wang, S.; Yang, C.; Xu, C.; Zhao, S.; Shi, Q., Separation and characterization of petroleum asphaltene fractions by ESI FT-ICR MS and UV-vis spectrometer. *Science China Chemistry* **2013,** *56*, 856-862.
29. Wang, L.; He, C.; Liu, Y.; Zhao, S.; Zhang, Y.; Xu, C.; Chung, K.; Shi, Q., Effects of experimental conditions on the molecular composition of maltenes and asphaltenes derived from oilsands bitumen: Characterized by negative-ion ESI FT-ICR MS. *Science China Chemistry* **2013,** *56*, 863-873.
30. Cho, Y.; Na, J.-G.; Nho, N.-S.; Kim, S.; Kim, S., Application of Saturates, Aromatics, Resins, and Asphaltenes Crude Oil Fractionation for Detailed Chemical Characterization of Heavy Crude Oils by Fourier Transform Ion Cyclotron Resonance Mass Spectrometry Equipped with Atmospheric Pressure Photoionization. *Energy & Fuels* **2012,** *26* (5), 2558-2565.
31. Qian, K.; Mennito, A. S.; Edwards, K. E.; Ferrughelli, D. T., Observation of vanadyl porphyrins and sulfur-containing vanadyl porphyrins in a petroleum asphaltene by atmospheric pressure photonionization Fourier transform ion cyclotron resonance mass spectrometry. *Rapid Commun. Mass Spectrom.* **2008,** *22* (14), 2153-2160.
32. Qian, K.; Rodgers, R. P.; Hendrickson, C. L.; Emmett, M. R.; Marshall, A. G., Reading Chemical Fine Print: Resolution and Identification of 3000 Nitrogen-Containing Aromatic Compounds from a Single Electrospray Ionization Fourier Transform Ion Cyclotron Resonance Mass Spectrum of Heavy Petroleum Crude Oil. *Energy & Fuels* **2001,** *15* (2), 492-498.
33. Shi, Q.; Hou, D.; Chung, K. H.; Xu, C.; Zhao, S.; Zhang, Y., Characterization of Heteroatom Compounds in a Crude Oil and Its Saturates, Aromatics, Resins, and Asphaltenes (SARA) and Non-basic Nitrogen Fractions Analyzed by Negative-Ion Electrospray Ionization Fourier Transform Ion Cyclotron Resonance Mass Spectrometry. *Energy & Fuels* **2010,** *24* (4), 2545-2553.
34. Ignasiak, T.; Strausz, O. P.; Montgomery, D. S., Oxygen distribution and hydrogen bonding in Athabasca asphaltene. *Fuel* **1977,** *56* (4), 359-365.
35. Zheng, C.; Brunner, M.; Li, H.; Zhang, D.; Atkin, R., Dissolution and suspension of asphaltenes with ionic liquids. *Fuel* **2019,** *238*, 129-138.
36. Moschopedis, S. E.; Speight, J. G., Oxygen functions in asphaltenes. *Fuel* **1976,** *55* (4), 334-336.
37. Chacón-Patiño, M. L.; Smith, D. F.; Hendrickson, C. L.; Marshall, A. G.; Rodgers, R. P., Advances in Asphaltene Petroleomics. Part 4. Compositional Trends of Solubility Subfractions Reveal that Polyfunctional Oxygen-Containing Compounds Drive Asphaltene Chemistry. *Energy & Fuels* **2020,** *34* (3), 3013-3030.
38. Liang, W., *Petroleum Chemistry, 2nd ed.* China University of Petroleum Press: 2009.
39. Elliot, J. D., Delayed Coker design and operation: recent trends and innovations. *Foster Wheeler USA Corporation* **1996**.
40. Guidroz, J. M.; Sneddon, J., Fate of vanadium determined by nitrous oxide–acetylene flame atomic absorption spectrometry in unburned and burned Venezuelan crude oil. *Microchem. J.* **2002,** *73* (3), 363-366.
41. Aucélio, R. Q.; Doyle, A.; Pizzorno, B. S.; Tristão, M. L. B.; Campos, R. C., Electrothermal atomic absorption spectrometric method for the determination of vanadium in diesel and asphaltene prepared as detergentless microemulsions. *Microchem. J.* **2004,** *78* (1), 21-26.
42. de Souza, R. M.; Meliande, A. L. S.; da Silveira, C. L. P.; Aucélio, R. Q., Determination of Mo, Zn, Cd, Ti, Ni, V, Fe, Mn, Cr and Co in crude oil using inductively coupled plasma optical emission spectrometry and sample introduction as detergentless microemulsions. *Microchem. J.* **2006,** *82* (2), 137-141.
43. Duyck, C.; Miekeley, N.; Porto da Silveira, C. L.; Szatmari, P., Trace element determination in crude oil and its fractions by inductively coupled plasma mass spectrometry using ultrasonic nebulization of toluene solutions. *Spectrochimica Acta Part B: Atomic Spectroscopy* **2002,** *57* (12), 1979-1990.
44. Iwasaki, K.; Tanaka, K., Preconcentration and x-ray fluorescence: Determination of vanadium, nickel and iron in residual fuel oils and in particulate material from oil-fired sources. *Anal. Chim. Acta* **1982,** *136*, 293-299.

45. Mastoi, G. M.; Khuhawar, M. Y.; Bozdar, R. B., Spectrophotometric determination of vanadium in crude oil. *J. Quant. Spectrosc. Radiat. Transfer* **2006,** *102* (2), 236-240.
46. Khuhawar, M. Y.; Arain, G. M., Liquid chromatographic determination of vanadium in petroleum oils and mineral ore samples using 2-acetylpyridne-4-phenyl-3-thiosemicarbazone as derivatizing reagent. *Talanta* **2006,** *68* (3), 535-541.
47. López, L.; Lo Mónaco, S., Geochemical implications of trace elements and sulfur in the saturate, aromatic and resin fractions of crude oil from the Mara and Mara Oeste fields, Venezuela. *Fuel* **2004,** *83* (3), 365-374.
48. Yen, T. F., *Role of trace metals in petroleum*. Ann Arbor Science Publishers,Ann Arbor, MI: United States, 1975.
49. Park, J.-I.; Al-Mutairi, A.; Marafie, A. M. J.; Yoon, S.-H.; Mochida, I.; Ma, X., The characterization of metal complexes in typical Kuwait atmospheric residues using both GPC coupled with ICP–MS and HT GC–AED. *Journal of Industrial and Engineering Chemistry* **2016,** *34*, 204-212.
50. Kotlyar, L. S.; Ripmeester, J. A.; Sparks, B. D.; Woods, J., Comparative study of organic matter derived from Utah and Athabasca oil sands. *Fuel* **1988,** *67* (11), 1529-1535.
51. Yakubov, M. R.; Sinyashin, K. O.; Abilova, G. R.; Tazeeva, E. G.; Milordov, D. V.; Yakubova, S. G.; Borisov, D. N.; Gryaznov, P. I.; Mironov, N. A.; Borisova, Y. Y., Differentiation of heavy oils according to the vanadium and nickel content in asphaltenes and resins. *Petroleum Chemistry* **2017,** *57* (10), 849-854.
52. Zheng, F.; Zhu, G.; Chen, Z.; Zhao, Q.; Shi, Q., Molecular composition of vanadyl porphyrins in the gilsonite. *Journal of Fuel Chemistry and Technology* **2020,** *48* (5), 562-567.
53. Zheng, F.; Hsu, C. S.; Zhang, Y.; Sun, Y.; Wu, Y.; Lu, H.; Sun, X.; Shi, Q., Simultaneous Detection of Vanadyl, Nickel, Iron, and Gallium Porphyrins in Marine Shales from the Eagle Ford Formation, South Texas. *Energy & Fuels* **2018,** *32* (10), 10382-10390.
54. Xu, Z.; Yu, L.; Xu, C.; Yan, Y.; Zhang, Y.; Zhang, Q.; Zhao, S.; Chung, K.; Gray, M. R.; Quan, S., Separation and Characterization of Vanadyl Porphyrins in Venezuela Orinoco Heavy Crude Oil. *Energy & Fuels* **2013,** *27* (6), 2874-2882.
55. Treibs, A., Chlorophyll- und Häminderivate in bituminösen Gesteinen, Erdölen, Erdwachsen und Asphalten. Ein Beitrag zur Entstehung des Erdöls. *Justus Liebigs Annalen Der Chemie* **1934,** *510* (1), 42-62.
56. Treibs, A., Chlorophyll- und Häminderivate in organischen Mineralstoffen. *Angew. Chem.* **1936,** *49* (38), 682-686.
57. Baker, E. W.; Yen, T. F.; Dickie, J. P.; Rhodes, R. E.; Clark, L. F., Mass spectrometry of porphyrins. II. Characterization of petroporphyrins. *J. Am. Chem. Soc.* **1967,** *89* (14), 3631-3639.
58. Quirke, J. M. E., Mass spectrometry of porphyrins and metalloporphyrins. *The porphyrin handbook* **2000,** *7*, 371-422.
59. Rodgers, R. P.; Hendrickson, C. L.; Emmett, M. R.; Marshall, A. G.; Greaney, M.; Qian, K., Molecular characterization of petroporphyrins in crude oil by electrospray ionization Fourier transform ion cyclotron resonance mass spectrometry. *Canadian Journal of Chemistry* **2001,** *79* (5-6), 546-551.
60. Xu, H.; Yu, D.; Que, G., Characterization of petroporphyrins in Gudao residue by ultraviolet–visible spectrophotometry and laser desorption ionization-time of flight mass spectrometry. *Fuel* **2005,** *84* (6), 647-652.
61. Dunning, H. N.; Moore, J. W., Porphyrin research and origin of petroleum. *AAPG Bulletin* **1957,** *41* (11), 2403-2412.
62. Bonnett, R.; Burke, P. J., Iron porphyrins in coal from the United States. *Geochim. Cosmochim. Acta* **1985,** *49* (6), 1487-1489.
63. Bonnett, R.; Burke, P. J.; Reszka, A., Metalloporphyrins in coal : 2. Iron porphyrins. *Fuel* **1987,** *66* (4), 515-520.
64. Treibs, A., Chlorophyll- und Hämin-Derivate in bituminösen Gesteinen, Erdölen, Kohlen, Phosphoriten. *Justus Liebigs Annalen Der Chemie* **1935,** *517*.
65. McKenna, A. M.; Purcell, J. M.; Rodgers, R. P.; Marshall, A. G., Identification of Vanadyl Porphyrins, in a Heavy Crude Oil and Raw Asphaltene by Atmospheric Pressure Photoionization Fourier Transform Ion Cyclotron Resonance (FT-ICR) Mass Spectrometry. *Energy & Fuels* **2009,** *23* (3-4), 2122-2128.
66. Wang, X.; Lang, R.; Qi, L., Petroporphyrins in Gaosheng crude oil. *Geochemistry* **1983,** *2* (3), 251-260.
67. Liao, Z.; Huang, D.; Shi, J., Discovery of Special Predominance of Vanadyl Porphyrin and High Abundance of Di-DPEP in Nonmarine Strata. *Science China - Chemistry* **1990,** *33* (5), 631-640.

68. Grigsby, R.; Green, J., High-resolution mass spectrometric analysis of a vanadyl porphyrin fraction isolated from the> 700 C resid of Cerro Negro heavy petroleum. *Energy & fuels* **1997,** *11* (3), 602-609.
69. Gallegos, E. J.; Sundararaman, P., Mass spectrometry of geoporphyrins. *Mass Spectrom. Rev.* **1985,** *4* (1), 55-85.
70. Hajibrahim, S.; Quirke, J.; Eglinton, G., Petroporphyrins: V. Structurally-related porphyrin series in bitumens, shales and petroleums—Evidence from HPLC and mass spectrometry. *Chem. Geol.* **1981,** *32* (1-4), 173-188.
71. Barrow, M. P.; McDonnell, L. A.; Feng, X. D.; Walker, J.; Derrick, P. J., Determination of the nature of naphthenic acids present in crude oils using nanospray Fourier transform ion cyclotron resonance mass spectrometry: The continued battle against corrosion. *Anal. Chem.* **2003,** *75* (4), 860-866.
72. Schaub, T. M.; Hendrickson, C. L.; Quinn, J. P.; Rodgers, R. P.; Marshall, A. G., Instrumentation and method for ultrahigh resolution field desorption ionization Fourier transform ion cyclotron resonance mass spectrometry of nonpolar species. *Anal. Chem.* **2005,** *77* (5), 1317-1324.
73. Rodgers, R. P.; Marshall, A. G., *Petroleomics: Advanced Characterization of Petroleum-Derived Materials by Fourier Transform Ion Cyclotron Resonance Mass Spectrometry (FT-ICR MS)*. Springer New York: 2007; p 63-93.
74. Putman, J. C.; Rowland, S. M.; Corilo, Y. E.; McKenna, A. M., Chromatographic enrichment and subsequent separation of nickel and vanadyl porphyrins from natural seeps and molecular characterization by positive electrospray ionization FT-ICR mass spectrometry. *Anal. Chem.* **2014,** *86* (21), 10708-10715.
75. Qian, K.; Edwards, K. E.; Diehl, J. H.; Green, L. A., Fundamentals and applications of electrospray ionization mass spectrometry for petroleum characterization. *Energy & Fuels* **2004,** *18* (6), 1784-1791.
76. Qian, K.; Edwards, K. E.; Mennito, A. S.; Walters, C. C.; Kushnerick, J. D., Enrichment, Resolution, and Identification of Nickel Porphyrins in Petroleum Asphaltene by Cyclograph Separation and Atmospheric Pressure Photoionization Fourier Transform Ion Cyclotron Resonance Mass Spectrometry. *Anal. Chem.* **2010,** *82* (1), 413-419.
77. Cho, Y.; Witt, M.; Jin, J. M.; Kim, Y. H.; Nho, N. S.; Kim, S., Evaluation of Laser Desorption Ionization Coupled to Fourier Transform Ion Cyclotron Resonance Mass Spectrometry To Study Metalloporphyrin Complexes. *Energy & Fuels* **2014,** *28* (11), 6699.
78. Zhao, X.; Liu, Y.; Xu, C.; Yan, Y.; Zhang, Y.; Zhang, Q.; Zhao, S.; Chung, K.; Gray, M. R.; Shi, Q., Separation and Characterization of Vanadyl Porphyrins in Venezuela Orinoco Heavy Crude Oil. *Energy & Fuels* **2013,** *27* (6), 2874-2882.
79. Ocampo, R.; Callot, H. J.; Albrecht, P., Occurrence of bacteriopetroporphyrins in oil shale. *Journal of the Chemical Society, Chemical Communications* **1985,** (4), 200-201.
80. Ocampo, R.; Callot, H. J.; Albrecht, P., Identification of polar porphyrins in oil shale. *Journal of the Chemical Society, Chemical Communications* **1985,** (4), 198-200.
81. Jarvis, J. M.; Sudasinghe, N. M.; Albrecht, K. O.; Schmidt, A. J.; Hallen, R. T.; Anderson, D. B.; Billing, J. M.; Schaub, T. M., Impact of iron porphyrin complexes when hydroprocessing algal HTL biocrude. *Fuel* **2016,** *182*, 411-418.
82. Qian, K.; Fredriksen, T. R.; Mennito, A. S.; Zhang, Y.; Harper, M. R.; Merchant, S.; Kushnerick, J. D.; Rytting, B. M.; Kilpatrick, P. K., Evidence of naturally-occurring vanadyl porphyrins containing multiple S and O atoms. *Fuel* **2019,** *239*, 1258-1264.
83. Zhao, X.; Shi, Q.; Gray, M. R.; Xu, C., New Vanadium Compounds in Venezuela Heavy Crude Oil Detected by Positive-ion Electrospray Ionization Fourier Transform Ion Cyclotron Resonance Mass Spectrometry. *Scientific Reports* **2014,** *4* (1), 5373.
84. Senglet, N.; Williams, C.; Faure, D.; Des Courières, T.; Guilard, R., Microheterogeneity study of heavy crude petroleum by u.v.-visible spectroscopy and small angle X-ray scattering. *Fuel* **1990,** *69* (1), 72-77.
85. Berthe, C.; Muller, J.; Cagnian, D.; Grinbitt, J.; Bonnelle, J. In *Characterization of heavy petroleum fractions by IR and UV-visible spectroscopy, ESCA photoelectronic spectroscopy and LAMMA spectroscopy in relation to the vanadium environment*, Collect. Colloq. Semin. (Inst. Fr. Pet.), 1984; pp 164-168.
86. Goulon, J.; Retournard, A.; Friant, P.; Goulon-Ginet, C.; Berthe, C.; Muller, J.-F.; Poncet, J.-L.; Guilard, R.; Escalier, J.-C.; Neff, B., Structural characterization by X-ray absorption spectroscopy (EXAFS/XANES) of the vanadium chemical environment in Boscan asphaltenes. *J. Chem. Soc., Dalton Trans.* **1984,** (6), 1095-1103.

87. Poncet, J.; Guilard, R.; Friant, P.; Goulonginet, C.; Goulon, J., Vanadium (IV) porphyrins-synthesis and classification of thiovanadyl and selenovanadyl porphyrins-EXAFS and RPE spectroscopic studies. *NOUVEAU JOURNAL DE CHIMIE-NEW JOURNAL OF CHEMISTRY* **1984,** *8* (10), 583-590.
88. Loos, M.; Ascone, I.; Friant, P.; Ruiz-Lopez, M. F.; Goulon, J.; Barbe, J. M.; Senglet, N.; Guilard, R.; Faure, D.; Des Courieres, T., Vanadyl porphyrins: evidence for self-association and for specific interactions with hydroprocessing catalysts shown from X.A.F.S. and E.S.R. studies. *Catal. Today* **1990,** *7* (4), 497-513.
89. Yokota, T.; Scriven, F.; Montgomery, D. S.; Strausz, O. P., Absorption and emission spectra of Athabasca asphaltene in the visible and near ultraviolet regions. *Fuel* **1986,** *65* (8), 1142-1149.
90. Antipenko, V.; Zemtseva, L., Multiplicative hindrances in the quantitative analysis of petroleum metal porphyrins. *Petroleum Chemistry* **1996,** *36* (1), 31-42.
91. Gutierrez Sama, S.; Desprez, A.; Krier, G.; Lienemann, C.-P.; Barbier, J.; Lobinski, R.; Barrere-Mangote, C.; Giusti, P.; Bouyssiere, B., Study of the Aggregation of Metal Complexes with Asphaltenes Using Gel Permeation Chromatography Inductively Coupled Plasma High-Resolution Mass Spectrometry. *Energy & Fuels* **2016,** *30* (9), 6907-6912.
92. Kim, T.; Ryu, J.; Kim, M.-J.; Kim, H.-J.; Shul, Y.-G.; Jeon, Y.; Park, J.-I., Characterization and analysis of vanadium and nickel species in atmospheric residues. *Fuel* **2014,** *117*, 783-791.
93. Caumette, G.; Lienemann, C. P.; Merdrignac, I.; Bouyssiere, B.; Lobinski, R., Fractionation and speciation of nickel and vanadium in crude oils by size exclusion chromatography-ICP MS and normal phase HPLC-ICP MS. *J. Anal. At. Spectrom.* **2010,** *25* (7), 1123-1129.
94. Gascon, G.; Vargas, V.; Feo, L.; Castellano, O.; Castillo, J.; Giusti, P.; Acavedo, S.; Lienemann, C. P.; Bouyssiere, B., Size Distributions of Sulfur, Vanadium, and Nickel Compounds in Crude Oils, Residues, and Their Saturate, Aromatic, Resin, and Asphaltene Fractions Determined by Gel Permeation Chromatography Inductively Coupled Plasma High-Resolution Mass Spectrometry. *Energy and Fuels* **2017,** *31* (8), 7783-7788.
95. Desprez, A.; Bouyssiere, B.; Arnaudguilhem, C.; Krier, G.; Vernex-Loset, L.; Giusti, P., Study of the size distribution of sulfur, vanadium, and nickel compounds in four crude oils and their distillation cuts by gel permeation chromatography inductively coupled plasma high-resolution mass spectrometry. *Energy and Fuels* **2014,** *28* (6), 3730-3737.
96. Duyck, C. B.; Saint'Pierre, T. D.; Miekeley, N.; Da Fonseca, T. C. O.; Szatmari, P., High performance liquid chromatography hyphenated to inductively coupled plasma mass spectrometry for v and Ni quantification as tetrapyrroles. *Spectrochimica Acta Part B: Atomic Spectroscopy* **2011,** *66* (5), 362-367.
97. Ellis, J.; Rechsteiner, C.; Moir, M.; Wilbur, S., Determination of volatile nickel and vanadinum species in crude oil and crude oil fractions by gas chromatography coupled to inductively coupled plasma mass spectrometry. *J. Anal. At. Spectrom.* **2011,** *26* (8), 1674-1678.
98. Gaulier, F.; Gibert, A.; Walls, D.; Langford, M.; Baker, S.; Baudot, A.; Porcheron, F.; Lienemann, C. P., Mercury speciation in liquid petroleum products: Comparison between on-site approach and lab measurement using size exclusion chromatography with high resolution inductively coupled plasma mass spectrometric detection (SEC-ICP-HR MS). *Fuel Process. Technol.* **2015,** *131*, 254-261.
99. Gutiérrez Sama, S.; Farenc, M.; Barrère-Mangote, C.; Lobinski, R.; Afonso, C.; Bouyssière, B.; Giusti, P., Molecular Fingerprints and Speciation of Crude Oils and Heavy Fractions Revealed by Molecular and Elemental Mass Spectrometry: Keystone between Petroleomics, Metallopetroleomics, and Petrointeractomics. *Energy & Fuels* **2018,** *32* (4), 4593-4605.
100. Ligiero, L. M.; Bouriat, P.; Dicharry, C.; Passade-Boupat, N.; Lalli, P. M.; Rodgers, R. P.; Barrère-Mangote, C.; Giusti, P.; Bouyssiere, B., Characterization of Crude Oil Interfacial Material Isolated by the Wet Silica Method. Part 1: Gel Permeation Chromatography Inductively Coupled Plasma High-Resolution Mass Spectrometry Analysis. *Energy and Fuels* **2017,** *31* (2), 1065-1071.
101. Mello, P. A.; Pereira, J. S. F.; Mesko, M. F.; Barin, J. S.; Flores, E. M. M., Sample preparation methods for subsequent determination of metals and non-metals in crude oil-A review. *Anal. Chim. Acta* **2012,** *746*, 15-36.
102. Pohl, P.; Dural, J.; Vorapalawut, N.; Merdrignac, I.; Lienemann, C. P.; Carrier, H.; Grassl, B.; Bouyssiere, B.; Lobinski, R., Multielement molecular size fractionation in crude oil and oil residue by size exclusion microchromatography with high resolution inductively coupled plasma mass spectrometric detection (HR ICP MS). *J. Anal. At. Spectrom.* **2010,** *25* (12), 1974-1977.

103. Vorapalawut, N.; Martinez Labrador, M.; Pohl, P.; Caetano, M.; Chirinos, J.; Arnaudguilhem, C.; Bouyssiere, B.; Shiowatana, J.; Lobinski, R., Application of TLC and la ICP SF MS for speciation of S, Ni and v in petroleum samples. *Talanta* **2012,** *97*, 574-578.
104. Acevedo, S.; Guzman, K.; Labrador, H.; Carrier, H.; Bouyssiere, B.; Lobinski, R., Trapping of Metallic Porphyrins by Asphaltene Aggregates: A Size Exclusion Microchromatography With High-Resolution Inductively Coupled Plasma Mass Spectrometric Detection Study. *Energy & Fuels* **2012,** *26* (8), 4968-4977.
105. Miller, J. T.; Fisher, R. B.; van der Eerden, A. M. J.; Koningsberger, D. C., Structural Determination by XAFS Spectroscopy of Non-Porphyrin Nickel and Vanadium in Maya Residuum, Hydrocracked Residuum, and Toluene-Insoluble Solid. *Energy & Fuels* **1999,** *13* (3), 719-727.
106. Bonnett, R.; Brewer, P.; Noro, K.; Noro, T., Chemistry of Vanadyl Porphyrins. *Tetrahedron* **1978,** *34* (3), 379-385.
107. Bencosme, C. S.; Romero, C.; Simoni, S., Axial interaction of vanadyltetraphenylporhyrin with Lewis bases. *Inorg. Chem.* **1985,** *24* (10), 1603-1604.
108. Dickson, F. E.; Kunesh, C. J.; McGinnis, E. L.; Petrakis, L., Use of electron spin resonance to characterize the vanadium(IV)-sulfur species in petroleum. *Anal. Chem.* **1972,** *44* (6), 978-981.
109. Dickson, F. E.; Petrakis, L., Application of electron spin resonance and electronic spectroscopy to the characterization of vanadium species in petroleum fractions. *Anal. Chem.* **1974,** *46* (8), 1129-1130.
110. Schabron, J. F.; Rovani, J. F.; Sanderson, M. M., Asphaltene Determinator Method for Automated On-Column Precipitation and Redissolution of Pericondensed Aromatic Asphaltene Components. *Energy & Fuels* **2010,** *24* (11), 5984-5996.
111. Kharrat, A. M.; Zacharia, J.; Cherian, V. J.; Anyatonwu, A., Issues with Comparing SARA Methodologies. *Energy & Fuels* **2007,** *21* (6), 3618-3621.
112. Rogel, E.; Miao, T.; Vien, J.; Roye, M., Comparing asphaltenes: Deposit versus crude oil. *Fuel* **2015,** *147*, 155-160.
113. Rogel, E.; Roye, M.; Vien, J.; Miao, T., Characterization of Asphaltene Fractions: Distribution, Chemical Characteristics, and Solubility Behavior. *Energy & Fuels* **2015,** *29* (4), 2143-2152.
114. Brown, J., A Study of the Hydrogen Distribution in Coal-like Materials by High-resolution Nuclear Magnetic Resonance Spectroscopy I-The Measurement and Interpreatation of the Spectra. *Fuel* **1960,** *39*, 79-86.
115. Brown, J.; Ladner, W., A study of the hydrogen distribution in coal-like materials by high-resolution nuclear magnetic resonance spectroscopy. 2. A comparison with infra-red measurement and the conversion to carbon structure. *Fuel* **1960,** *39* (1), 87-96.
116. Eyssautier, J.; Levitz, P.; Espinat, D.; Jestin, J.; Gummel, J.; Grillo, I.; Barré, L., Insight into Asphaltene Nanoaggregate Structure Inferred by Small Angle Neutron and X-ray Scattering. *The Journal of Physical Chemistry B* **2011,** *115* (21), 6827-6837.
117. Strausz, O. P.; Peng, P. a.; Murgich, J., About the Colloidal Nature of Asphaltenes and the MW of Covalent Monomeric Units. *Energy & Fuels* **2002,** *16* (4), 809-822.
118. Guzman, A.; Bueno, A.; Carbognani, L., Molecular Weight Determination of Asphaltenes from Colombian Crudes by Size Exclusion Chromatography (SEC) and Vapor Pressure Osmometry (VPO). *Pet. Sci. Technol.* **2009,** *27* (8), 801-816.
119. Hortal, A. R.; Martínez-Haya, B.; Lobato, M. D.; Pedrosa, J. M.; Lago, S., On the determination of molecular weight distributions of asphaltenes and their aggregates in laser desorption ionization experiments. *J. Mass Spectrom.* **2006,** *41* (7), 960-968.
120. Martínez-Haya, B.; Hortal, A. R.; Hurtado, P.; Lobato, M. D.; Pedrosa, J. M., Laser desorption/ionization determination of molecular weight distributions of polyaromatic carbonaceous compounds and their aggregates. *J. Mass Spectrom.* **2007,** *42* (6), 701-713.
121. Nali, M.; Manclossi, A., SIZE EXCLUSION CHROMATOGRAPHY AND VAPOR PRESSURE OSMOMETRY IN THE DETERMINATION OF ASPHALTENE MOLECULAR WEIGHT. *Fuel Sci. Technol. Int.* **1995,** *13* (10), 1051-1264.
122. Sato, S.; Takanohashi, T.; Tanaka, R., Molecular Weight Calibration of Asphaltenes Using Gel Permeation Chromatography/Mass Spectrometry. *Energy & Fuels* **2005,** *19* (5), 1991-1994.
123. Groenzin, H.; Mullins, O. C., Asphaltene Molecular Size and Structure. *The Journal of Physical Chemistry A* **1999,** *103* (50), 11237-11245.

124. Groenzin, H.; Mullins, O. C., Molecular Size and Structure of Asphaltenes from Various Sources. *Energy & Fuels* **2000,** *14* (3), 677-684.
125. Strausz, O. P.; Safarik, I.; Lown, E. M.; Morales-Izquierdo, A., A Critique of Asphaltene Fluorescence Decay and Depolarization-Based Claims about Molecular Weight and Molecular Architecture. *Energy & Fuels* **2008,** *22* (2), 1156-1166.
126. Morgan, T. J.; Millan, M.; Behrouzi, M.; Herod, A. A.; Kandiyoti, R., On the Limitations of UV−Fluorescence Spectroscopy in the Detection of High-Mass Hydrocarbon Molecules. *Energy & Fuels* **2005,** *19* (1), 164-169.
127. Mullins, O. C.; Martínez-Haya, B.; Marshall, A. G., Contrasting Perspective on Asphaltene Molecular Weight. This Comment vs the Overview of A. A. Herod, K. D. Bartle, and R. Kandiyoti. *Energy & Fuels* **2008,** *22* (3), 1765-1773.
128. Marshall, A. G.; Rodgers, R. P., Petroleomics: The Next Grand Challenge for Chemical Analysis. *Acc. Chem. Res.* **2004,** *37* (1), 53-59.
129. Rodgers, R. P.; Marshall, A. G., Petroleomics: Advanced Characterization of Petroleum-Derived Materials by Fourier Transform Ion Cyclotron Resonance Mass Spectrometry (FT-ICR MS). In *Asphaltenes, Heavy Oils, and Petroleomics*, Mullins, O. C.; Sheu, E. Y.; Hammami, A.; Marshall, A. G., Eds. Springer New York: New York, NY, 2007; pp 63-93.
130. Marshall, A. G.; Rodgers, R. P., Petroleomics: Chemistry of the underworld. *Proceedings of the National Academy of Sciences* **2008,** *105* (47), 18090.
131. Klein, G. C.; Kim, S.; Rodgers, R. P.; Marshall, A. G.; Yen, A., Mass Spectral Analysis of Asphaltenes. II. Detailed Compositional Comparison of Asphaltenes Deposit to Its Crude Oil Counterpart for Two Geographically Different Crude Oils by ESI FT-ICR MS. *Energy & Fuels* **2006,** *20* (5), 1973-1979.
132. Huba, A. K.; Huba, K.; Gardinali, P. R., Understanding the atmospheric pressure ionization of petroleum components: The effects of size, structure, and presence of heteroatoms. *Sci. Total Environ.* **2016,** *568*, 1018-1025.
133. Jiang, B.; Liang, Y.; Xu, C.; Zhang, J.; Hu, M.; Shi, Q., Polycyclic Aromatic Hydrocarbons (PAHs) in Ambient Aerosols from Beijing: Characterization of Low Volatile PAHs by Positive-Ion Atmospheric Pressure Photoionization (APPI) Coupled with Fourier Transform Ion Cyclotron Resonance. *Environmental Science & Technology* **2014,** *48* (9), 4716-4723.
134. McKenna, A. M.; Chacón-Patiño, M. L.; Weisbrod, C. R.; Blakney, G. T.; Rodgers, R. P., Molecular-Level Characterization of Asphaltenes Isolated from Distillation Cuts. *Energy & Fuels* **2019,** *33* (3), 2018-2029.
135. Nyadong, L.; Lai, J.; Thompsen, C.; LaFrancois, C. J.; Cai, X.; Song, C.; Wang, J.; Wang, W., High-Field Orbitrap Mass Spectrometry and Tandem Mass Spectrometry for Molecular Characterization of Asphaltenes. *Energy & Fuels* **2018,** *32* (1), 294-305.
136. Lozano, D. C. P.; Thomas, M. J.; Jones, H. E.; Barrow, M. P., Petroleomics: Tools, Challenges, and Developments. *Annual Review of Analytical Chemistry* **2020**.
137. Panda, S. K.; Brockmann, K.-J.; Benter, T.; Schrader, W., Atmospheric pressure laser ionization (APLI) coupled with Fourier transform ion cyclotron resonance mass spectrometry applied to petroleum samples analysis: comparison with electrospray ionization and atmospheric pressure photoionization methods. *Rapid Commun. Mass Spectrom.* **2011,** *25* (16), 2317-2326.
138. Gaspar, A.; Zellermann, E.; Lababidi, S.; Reece, J.; Schrader, W., Characterization of Saturates, Aromatics, Resins, and Asphaltenes Heavy Crude Oil Fractions by Atmospheric Pressure Laser Ionization Fourier Transform Ion Cyclotron Resonance Mass Spectrometry. *Energy & Fuels* **2012,** *26* (6), 3481-3487.
139. Witt, M.; Godejohann, M.; Oltmanns, S.; Moir, M.; Rogel, E., Characterization of Asphaltenes Precipitated at Different Solvent Power Conditions Using Atmospheric Pressure Photoionization (APPI) and Laser Desorption Ionization (LDI) Coupled to Fourier Transform Ion Cyclotron Resonance Mass Spectrometry (FT-ICR MS). *Energy & Fuels* **2018,** *32* (3), 2653-2660.
140. Pereira, T. M. C.; Vanini, G.; Tose, L. V.; Cardoso, F. M. R.; Fleming, F. P.; Rosa, P. T. V.; Thompson, C. J.; Castro, E. V. R.; Vaz, B. G.; Romão, W., FT-ICR MS analysis of asphaltenes: Asphaltenes go in, fullerenes come out. *Fuel* **2014,** *131*, 49-58.
141. Schuler, B.; Meyer, G.; Peña, D.; Mullins, O. C.; Gross, L., Unraveling the Molecular Structures of Asphaltenes by Atomic Force Microscopy. *J. Am. Chem. Soc.* **2015,** *137* (31), 9870-9876.
142. Balestrin, L. B. d. S.; Cardoso, M. B.; Loh, W., Using Atomic Force Microscopy To Detect Asphaltene Colloidal Particles in Crude Oils. *Energy & Fuels* **2017,** *31* (4), 3738-3746.

143. Zhang, Y.; Schulz, F.; Rytting, B. M.; Walters, C. C.; Kaiser, K.; Metz, J. N.; Harper, M. R.; Merchant, S. S.; Mennito, A. S.; Qian, K.; Kushnerick, J. D.; Kilpatrick, P. K.; Gross, L., Elucidating the Geometric Substitution of Petroporphyrins by Spectroscopic Analysis and Atomic Force Microscopy Molecular Imaging. *Energy & Fuels* **2019,** *33* (7), 6088-6097.
144. Zhang, L.; Zhao, S.; Xu, Z.; Chung, K. H.; Zhao, C.; Zhang, N.; Xu, C.; Shi, Q., Molecular Weight and Aggregation of Heavy Petroleum Fractions Measured by Vapor Pressure Osmometry and a Hindered Stepwise Aggregation Model. *Energy & Fuels* **2014,** *28* (10), 6179-6187.
145. Yarranton, H. W.; Ortiz, D. P.; Barrera, D. M.; Baydak, E. N.; Barré, L.; Frot, D.; Eyssautier, J.; Zeng, H.; Xu, Z.; Dechaine, G.; Becerra, M.; Shaw, J. M.; McKenna, A. M.; Mapolelo, M. M.; Bohne, C.; Yang, Z.; Oake, J., On the Size Distribution of Self-Associated Asphaltenes. *Energy & Fuels* **2013,** *27* (9), 5083-5106.
146. Gray, M. R.; Tykwinski, R. R.; Stryker, J. M.; Tan, X., Supramolecular Assembly Model for Aggregation of Petroleum Asphaltenes. *Energy & Fuels* **2011,** *25* (7), 3125-3134.
147. Gawrys, K. L.; Blankenship, G. A.; Kilpatrick, P. K., On the Distribution of Chemical Properties and Aggregation of Solubility Fractions in Asphaltenes. *Energy & Fuels* **2006,** *20* (2), 705-714.
148. Östlund, J.-A.; Nydén, M.; Auflem, I. H.; Sjöblom, J., Interactions between Asphaltenes and Naphthenic Acids. *Energy & Fuels* **2003,** *17* (1), 113-119.
149. Stoyanov, S. R.; Yin, C.-X.; Gray, M. R.; Stryker, J. M.; Gusarov, S.; Kovalenko, A., Computational and Experimental Study of the Structure, Binding Preferences, and Spectroscopy of Nickel(II) and Vanadyl Porphyrins in Petroleum. *The Journal of Physical Chemistry B* **2010,** *114* (6), 2180-2188.
150. Gray, M. R.; Yarranton, H. W., Quantitative Modeling of Formation of Asphaltene Nanoaggregates. *Energy & Fuels* **2019,** *33* (9), 8566-8575.
151. Buenrostro-Gonzalez, E.; Lira-Galeana, C.; Gil-Villegas, A.; Wu, J., Asphaltene precipitation in crude oils: Theory and experiments. *AlChE J.* **2004,** *50* (10), 2552-2570.
152. Hassanvand, M.; Shahsavani, B.; Anooshe, A., Study of temperature effect on asphaltene precipitation by visual and quantitative methods. *Journal of Petroleum Technology and Alternative Fuels* **2012,** *3* (2), 8-18.
153. Li, X.; Berg, S.; Castellanos-Diaz, O.; Wiegmann, A.; Verlaan, M., Solvent-dependent recovery characteristic and asphaltene deposition during solvent extraction of heavy oil. *Fuel* **2020,** *263*, 116716.
154. Alimohammadi, S.; Zendehboudi, S.; James, L., A comprehensive review of asphaltene deposition in petroleum reservoirs: Theory, challenges, and tips. *Fuel* **2019,** *252*, 753-791.
155. Vazquez, D.; Mansoori, G. A., Identification and measurement of petroleum precipitates. *Journal of Petroleum Science and Engineering* **2000,** *26* (1), 49-55.
156. Mullins, O. C., The Modified Yen Model. *Energy & Fuels* **2010,** *24* (4), 2179-2207.
157. Maqbool, T.; Srikiratiwong, P.; Fogler, H. S., Effect of Temperature on the Precipitation Kinetics of Asphaltenes. *Energy & Fuels* **2011,** *25* (2), 694-700.
158. Evdokimov, I. N.; Fesan, A. A.; Losev, A. P., New Answers to the Optical Interrogation of Asphaltenes: Complex States of Primary Aggregates from Steady-State Fluorescence Studies. *Energy & Fuels* **2016,** *30* (10), 8226-8235.
159. Rashid, Z.; Wilfred, C. D.; Gnanasundaram, N.; Arunagiri, A.; Murugesan, T., A comprehensive review on the recent advances on the petroleum asphaltene aggregation. *Journal of Petroleum Science and Engineering* **2019,** *176*, 249-268.
160. Mack, C., Colloid Chemistry of Asphalts. *The Journal of Physical Chemistry* **1932,** *36* (12), 2901-2914.
161. Dickie, J. P.; Yen, T. F., Macrostructures of the asphaltic fractions by various instrumental methods. *Anal. Chem.* **1967,** *39* (14), 1847-1852.
162. Moncada, J.; Schartung, D.; Stephens, N.; Oh, T.-S.; Carrero, C. A., Determining the flocculation point of asphaltenes combining ultrasound and electrochemical impedance spectroscopy. *Fuel* **2019,** *241*, 870-875.
163. Fenistein, D.; Barré, L., Experimental measurement of the mass distribution of petroleum asphaltene aggregates using ultracentrifugation and small-angle X-ray scattering. *Fuel* **2001,** *80* (2), 283-287.
164. Mullins, O. C., The Asphaltenes. *Annual Review of Analytical Chemistry* **2011,** *4* (1), 393-418.
165. Mullins, O. C.; Sabbah, H.; Eyssautier, J.; Pomerantz, A. E.; Barré, L.; Andrews, A. B.; Ruiz-Morales, Y.; Mostowfi, F.; McFarlane, R.; Goual, L.; Lepkowicz, R.; Cooper, T.; Orbulescu, J.; Leblanc, R. M.; Edwards, J.; Zare, R. N., Advances in Asphaltene Science and the Yen–Mullins Model. *Energy & Fuels* **2012,** *26* (7), 3986-4003.
166. Zhang, Y.; Siskin, M.; Gray, M. R.; Walters, C. C.; Rodgers, R. P., Mechanisms of Asphaltene Aggregation: Puzzles and a New Hypothesis. *Energy & Fuels* **2020**.

167. Waters, M. L., Aromatic Interactions. *Acc. Chem. Res.* **2013,** *46* (4), 873-873.
168. Sedghi, M.; Goual, L.; Welch, W.; Kubelka, J., Effect of Asphaltene Structure on Association and Aggregation Using Molecular Dynamics. *The Journal of Physical Chemistry B* **2013,** *117* (18), 5765-5776.
169. Morantes, L. R.; Percebom, A. M.; Mejía-Ospino, E., On the molecular basis of aggregation and stability of Colombian asphaltenes and their subfractions. *Fuel* **2019,** *241*, 542-549.
170. Boduszynski, M. M.; Hurtubise, R. J.; Silver, H. F., Separation of solvent-refined coal into solvent-derived fractions. *Anal. Chem.* **1982,** *54* (3), 372-375.
171. Rogel, E.; Roye, M.; Vien, J.; Witt, M., Equivalent Distillation: A Path to a Better Understanding of Asphaltene Characteristics and Behavior. In *The Boduszynski Continuum: Contributions to the Understanding of the Molecular Composition of Petroleum*, American Chemical Society: 2018; Vol. 1282, pp 51-72.
172. Miller, J. T.; Fisher, R. B.; Thiyagarajan, P.; Winans, R. E.; Hunt, J. E., Subfractionation and Characterization of Mayan Asphaltene. *Energy & Fuels* **1998,** *12* (6), 1290-1298.
173. Acevedo, S.; Escobar, G.; Ranaudo, M. A.; Piñate, J.; Amorín, A.; Díaz, M.; Silva, P., Observations about the Structure and Dispersion of Petroleum Asphaltenes Aggregates Obtained from Dialysis Fractionation and Characterization. *Energy & Fuels* **1997,** *11* (4), 774-778.
174. Kharrat, A. M., Characterization of Canadian Heavy Oils Using Sequential Extraction Approach. *Energy & Fuels* **2009,** *23* (2), 828-834.
175. Boduszyński, M.; Chadha, B. R.; Szkuta-Pochopień, T., Investigations on Romashkino asphaltic bitumen. 3. Fractionation of asphaltenes using ion-exchange chromatography. *Fuel* **1977,** *56* (4), 432-436.
176. Carbognani, L., Preparative Subfractionation of Petroleum Resins and Asphaltenes. I. Development of Size Exclusion Separation Methodology. *Pet. Sci. Technol.* **2003,** *21* (11-12), 1685-1703.
177. Yang, X.; Hamza, H.; Czarnecki, J., Investigation of Subfractions of Athabasca Asphaltenes and Their Role in Emulsion Stability. *Energy & Fuels* **2004,** *18* (3), 770-777.
178. Ovalles, C.; Rogel, E.; Moir, M.; Thomas, L.; Pradhan, A., Characterization of Heavy Crude Oils, Their Fractions, and Hydrovisbroken Products by the Asphaltene Solubility Fraction Method. *Energy & Fuels* **2012,** *26* (1), 549-556.
179. Barré, L.; Simon, S.; Palermo, T., Solution Properties of Asphaltenes. *Langmuir* **2008,** *24* (8), 3709-3717.
180. Guiliano, M.; Boukir, A.; Doumenq, P.; Mille, G.; Crampon, C.; Badens, E.; Charbit, G., Supercritical Fluid Extraction of Bal 150 Crude Oil Asphaltenes. *Energy & Fuels* **2000,** *14* (1), 89-94.
181. Zhang, L.; Xu, Z.; Quan, S.; Sun, X.; Na, Z.; Zhang, Y.; Chung, K. H.; Xu, C.; Zhao, S., Molecular Characterization of Polar Heteroatom Species in Venezuela Orinoco Petroleum Vacuum Residue and Its Supercritical Fluid Extraction Subfractions. *Energy & Fuels* **2012,** *26* (9), 5795-5803.
182. Marques, J.; Merdrignac, I.; Baudot, A.; Barré, L.; Guillaume, D.; Espinat, D.; Brunet, S., Asphaltenes size polydispersity reduction by nano-and ultrafiltration separation methods–comparison with the flocculation method. *Oil & Gas Science and Technology-Revue de l'IFP* **2008,** *63* (1), 139-149.
183. Marques, J.; Guillaume, D.; Merdrignac, I.; Espinat, D.; Barré, L.; Brunet, S., Asphaltene cross-flow membrane ultrafiltration on a preparative scale and feedstock reconstitution method. *Oil & Gas Science and Technology-Revue de l'IFP* **2009,** *64* (6), 795-806.
184. Subramanian, S.; Simon, S.; Gao, B.; Sjöblom, J., Asphaltene fractionation based on adsorption onto calcium carbonate: Part 1. Characterization of sub-fractions and QCM-D measurements. *Colloids and Surfaces A: Physicochemical and Engineering Aspects* **2016,** *495*, 136-148.
185. Subramanian, S.; Sørland, G. H.; Simon, S.; Xu, Z.; Sjöblom, J., Asphaltene fractionation based on adsorption onto calcium carbonate: Part 2. Self-association and aggregation properties. *Colloids and Surfaces A: Physicochemical and Engineering Aspects* **2017,** *514*, 79-90.
186. Ruwoldt, J.; Subramanian, S.; Simon, S.; Oschmann, H.; Sjöblom, J., Asphaltene fractionation based on adsorption onto calcium carbonate: Part 3. Effect of asphaltenes on wax crystallization. *Colloids and Surfaces A: Physicochemical and Engineering Aspects* **2018,** *554*, 129-141.
187. Fan, S.; Liu, H.; Wang, J.; Chen, H.; Bai, R.; Guo, A.; Chen, K.; Huang, J.; Wang, Z., Microwave-assisted Petroporphyrin Release from Asphaltene Aggregates in Polar Solvents. *Energy & Fuels* **2020,** *34* (3), 2683-2692.
188. Chung, K. H.; Xu, C.; Hu, Y.; Wang, R., Supercritical fluid extraction reveals resid properties. *Oil & Gas Journal* **1997,** *95* (3), 66-69.

189. Shi, Q.; Pan, N.; Long, H.; Cui, D.; Guo, X.; Long, Y.; Chung, K. H.; Zhao, S.; Xu, C.; Hsu, C. S., Characterization of Middle-Temperature Gasification Coal Tar. Part 3: Molecular Composition of Acidic Compounds. *Energy & Fuels* **2013,** *27* (1), 108-117.
190. Zhang, L.; Xu, Z.; Shi, Q.; Sun, X.; Zhang, N.; Zhang, Y.; Chung, K. H.; Xu, C.; Zhao, S., Molecular Characterization of Polar Heteroatom Species in Venezuela Orinoco Petroleum Vacuum Residue and Its Supercritical Fluid Extraction Subfractions. *Energy & Fuels* **2012,** *26* (9), 5795-5803.
191. Gardner, R. D.; Pope, M. C.; Wehner, M.; Donovan, A. D., Comparative stratigraphy of the Eagle Ford Group strata in Lozier Canyon and Antonio Creek, Terrell County, Texas. *Gcags Journal* **2013,** *2*, 42-52.
192. Sun, X.; Zhang, T.; Sun, Y.; Milliken, K. L.; Sun, D., Geochemical evidence of organic matter source input and depositional environments in the lower and upper Eagle Ford Formation, south Texas. *Org. Geochem.* **2016,** *98*, 66-81.
193. Damsté, J. S. S.; Keely, B. J.; Betts, S. E.; Baas, M.; Maxwell, J. R.; de Leeuw, J. W., Variations in abundances and distributions of isoprenoid chromans and long-chain alkylbenzenes in sediments of the Mulhouse Basin: a molecular sedimentary record of palaeosalinity. *Org. Geochem.* **1993,** *20* (8), 1201-1215.
194. Vernemismer, J.; Ocampo, R.; Callot, H. J.; Albrecht, P., Isolation of a series of vanadyl-tetrahydrobenzopetroporphyrins from Timahdit oil shale. Structure determination and total synthesis of the major constituent. *Journal of the Chemical Society Chemical Communications* **1987,** *20* (20), 1581-1583.
195. Huszánk, R.; Horváth, O., A heme-like, water-soluble iron(II) porphyrin: thermal and photoinduced properties, evidence for sitting-atop structure. *Chem. Commun.* **2005,** *2* (2), 224.
196. Eckardt, C. B.; Wolf, M.; Maxwell, J. R., Iron porphyrins in the Permian Kupferschiefer of the lower Rhine Basin, N.W. Germany. *Org. Geochem.* **1989,** *14* (6), 659-666.
197. Furimsky, E., On Exclusivity of Vanadium and Nickel Porphyrins in Crude Oil. *Energy & Fuels* **2016,** *30* (11), 9978-9980.
198. Structural Biochemistry/Protein function/Hemoglobin. https://en.wikibooks.org/wiki/Structural_Biochemistry/Protein_function/Hemoglobin.
199. Bennett, R.; Czechowski, F., Gallium porphyrins in bituminous coal. *Nature* **1980,** *283* (5746), 465-467.
200. Bonnett, R.; Czechowski, F., Metalloporphyrins in coal. 1. Gallium porphyrins in bituminous coals. *Journal of the Chemical Society Perkin Transactions* **1984,** *28* (1), 61-65.
201. Lu, J.; Zhang, Y.; Shi, Q., Ionizing Aromatic Compounds in Petroleum by Electrospray with HCOONH4 as Ionization Promoter. *Anal. Chem.* **2016,** *88* (7), 3471-3475.
202. Bouldin, M. G., Gilsonite modifier hard pen binder study. *American Gilsonite Company* **2002,** *5*.
203. Siswosoebrotho, B. I.; Kusnianti, N.; Tumewu, W. In *Laboratory evaluation of lawele Buton natural asphalt in asphalt concrete mixture*, Proceedings of the Eastern Asia Society for Transportation Studies, 2005; pp 857-867.
204. Hadiwardoyo, S. P.; Sinaga, E. S.; Fikri, H., The influence of Buton asphalt additive on skid resistance based on penetration index and temperature. *Construction and Building Materials* **2013,** *42*, 5-10.
205. Ameri, M.; Mansourian, A.; Ashani, S. S.; Yadollahi, G., Technical study on the Iranian Gilsonite as an additive for modification of asphalt binders used in pavement construction. *Construction and Building Materials* **2011,** *25* (3), 1379-1387.
206. Lee, H. J.; Lee, J. H.; Park, H. M., Performance evaluation of high modulus asphalt mixtures for long life asphalt pavements. *Construction and building materials* **2007,** *21* (5), 1079-1087.
207. Barwise, A.; Park, P., Petroporphyrin fingerprinting as a geochemical marker. In *Advances in Organic Geochemistry 1981*, Wiley Chichester: 1983; pp 668-674.
208. Didyk, B. M.; Alturki, Y. I. A.; Pillinger, C. T.; Eglinton, G., Petroporphyrins as indicators of geothermal maturation. *Nature* **1975,** *256* (5518), 563-565.
209. N. Dunning, H.; W. Moore, J.; Bieber, H.; B. Williams, R., *Porphyrin, Nickel, Vanadium, and Nitrogen in Petroleum*. 1960; Vol. 5.
210. Hodgson, G.; Baker, B., Evidence for porphyrins in the Orgueil meteorite. *Nature* **1964,** *202* (4928), 125.
211. Hodgson, G. W.; Baker, B. L.; Peake, E., The Role of Porphyrins in the Geochemistry of Petroleum. In *7th World Petroleum Congress*, World Petroleum Congress: Mexico City, Mexico, 1967; pp 117-128.
212. Sundararaman, P., On the mechanism of change in DPEP/ETIO ratio with maturity. *Geochim. Cosmochim. Acta* **1993,** *57* (18), 4517-4520.

213. Fish, R. H.; Reynolds, J. G.; Gallegos, E. J., Molecular Characterization of Nickel and Vanadium Nonporphyrin Compounds Found in Heavy Crude Petroleums and Bitumens. In *Metal Complexes in Fossil Fuels*, American Chemical Society: 1987; Vol. 344, pp 332-349.
214. Cho, Y.; Jin, J. M.; Witt, M.; Birdwell, J. E.; Na, J.-G.; Roh, N.-S.; Kim, S., Comparing Laser Desorption Ionization and Atmospheric Pressure Photoionization Coupled to Fourier Transform Ion Cyclotron Resonance Mass Spectrometry To Characterize Shale Oils at the Molecular Level. *Energy & Fuels* **2013,** *27* (4), 1830-1837.
215. Cho, Y.; Witt, M.; Kim, Y. H.; Kim, S., Characterization of Crude Oils at the Molecular Level by Use of Laser Desorption Ionization Fourier-Transform Ion Cyclotron Resonance Mass Spectrometry. *Anal. Chem.* **2012,** *84* (20), 8587-8594.
216. Rogel, E.; Witt, M.; Moir, M. E., Effects of Aging on Asphaltene Deposit Composition Using Ultrahigh-Resolution Magnetic Resonance Mass Spectrometry. *Energy & Fuels* **2019,** *33* (10), 9596-9603.
217. Chacón-Patiño, M. L.; Blanco-Tirado, C.; Orrego-Ruiz, J. A.; Gómez-Escudero, A.; Combariza, M. Y., High Resolution Mass Spectrometric View of Asphaltene–SiO2 Interactions. *Energy & Fuels* **2015,** *29* (3), 1323-1331.
218. May, J. C.; Morris, C. B.; McLean, J. A., Ion Mobility Collision Cross Section Compendium. *Anal. Chem.* **2017,** *89* (2), 1032-1044.
219. Lapthorn, C.; Pullen, F.; Chowdhry, B. Z., Ion mobility spectrometry-mass spectrometry (IMS-MS) of small molecules: Separating and assigning structures to ions. *Mass Spectrom. Rev.* **2013,** *32* (1), 43-71.
220. Wu, Q.; Wang, J.-Y.; Han, D.-Q.; Yao, Z.-P., Recent advances in differentiation of isomers by ion mobility mass spectrometry. *TrAC, Trends Anal. Chem.* **2020,** *124*, 115801.
221. Xie, C.; Wu, Q.; Zhang, S.; Wang, C.; Gao, W.; Yu, J.; Tang, K., Improving glycan isomeric separation via metal ion incorporation for drift tube ion mobility-mass spectrometry. *Talanta* **2020,** *211*, 120719.
222. Adams, K. J.; Ramirez, C. E.; Smith, N. F.; Muñoz-Muñoz, A. C.; Andrade, L.; Fernandez-Lima, F., Analysis of isomeric opioids in urine using LC-TIMS-TOF MS. *Talanta* **2018,** *183*, 177-183.
223. Gabelica, V.; Shvartsburg, A. A.; Afonso, C.; Barran, P.; Benesch, J. L. P.; Bleiholder, C.; Bowers, M. T.; Bilbao, A.; Bush, M. F.; Campbell, J. L.; Campuzano, I. D. G.; Causon, T.; Clowers, B. H.; Creaser, C. S.; De Pauw, E.; Far, J.; Fernandez-Lima, F.; Fjeldsted, J. C.; Giles, K.; Groessl, M.; Hogan Jr, C. J.; Hann, S.; Kim, H. I.; Kurulugama, R. T.; May, J. C.; McLean, J. A.; Pagel, K.; Richardson, K.; Ridgeway, M. E.; Rosu, F.; Sobott, F.; Thalassinos, K.; Valentine, S. J.; Wyttenbach, T., Recommendations for reporting ion mobility Mass Spectrometry measurements. *Mass Spectrom. Rev.* **2019,** *38* (3), 291-320.
224. Kanu, A. B.; Dwivedi, P.; Tam, M.; Matz, L.; Hill, H. H., Jr., Ion mobility-mass spectrometry. *J. Mass Spectrom.* **2008,** *43* (1), 1-22.
225. Benigni, P.; Bravo, C.; Quirke, J. M. E.; DeBord, J. D.; Mebel, A. M.; Fernandez-Lima, F., Analysis of Geologically Relevant Metal Porphyrins Using Trapped Ion Mobility Spectrometry–Mass Spectrometry and Theoretical Calculations. *Energy & Fuels* **2016,** *30* (12), 10341-10347.
226. Benigni, P.; Sandoval, K.; Thompson, C. J.; Ridgeway, M. E.; Park, M. A.; Gardinali, P.; Fernandez-Lima, F., Analysis of Photoirradiated Water Accommodated Fractions of Crude Oils Using Tandem TIMS and FT-ICR MS. *Environmental Science & Technology* **2017,** *51* (11), 5978-5988.
227. Farenc, M.; Corilo, Y. E.; Lalli, P. M.; Riches, E.; Rodgers, R. P.; Afonso, C.; Giusti, P., Comparison of Atmospheric Pressure Ionization for the Analysis of Heavy Petroleum Fractions with Ion Mobility-Mass Spectrometry. *Energy & Fuels* **2016,** *30* (11), 8896-8903.
228. Lalli, P. M.; Corilo, Y. E.; Rowland, S. M.; Marshall, A. G.; Rodgers, R. P., Isomeric Separation and Structural Characterization of Acids in Petroleum by Ion Mobility Mass Spectrometry. *Energy & Fuels* **2015,** *29* (6), 3626-3633.
229. Lalli, P. M.; Jarvis, J. M.; Marshall, A. G.; Rodgers, R. P., Functional Isomers in Petroleum Emulsion Interfacial Material Revealed by Ion Mobility Mass Spectrometry and Collision-Induced Dissociation. *Energy & Fuels* **2017,** *31* (1), 311-318.
230. Maleki, H.; Ghassabi Kondalaji, S.; Khakinejad, M.; Valentine, S. J., Structural Assignments of Sulfur-Containing Compounds in Crude Oil Using Ion Mobility Spectrometry-Mass Spectrometry. *Energy & Fuels* **2016,** *30* (11), 9150-9161.
231. Yassine, M. M.; Dabek-Zlotorzynska, E., Investigation of isomeric structures in a commercial mixture of naphthenic acids using ultrahigh pressure liquid chromatography coupled to hybrid traveling wave ion mobility-time of flight mass spectrometry. *Journal of Chromatography A* **2018,** *1572*, 90-99.

232. Lanucara, F.; Holman, S. W.; Gray, C. J.; Eyers, C. E., The power of ion mobility-mass spectrometry for structural characterization and the study of conformational dynamics. *Nature Chemistry* **2014,** *6* (4), 281-294.
233. Hernandez, D. R.; DeBord, J. D.; Ridgeway, M. E.; Kaplan, D. A.; Park, M. A.; Fernandez-Lima, F., Ion dynamics in a trapped ion mobility spectrometer. *Analyst* **2014,** *139* (8), 1913-1921.
234. Ridgeway, M. E.; Lubeck, M.; Jordens, J.; Mann, M.; Park, M. A., Trapped ion mobility spectrometry: A short review. *Int. J. Mass spectrom.* **2018,** *425*, 22-35.
235. Boyd, P. D. W.; Smith, T. D.; Price, J. H.; Pilbrow, J. R., Electron Spin Resonance Study of Metal Ion Separations in Dimeric Copper (II) and Vanadyl Porphyrins. *The Journal of Chemical Physics* **1972,** *56* (3), 1253-1263.
236. Lemberg, R.; Legge, J., Hematin compounds and bile pigments. **1949**.
237. Brown, S. B.; Shillcock, M.; Jones, P., Equilibrium and kinetic studies of the aggregation of porphyrins in aqueous solution. *Biochem. J* **1976,** *153*, 279-285.
238. Pasternack, R. F.; Francesconi, L.; Raff, D.; Spiro, E., Aggregation of nickel (II), copper (II), and zinc (II) derivatives of water-soluble porphyrins. *Inorg. Chem.* **1973,** *12* (11), 2606-2611.
239. Zhao, X.; Xu, C.; Shi, Q., Porphyrins in Heavy Petroleums: A Review. In *Structure and Modeling of Complex Petroleum Mixtures*, Springer: 2015; pp 39-70.
240. Santos Silva, H.; Alfarra, A.; Vallverdu, G.; Bégué, D.; Bouyssiere, B.; Baraille, I., Impact of H-Bonds and Porphyrins on Asphaltene Aggregation As Revealed by Molecular Dynamics Simulations. *Energy & Fuels* **2018,** *32* (11), 11153-11164.
241. Garcia-Montoto, V.; Verdier, S.; Maroun, Z.; Egeberg, R.; Tiedje, J. L.; Sandersen, S.; Zeuthen, P.; Bouyssiere, B., Understanding the removal of V, Ni and S in crude oil atmospheric residue hydrodemetallization and hydrodesulfurization. *Fuel Process. Technol.* **2020,** *201*, 106341.
242. Acevedo, N.; Moulian, R.; Chacón-Patiño, M. L.; Mejia, A.; Radji, S.; Daridon, J.-L.; Barrère-Mangote, C.; Giusti, P.; Rodgers, R. P.; Piscitelli, V.; Castillo, J.; Carrier, H.; Bouyssiere, B., Understanding Asphaltene Fraction Behavior through Combined Quartz Crystal Resonator Sensor, FT-ICR MS, GPC ICP HR-MS, and AFM Characterization. Part I: Extrography Fractionations. *Energy & Fuels* **2020,** *34* (11), 13903-13915.
243. Putman, J. C.; Gutiérrez Sama, S.; Barrère-Mangote, C.; Rodgers, R. P.; Lobinski, R.; Marshall, A. G.; Bouyssière, B.; Giusti, P., Analysis of Petroleum Products by Gel Permeation Chromatography Coupled Online with Inductively Coupled Plasma Mass Spectrometry and Offline with Fourier Transform Ion Cyclotron Resonance Mass Spectrometry. *Energy & Fuels* **2018,** *32* (12), 12198-12204.
244. Moulian, R.; Zheng, F.; Salvato Vallverdu, G.; Barrere-Mangote, C.; Shi, Q.; Giusti, P.; Bouyssiere, B., Understanding the Vanadium–Asphaltene Nanoaggregate Link with Silver Triflate Complexation and GPC ICP-MS Analysis. *Energy & Fuels* **2020**.

ECOLE DOCTORALE :
Sciences Exactes et leurs Applications

LABORATOIRE :
UMR 5254 IPREM, Université de Pau et des Pays de l'Adour
China University of Petroleum-Beijing

Fang ZHENG
zhengfangg@hotmail.com